# Biopsy-Implantable Chemical Sensor

by

Christophoros C. Vassiliou

S.B. Electrical Science and Engineering, MIT, 2004
M.Eng. Electrical Engineering and Computer Science, MIT, 2006

Submitted to the
Department of Electrical Engineering and Computer Science
in partial fulfillment of the requirements for the degree of

Doctor of Philosophy

at the

MASSACHUSETTS INSTITUTE OF TECHNOLOGY

September 2013





Author .....
Department of Electrical Engineering and Computer Science
August 30, 2013

Certified by .....
Michael J. Cima
David H. Koch Professor of Engineering
Thesis Supervisor

Accepted by .....
Leslie A. Kolodziejski
Chair of the Committee on Graduate Students

# Biopsy-Implantable Chemical Sensor

by

Christophoros C. Vassiliou

Submitted to the
Department of Electrical Engineering and Computer Science
on August 30, 2013, in partial fulfillment of the
requirements for the degree of
Doctor of Philosophy

## Abstract

There is a dire need for tools that can rapidly detect cancer treatment efficacy. A cancer patient must endure the side effects of chemotherapy and radiotherapy. It will be weeks before a change in the size of the tumor can be observed and the oncologist has the information necessary to determine whether treatment is working. Valuable time is lost searching for the right treatment and the right dose.

This thesis presents a sensor that can be implanted inside the body during a biopsy procedure and wirelessly report on the tissue environment. The sensor has direct access and can track metabolic markers, such as pH and oxygen, which have been shown to predict outcome, dose, and response to cancer treatment. These markers cannot be measured anywhere else except directly inside the tissue, and this sensor provides that access. The probe allows for repeat, non-invasive measurement of the same location after the initial biopsy.

The sensor consists of a small nuclear magnetic resonance (NMR) probe that has a cavity filled with a contrast agent sensitive to the chemical of interest. An NMR relaxation measurement of the contrast agent reveals the chemical concentration. Wireless NMR measurements are performed with the aid of a reader probe that resides outside of the body. The reader generates the excitation pulses and receives the NMR signal. The sensor and reader have a mutual inductance that enables the wireless measurement. The resonant coupling allows wireless NMR measurements with enhanced signal-to-noise ratio. The field inside the sensor is amplified compared to the surrounding tissue. The amplification localizes the measurement to the sensor

and eliminates any signal from the surrounding tissue. The coupled reader-sensor performs standard NMR relaxation measurements. A method is presented to produce the sensors in large numbers, and the sensors are tested in vivo.

The probe is designed to be implanted during a routine procedure and would be no more invasive than existing clinical practice. The measurements can track tumor progression and guide therapy before any physical changes can be observed, and the patient can receive the right treatment as soon as possible.

Thesis Supervisor: Michael J. Cima
Title: David H. Koch Professor of Engineering

# Acknowledgments

I am truly grateful to my advisor, Professor Michael Cima. I joined his lab as an undergraduate and have had the opportunity to work on a number of projects. The breadth of research topics in his lab and the number of departments that have been represented in the lab are a testament to his boundless energy and fearless approach to science and engineering. He has taught me to ask the right questions and inspired me to tackle seemingly insurmountable problems, seeking solutions that draw from diverse fields. I look forward to our future collaborations.

I am thankful for Professor Sangeeta Bhatia and Professor Elfar Adalsteinsson for their service on my thesis committee. I am grateful for their advice regarding my personal and career development, and I am certain that those lessons will continue to benefit me for many years to come.

I have benefited from the guidance and mentorship of Professor Isaac Chuang, who has offered many helpful suggestions and recommendations throughout my graduate career. I am grateful to the Course VI Graduate Office and to Janet Fischer, in particular, for her patience.

Funding for this research was provided by the National Cancer Institute, the National Science Foundation, and the United States Air Force.

I have had the good fortune of being in a lab with a group of amazing individuals whose greatest strength is their willingness and ability to work together. The lab members have been a second family to me and I truly enjoyed the time I've spent in the lab. I would like to thank my Grace Kim and Karen Daniel, with whom I started the sensors project; they gently introduced me to the world of biomedical research.

Many thanks to the other members of the project: Yibo Ling, Vincent Liu, and Syed Imaad. I will always remember our many hours in the lab, our trips to Billerica and Burlington, and our conversations about nothing in between scans in the imaging suite. I am indebted to you for your contributions to the project, and I could not have asked for a better group of people to work with. I look forward to seeing how the project evolves with the newest member Gregory Ekchian. I was fortunate to have had the opportunity to work with an amazing undergraduate researcher, Melanie Adams. Special thanks to Byron Masi with whom I shared countless hours in the machine shop. Many, many thanks to you all for your camaraderie and friendship: Hong Linh, Heejin, Yoda, Dan, Alex, Noel, Maple, Qunya, Jen, Urvashi, Kevin, Jay, Jack, Negar, Joan, Matt, Laura, Núria, Katerina, and Lina. Thanks to Milton for assistance with the machining. I am truly thankful for all the hard work that Barbara Layne and Lenny Rigione put in to keep the lab running and us out of trouble.

I enjoyed working with our collaborators through the CCNE project, and especially Keith Brown, Dave Issadore, and Professor Westervelt at Harvard University.

Thank you also to Elizabeth, Rachel, and Greg for helpful comments and suggestions that improved this manuscript.

I have benefited greatly from the amazing staff and resources at the Koch Institute, and I am especially thankful for the help of Scott Malstrom and Milton Cornwall-Bradley. I would also like to thank Alex Fiorentino for the many outreach opportunities.

MIT has been my academic home since my undergraduate years, and I have benefited immensely from all that MIT has to offer. The MIT Libraries have been of immense help to my study and research. Big thanks to Mark Belanger and Tony Caloggero

at the Edgerton Student Shop. And many thanks to the members of DCM for their assistance and training. Thank you to my many MIT friends but especially Krish, Robin, Laura, Daanish, and Ted.

I am truly thankful for my Mom and Dad, Hariclea and Christakis, who encouraged my early interest in science and engineering and whose sacrifices ensured that my siblings and I received the best possible education. Thank you to my in-laws, Judy and Paul, for their support and assistance throughout and especially for their help with errands during crunch time.

Finally, I would like to express my sincere gratitude to my wife and best friend, Elizabeth. Her enthusiasm, wit, and humor have seen me through my graduate degree. She is my champion and cheerleader, and I am a better person because of her. This is as much her achievement as it is my own.

*I dedicate this thesis*
*in memory of our beloved children,*
*Angeliki and Panagiotis,*
*Twinnie, and Baby Boy.*

# Contents

**1 The clinical need** **27**

1.1 Sensors inside the body . . . . . 27

1.2 Cancer . . . . . 30

1.2.1 Treatment . . . . . 30

1.2.2 New drug approvals . . . . . 32

1.2.3 The tumor microenvironment . . . . . 33

1.3 Thesis overview . . . . . 34

**2 Background** **37**

2.1 Nuclear Magnetic Resonance . . . . . 38

2.1.1 Signal strength . . . . . 38

2.1.2 Relaxation . . . . . 41

2.1.3 Hardware . . . . . 45

2.2 Resonant Circuits . . . . . 46

2.3 Mutual Induction . . . . . 54

**3 Wireless NMR** **59**

3.1 Magnetic field amplification . . . . . 59

3.2 Circuit model . . . . . 62

3.2.1 Transmit mode . . . . . 64

3.2.2 Receive mode . . . . . 68

3.3 Design considerations . . . . . 73

3.3.1 Sensor length . . . . . 73

3.3.2 Wire diameter . . . . . 74

3.3.3 Sensor diameter . . . . . 75

3.3.4 Reader coil diameter . . . . . 79

3.3.5 Number of turns on the reader coil . . . . . 79

3.3.6 Noise and EMI . . . . . 83

3.3.7 Reader coil length . . . . . 84

3.3.8 Tissue conductivity . . . . . 84

3.4 Practical considerations . . . . . 86

3.4.1 Tuning frequency . . . . . 89

3.4.2 Misalignment . . . . . 90

3.4.3 Remote measurement . . . . . 93

3.5 Sensor fabrication . . . . . 95
3.5.1 Machining the plastic body . . . . . 98
3.5.2 Winding the coil . . . . . 101
3.5.3 Tuning the resonant circuit . . . . . 101
3.5.4 Potting in epoxy . . . . . 102
3.5.5 Filling with the assay material . . . . . 104
3.6 Reader fabrication . . . . . 104
3.7 Testing the complete system . . . . . 105
3.8 Conclusion . . . . . 107

**4 Oxygen sensing** **111**

4.1 Oxygen and cancer therapy . . . . . 112
4.2 Oxygen as a contrast agent . . . . . 113
4.3 Oxygen sensitivity . . . . . 116
4.4 Oxygen sensitivity experiments . . . . . 118
4.5 Tissue oxygen measurements . . . . . 118
4.5.1 Inspired oxygen . . . . . 121
4.5.2 Restriction of circulation . . . . . 121
4.6 Prospects . . . . . 123

**5 pH sensing** **127**

5.1 Electrochemical pH sensors . . . . . 128

5.2 HEMA-BIS gels for pH measurements . . . . . 129

5.3 Temperature dependence . . . . . 132

5.4 Pilot study . . . . . 136

5.5 Detecting chemotherapeutic efficacy . . . . . 138

5.6 Conclusion and future work . . . . . 142

**6 Detecting protein biomarkers** **145**

6.1 Cardiac biomarkers . . . . . 147

6.1.1 Exposure . . . . . 148

6.1.2 Mouse myocardial infarction model . . . . . 148

6.1.3 Future cardiac sensor applications . . . . . 152

6.2 Nanoparticle aggregation . . . . . 154

6.3 Prospects . . . . . 164

**7 Conclusion** **165**

**A Least-squares echo estimation** **173**

A.1 Theory . . . . . 174

A.2 Experiment . . . . . 176

**B Numerical computation of mutual inductance** 185

**Bibliography** 189

THIS PAGE INTENTIONALLY LEFT BLANK

# List of Figures

1-1 Biopsy implantable NMR sensor . . . . . 35

2-1 Transverse relaxation is measured using the CPMG pulse sequence. A 90° pulse rotates the magnetization into the $x - y$ plane. A train of refocusing pulses compensates for field inhomogeneities and the signal appears as brief "echoes". The envelope of the echo amplitudes (dashed) decays with a time constant, $T_2$. . . . . 43

2-2 Saturation Recovery measures the longitudinal, or spin-lattice relaxation. A burst of pulses with decreasing intervals completely saturate the magnetization such that the net is zero. The system is allowed to recover for a time *tau* during which the $z$-directed magnetization approaches the equilibrium magnetization, $M_0$. The relaxation is interrupted with a spin-echo sequence to generate an echo with $M(\tau) = M_0(1 - e^{-\tau/T_1})$. The relaxation time, $T_1$, is measured by repeating the sequence for different recovery times. . . . . 44

2-3 Plate format NMR (left) combines a commercially-available single-sided NMR probe with a 3-axis robot. The NMR MOUSE measures a thin slice above the surface thanks to its unconventional magnet arrangement shown on the right. . . . . 47

2-4 An RLC circuit models the capacitor-inductor circuit with the resistor representing the losses in the inductor. At very low frequency the resistance is R, while at high frequency the capacitor shorts out the current source. . . . . 48

2-5 Response of the RLC circuit to a current input . . . . . 49

2-6 Frequency response of an RLC circuit . . . . . 51

2-7 Two dimensional simulation of magnetic field in cylindrical coordinates $\hat{y} - \hat{r}$. A 20 turn coil is modeled with 1 A current flow. The field lines show the direction of $\vec{B}$, and the color represents the magnitude of the $\hat{y}$ directed field. . . . . 52

2-8 Two dimensional cross section of current distribution. The images are cylindrically symmetric about the left side of the page. The coil has a larger resistance at high frequency because the current flows mostly on the inner surface of the coil. . . . . 53

2-9 Mutual inductance represented in a circuit diagram. . . . . 54

2-10 The field generated by a changing current in one coil induces a voltage, $v_2(t) = -M\frac{di_1}{dt}$, in a nearby coil. . . . . 56

3-1 A large field amplification occurs if a coil is excited on resonance. . . 62

3-2 The field generated inside the sensor is greatly enhanced when the sensor is excited at the resonance frequency by a current flowing in the reader coil. . . . . 63

3-3 Transmit path showing a $50\,\Omega$ voltage source connected to the reader probe. The resistors model losses in the coils. . . . . 65

3-4 Block diagram of the coupled probes. Solution of the feedback loop gives the current in the sensor coil. . . . . 65

3-5 Simplified transmit path with the admittance $Y_{CP}$ representing the couple reader-sensor. A single-coil NMR probe has $Y_{CP} = (R + j\omega L)^{-1}$. 67

3-6 Simulation of the field inside the sensor coil as a function of distance from the reader coil. A tuned reader coil increases the field inside the sensor coil more than 20 fold. . . . . 69

3-7 Signal reception path. The NMR signal appears as a voltage across the sensor coil. Resistive losses in the coils are modeled as noise sources. 70

3-8 A tuned reader coil ensures enhanced reception of the NMR signal. . 72

3-9 Field map of sensor coil showing high degree of uniformity in the sample chamber. The contour lines represent $M_{xy}/M_0$, the projection onto the transverse plane following a 90° pulse calibrated to the center of the chamber. . . . . 74

3-10 The signal-to-noise ratio as the wire diameter is increased. The smallest possible wire diameter will maximize the signal-to-noise by increasing the sample volume. The coil length is fixed and the wire is wound as compactly as possible; many more turns of the finer wire are needed to fill the length. . . . . 76

3-11 Photograph of sensors with smaller diameter coil and chamber to investigate the practical lower limit on sensor size. . . . . 77

3-12 Signal strength versus sensor diameter normalized to the 2.2 mm sensor on the single-sided magnet. The largest sensor for a given application gives the strongest signal. . . . . 77

3-13 Simulated signal-to-noise ratio versus sensor diameter. Increasing the sensor volume increases the signal-to-noise ratio, but the gains are modest as the sensor becomes very large. . . . . 78

3-14 The received signal amplitude decreases as the number of turns on the reader coil is increased. . . . . 80

3-15 Thermal noise at the receiver due to losses in the reader and sensor coils. The thermal noise from the reader coil dominates the sensor coil noise when the reader coil has fewer than six turns. If thermal noise is the only noise source then the reader coil should be designed so that the sensor noise is dominant. . . . . 81

3-16 Considering only the thermal noise, the signal-to-noise ratio increases with the number of turns on the reader coil. . . . . 82

3-17 Mutual inductance between a two-turn reader coil and a sensor coil versus position. The diagram is rotationally symmetric about the $\hat{x}$ direction. The thick line represents the volume over which $M$ changes less than 1% from the origin. . . . . 85

3-18 Mutual inductance contour map when the two turns of the reader coil are separated by one radius. The 1% region is significantly expanded compared to Figure 3-17. . . . . 85

3-19 The field strength inside the sensor is virtually unchanged over the range of conductivity expected inside the body. The increased resistance of the reader coil captures the loss in the conductive medium. . 87

3-20 Plot of sensor field versus the conductivity of the surrounding medium. Higher frequency operation is generally preferred except in very high conductivity media. . . . . 88

3-21 Plot of signal-to-noise ratio as a function of mismatch between the sensor resonant frequency and the Larmor frequency. Maximum SNR is achieved on resonance, but slight deviations in the sensor's resonant frequency do not matter. . . . . 89

3-22 The reader coil can be tuned to a lower frequency without the sensor to maximize the signal-to-noise ratio when the sensor is inserted. The SNR is equivalent to tuning at the resonant frequency with the sensor inside. This method provides a way to tune when the precise location of the sensor is unknown. . . . . 91

3-23 Measured echo amplitude versus the angle between the reader and sensor axes. The signal is relatively insensitive to angular deviations less than 20° and is detectable even with deviations as large as 60°. . 92

3-24 Field strength inside the sensor at a distance from the reader coil mimics the human system configuration. A larger radius coil improves the sensitivity at larger distances. There is an optimum coil radius for each measurement depth. . . . . 94

3-25 Photograph of an implantable sensor . . . . . 95

3-26 Core biopsy needle. A trocar facilitates insertion into the body. The cannula provides a channel through which the biopsy needle can obtain multiple tissue samples. . . . . 96

3-27 Sensor implantation following a mock biopsy procedure on a gelatin phantom. . . . . 97

3-28 Subcutaneous implantation needle. . . . . 98

3-29 Key components of implantable sensor . . . . . 99

3-30 Machining the sensor body and cavity. The cavity is drilled (1-2) and the coil support bobbin are milled using carbide end mills (3). The lower portion will house the capacitor and is cut to the final sensor diameter (4). . . . . 100

3-31 Machining the capacitor pocket. The stock is rotated 90°, and a pocket is cut for the tuning capacitor (5-6). Wire through-holes are drilled (7) before the completed body is parted from the stock (8). . . . . 100

3-32 Photograph of a completed NMR probe. A sensor is made by filling the chamber with the appropriate chemically sensitive contrast agent. 103

3-33 Complete measurement apparatus for preclinical testing. . . . . 106

3-34 Verifying the measurement of an echo and scaling with pulse amplitude. The maximum echo amplitude represents the 90° condition. . . 107

3-35 Transverse relaxation measurement acquired with an implanted sensor. 108

4-1 The oxygen sensor response (top) to changing oxygen fraction in a balance of nitrogen (bottom). Each condition was maintained for 30 min. A saturation pulse sequence with 600 ms recovery time yields a very fast $T_1$-weighted intensity measurement for monitoring dynamics. 119

4-2 Calibration curve of $T_1$ weighted intensity versus oxygen fraction in nitrogen. The error bars are smaller than the marker size. . . . . 120

4-3 Boxplot of $T_1$ measured by a sensor implanted in a rat calf muscle. The inspired gas was changed from oxygen to air, and an increase in $T_1$ followed. A second transition back to oxygen did not show a corresponding difference. A longer time might be needed for the recovery. . . . . 122

4-4 $T_1$ measured in a calf muscle under free and constricted circulation. A significant increase in relaxation time is observed after applying light pressure to the thigh. . . . . 124

5-1 Measurements of $T_2$ versus pH of a saline solution using HEMA-BIS gel inside a sensor. A peristaltic pump maintained a constant flow of saline from a temperature controlled bath over the device. A pH probe in the bath monitored both temperature and pH. . . . . 131

5-2 $T_2$ versus pH calibration curve. . . . . 133

5-3 Histogram of pH measurement error establishing a limit of detection better than 0.1 pH units. . . . . 134

5-4 The measured $T_2$ decreases with temperature. The expected temperature deviation in vivo is very narrow compared to the studied range, but the calibration curve must be performed at body temperature. . . 135

5-5 Relaxation time measurement for sensors implanted inside, near, and contralaterally to the tumor. The sensors on the tumor side measured a shorter $T_2$, consistent with a lower tissue pH. . . . . 137

5-6 Measured relaxation times for sensors implanted in mouse tumors. Those animal receiving treatment (doxorubicin) are shown as solid red lines, and the control group that received saline injections are shown in dashed black lines. Each line represents a different animal. No discernible pattern emerges between the two groups suggesting that this dose had no effect on the tumor pH. . . . . 140

5-7 Measured relaxation times for implanted sensors that received no treatment. The mean $T_2$ (thick red) decreases over the four days of implantation consistent with a net trend towards more acidic conditions in the tumors. . . . . 141

5-8 Histologic section of an untreated tumor (H&E stain). Significant regions of necrotic tissue are mostly stained pink. Healthy melanoma cells have purple-stained nuclei. The brown spots are melanin, characteristic of melanoma. . . . . 142

5-9 H&E stained sections of treated and untreated tumors. Substantial regions of necrotic tissue (pink with no purple stained nuclei) are apparent in both sections. . . . . 143

6-1 Prototype device used to test protein detection. Sensitive nanoparticles are encapsulated in a plastic body using a semipermeable membrane that keeps the nanoparticles in but allows the target to pass. . . . . 146

6-2 Antibody based sensors measure exposure, defined as the time integral of concentration. Transient events can be detected because exposure remains high even after the concentration has subsided. . . . . 149

6-3 Measured $T_2$ versus time. Sensors exposed to steady concentrations of myoglobin respond at different rates but saturate to the same value. Adapted from Ling, Pong, Vassiliou et al. [89]. . . . . 150

6-4 Measured $T_2$ versus myoglobin exposure. The measurements from Figure 6-3 all lie along a characteristic $T_2$ vs exposure curve. Transient profiles (markers) simulate one-off events and also lie along the curve. Adapted from Ling, Pong, Vassiliou et al. [89]. . . . . 151

6-5 Sensors implanted in a myocardial infarction (MI) model. MRI measurements of the sensor (a) show one possible use. Sham and control experiments show that the sensors indeed detect the MI (b). The measured $T_2$ increase with the amount of damaged tissue (c-e) as would be expected from Figure 6-4. Reproduced from Ling, Pong, Vassiliou et al. [89]. . . . . 153

6-6 Scanning electron micrograph of 1 µm beads. . . . . 155

6-7 A tube containing particles suspended in molten agarose is inserted into a weak magnetic field. The particles begin to form chains. A water-cooled jacket gels the agar solution after a predetermined time, and the particle formation is captured. . . . . 156

6-8 Bright field transmission micrograph of 1 µm beads suspended in agar. The chains were created by magnetizing the sample using an electromagnet ($B$=4 mT). . . . . 156

6-9 The average chain length determined by optical imaging shows a power-law increase with time inside the 4 mT magnetic field. . . . . 157

6-10 The tube is rotated along an axis perpendicular to instrument field, $B_0$, with $\theta_c$ being the angle between particle chains and $B_0$. . . . . 158

6-11 Relaxation time measurements as a function of angle between the magnetized direction, $\hat{B}_c$ and the measurement field direction, $\hat{B}_0$. . . 159

6-12 Measured relaxation time as a function of magnetization time shows a power law increase of $T_2$ with time. . . . . 160

6-13 The difference between high and low $T_2$ values as the sample is rotated relative to the magnetic field also increases as a function of magnetization time and chain length. . . . . 161

6-14 Isosurfaces of field perturbations caused by a three-particle chain at different angles to the field. The top and bottom surfaces (red) bound the 1% positive field deviation, and the center, torroidal surface (blue) bounds the negative 1% field deviation. The shape and volume of the 1% boundaries change with angle and are responsible for the angular dependence of $T_2$. . . . . 162

6-15 The volume of solution for which the field is perturbed at least 1% is shown versus chain angle and normalized to the particle volume. The three-particle chains show a gentler field gradient consistent with an increasing $T_2$. Rotating the chain 90° increases the field gradient, and a shorter $T_2$ is expected. . . . . 163

7-1 Concept implantable sensor for simultaneous pH and oxygen measurements. . . . . 170

A-1 Typical signal acquired from one echo. The echo envelope is formed by summing multiple echoes at the start of a multi-echo sequence. . 177

A-2 The signal-to-noise ratio of the least squares estimate increases as more data is acquired. Increasing the integration time eventually adds noise but no data and leads to a reduction in SNR. . . . . 179

A-3 Echo envelopes as detected with a different receiver angle. The dotted lines represent the peak of the real and imaginary phases. . . . . 180

A-4 Plot of the maximum achievable signal-to-noise ratio versus the receiver phase angle. The integral method requires phase alignment, but the least squares method gives an optimal SNR regardless of phase angle. . . . . 181

A-5 The echo envelope changes over the first few echoes. . . . . 182

A-6 Normalized signal amplitude for echoes 5 to 100. The echo shape is constant within the noise of any one measurement. . . . . 183

# List of Tables

2.1 Simulation parameters and outputs for a 20-turn coil. . . . . 54

4.1 Siloxane molecule physical parameters and interaction with oxygen. The values are used in Equation (4.2) to estimate $T_1$. . . . . 115

4.2 Measured and predicted values of $T_1$ for siloxanes in air. The sensitivity is ultimately determined by the very high inherent $T_1$ values of the material. . . . . 115

5.1 Acquisition parameters for measuring the transverse relaxation time, $T_2$. . . . . 136

THIS PAGE INTENTIONALLY LEFT BLANK

# Chapter 1

# The clinical need

Sensors implanted inside the body offer the medical practitioner a unique vantage point. They provide direct access to the physical and chemical environment of the tissue that blood tests and imaging do not offer. Needle probes provide similar access but are too invasive for routine and repeat use. This thesis presents a sensor designed to be implanted during a biopsy procedure and to wirelessly report on its surroundings. The sensor performs repeat virtual biopsies on the same site using contrast agents developed for magnetic resonance imaging (MRI) to measure proteins, oxygen, and pH. This sensor is demonstrated primarily as a tool for monitoring cancer but also finds applications in heart disease and traumatic injury.

## 1.1 Sensors inside the body

A sensor converts a physical or chemical property into information. Sensors that reside inside the body must provide medically useful information not available through

other means, in a timely manner, and with minimal patient discomfort. These constitute the sensor engineer's guiding principles. The usefulness of a sensor is measured by how its availability changes clinical practice. Before building a sensor the engineer should ask, "Will clinicians do anything differently based on this sensor's readings?" This question is best answered in conversation with a practicing clinician.

The discussion with the clinician is also critical to determine where the sensor will reside and how it will be deployed. All existing procedures in the standard of care offer avenues for deploying a sensor. The chosen avenue will also constrain the device's design. If key-hole surgery is performed with laparoscopic tools then the device must be designed to fit through those tools. Designing for existing procedures makes the deployment method obvious to a doctor or surgeon; it fits in neatly with their current practice. The existing procedures also offer a method of payment since reimbursement codes are already in the system. Avoiding additional procedures reduces the risk to the patient and the overall cost of care.

How fast the sensor must measure depends on the application. An implantable defibrillator must continuously monitor heart activity by taking measurements many times per second. It does this to take necessary corrective action when abnormal cardiac rhythms are detected. The information must be acted on immediately and while the patient may be incapacitated. The direct monitoring enables the life-saving instrument[1]. A sensor that tries to detect whether cancer therapy is working only needs to measure once a day or less. Measuring every second will not add any information, since no changes occur on that time-scale. The decision on how often to sample influences how the device is powered and, consequently, how big the device must be made. The defibrillator requires a large battery; whereas, the cancer sensor presented here is powered wirelessly when the measurement is needed. It can be

made smaller than commercially available medical batteries[2].

The PillCam is a small battery operated camera that exemplifies the importance of patient comfort. It is swallowed and travels along the 9 m tortuous path of the digestive system taking photographs along the way[3, 4]. It transmits the images to a belt worn by the patient. The doctor receives a complete view of the GI tract within one or two days. The imaging is done at home and avoids having to schedule an endoscopy or colonoscopy. It has farther reach than either of those procedures and is incomparably more comfortable. It is no surprise that it is finding uses for diagnosing many types of gastrointestinal conditions.

There has been no discussion of science or engineering so far, because the most important decision is what a sensor or device should do to provide the most benefit to the patient. The technology is secondary; even the most technologically advanced sensor is useless if it provides no meaningful information or if it will never be used. The first decision is what the device should do, and then it is up to the engineer to choose the best tool for the job.

The sensor presented in this thesis is designed to monitor cancer directly from within a tumor. It measures clinically relevant markers that may indicate how the tumor is progressing and whether therapy is proving effective. It takes weeks of treatment for changes in the size of a tumor to manifest; changes in pH inside the tumor have been detected as early as one day after treatment. The sensor response time, measured in minutes and hours, is much faster than any anticipated change inside the tumor. Designed to be implanted during a biopsy procedure, the sensor fits nicely into clinical practice. It is no more invasive than the current standard of care, and the readout is completely non-invasive.

## 1.2 Cancer

Worldwide, 7.5 million people died from cancer in 2008. That year approximately 12.7 million people were diagnosed with cancer. Cancers of the lung, breast and colorectum made up one third of the total[5]. This year, in the United States alone, over 1.6 million people will be diagnosed with cancer[6]. It can be expected that the global diagnosis figure will rise dramatically as screening improves in developing nations and more cases are detected.

Fortunately the number of cancer survivors is also increasing. Patient education and better screening have lead to earlier detection and treatment[7]. There were over 13 million cancer survivors at the start of 2012; that number is expected to reach 19 million in the next decade[8]. Lesions are discovered through self-examination, routine screening, and imaging. A cancer diagnosis, however, is almost exclusively confirmed by a direct observation of the suspected tissue, that is, by biopsy[9]. A needle biopsy is an invasive medical procedure that removes a small tissue sample from inside the body. A pathologist microscopically examines the cells to look for cancerous cells. The findings also help identify the type of cancer, which will point to a particular course of therapy that is most likely to succeed. Treatment can involve radiotherapy, chemotherapy, and/or surgery.

### 1.2.1 Treatment

Cancer treatment is shockingly ineffective. The underlying complexity of the disease and the similarity between cancerous and normal cells make treatment challenging. A single genetic mutation kickstarts a cycle of abnormal cell growth. These cells

proliferate by evading the body's mechanisms for dealing with misbehaving cells. They co-opt blood vessels to provide perfusion necessary for growth and eventually escape from the tumor to invade the rest of the body[10, 11, 12]. The rapid rates of cell division and genetic mutation make treatment very hard, and resistance develops quickly even to treatments that were initially effective.

High rates of morbidity are associated with treating cancer. Many of the side effects are not from the disease but from the treatment. Patients undergoing chemotherapy or radiotherapy will likely experience fatigue, emotional distress, and severe pain[8]. Radiation therapy and surgery have fewer side effects because the treatment is localized, but tissue around the targeted area is still susceptible to damage.

Chemotherapy causes widespread damage to the body leaving no tissue unharmed; every system is adversely affected. The list of side effects mirrors the list of tissues and organs in the body. Chemotherapy reduces white blood counts, suppressing the immune system and increasing the risk of secondary infections. The drugs damage tissue throughout the digestive system, beginning in the mouth and gums, down the throat, and along the lining of the intestines. The compromised digestive system causes malnutrition and dehydration. Nausea and constipation are also common side effects that compound these problems. The brain, skin, lungs, hair follicles, and the peripheral nervous system are all adversely affected. Cardiotoxicity and decreased bone density are major concerns. Add extreme fatigue and sleep disruption to this, and it is not hard to see why over half of cancer patients experience severe emotional distress[8]. These adverse effects are accepted because chemotherapy does more damage to cancer cells than to healthy cells and because there are no other options.

Early diagnosis and treatment are critical to long term survival. The right drug and

dosage must be found early on to reduce the overall morbidity and prevent metastasis, which is responsible for 80 % of all cancer related deaths[10]. Many drugs are effective only for a small fraction of patients, and identifying the right drug for a patient is an entire area of research[9]. It may be weeks after the treatment starts before doctors can determine whether the drug is working or not. A sensor that directly monitors a tumor could quickly and definitively assess response thus saving critical time in the early stages of the disease.

### 1.2.2 New drug approvals

Recent drug approvals by the Food and Drug Administration (FDA) highlight the dire need for methods to determine whether a drug is working or not. Four recently approved drugs achieved less than 6 months increase in median survival with overall response rates well below 50% of the treated population. The drugs only modestly improve over previously approved drugs and some carry the potential for serious toxicity in the heart and liver. Detecting treatment efficacy is extremely important.

The human epidermal growth factor receptor 2 (HER2) is expressed in a third of breast cancer patients and is predictive of poor reponse to therapy[13]. However, the receptor can be targeted by antibodies and is the basis for several drugs. The response rate to trastuzumab is 30% among HER2 positive patients compared with just 9% across all patients. Added to chemotherapy it increased median survival from 20 to 25 months[10]. Among the 2013 drug approvals is ado-trastuzumab emtansine, which further extends the median survival to 31 months. The response rate is slightly higher than trastuzumab but still under 50%[14, 15, 16]. Clearly

there is an enormous benefit to identifying HER2 positive patients, but even among this preselected population more than half of the patients will not respond. While the newer drug may perform better across a patient population, there is no way of knowing whether an individual patient will respond or not.

Regorafenib is a new drug for treating metastatic colorectal cancer[17]. It was approved despite only increasing survival by 1.4 months with a response rate of 5%. The justification of approval in the summary review is telling, "While the absolute magnitude of the treatment effects on survival [...] are small, the ability of any single agent to demonstrate efficacy in this heavily pre-treated population represents clinical benefit" [18].

This particular drug has relatively mild side effects, but that is not always the case. Identifying the patients who are responding ensures that only those who are benefiting are subjected to the side effects. A sensor could identify the 60% of HER2 positive patients that aren't responding and reduce their risk of severe hepatic and cardiac toxicity. If efficacy is detected quickly, then the 9% of HER2 negative patients who might benefit from trastuzumab can be identified.

### 1.2.3 The tumor microenvironment

Cancer is more than just a collection of cells but behaves as an organ in which the surrounding environment is as important as the constituent cells[19]. The extracellular matrix, once thought to be a collection of cell-binding proteins, is increasingly being recognized as an important contributor to the tumor lifecycle[10, 20]. It is actively involved in cell proliferation, tumor growth, angiogenesis, and metastasis[21].

Even the physical arrangement of tumor cells is of critical importance; the future

growth pattern of a tumor depends on the three dimensional arrangement of its consituent cells[22]. A study on individual cells found that cells confined to a 20 µm diameter post were likely to die but cells given a 50 µm plot continued to grow[23]. This raises the possibility of new treatments that target the tumor microenvironment and not just the cells[24].

Cells removed from the body provide only part of the story. Cell morphology, gene mutations, and surface protein expression tell only half the story. One can envision that tumors will be characterized also by properties of tumor environment such as oxygen, pH, and vascularization. Studying the tumor environment should be as important as studying the response of cells in a culture dish. An oncologist with feedback from a sensor inside the tumor could quickly try multiple drugs, identify the one most likely to work, and start the patient on the right drug as soon as possible. The disease will be treated sooner, and the patient will be spared the side effects of ineffective treatment.

## 1.3 Thesis overview

This thesis presents an implantable NMR probe (figure 1-1) that can be implanted directly inside a tumor using a standard biopsy needle. A variety of NMR contrast agents are used to create sensors for oxygen, pH, and various proteins. The on-board circuit enhances the signal strength, allows wireless remote measurement, and eliminates any interfering signals from the surrounding tissue. The sensors exploit nuclear magnetic resonance (NMR) for measurement. Chapter 2 provides a brief introduction to NMR detection, resonant circuits, and mutual inductance. These three topics form the basis of a wireless NMR probe. Chapter 3 presents the theoret-

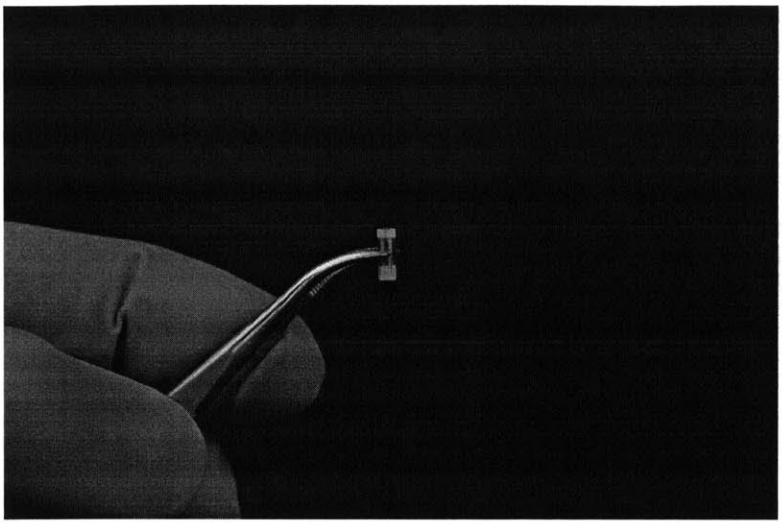

Figure 1-1: Biopsy implantable NMR sensor

ical framework and the design and construction of an implantable NMR probe. The sensors rely on contrast agents to convert a chemical concentration or dose into an NMR signal, and several examples are presented. Chapter 4 demonstrates on oxygen sensor and tests it in a rat model. These measurements can predict the efficacy of chemotherapy and radiotherapy. Chapter 5 presents a pH sensor for monitoring the acidic environment of a tumor tested in a melanoma model in mice. Decreasing pH following chemotherapy has been proposed as an indicator of treatment efficacy. Chapter 6 shows how protein biomarkers can be measured as sentinels for myocardial tissue damage caused by myocardial infarction or chemotherapy induced cardiotoxity. The prospects for human use are discussed in Chapter 7 along with additional work needed to bring this to fruition.

THIS PAGE INTENTIONALLY LEFT BLANK

# Chapter 2

# Background

The sensor is comprised of a wireless nuclear magnetic resonance (NMR) probe that contains a chemically sensitive contrast agent. NMR is not an obvious choice for a miniaturized sensor because the signal is extremely weak compared to other techniques. However, it offers an array of contrast mechanisms, and NMR can be performed on opaque media and through tissue. Optical sensors require clean, transparent samples. Optical detection through tissue is hindered by severe absorption and scattering. Ionizing radiation (X-ray) or radioactive sources (positron emission tomography) are unacceptable for repeat monitoring, while ultrasound lacks contrast and chemical sensitivity. Overall NMR is an excellent modality for sensors inside the body.

A wireless NMR probe is discussed in detail in Chapter 3. This chapter introduces three important concepts that the sensors rely on: nuclear magnetic resonance, resonant circuits, and mutual inductance.

## 2.1 Nuclear Magnetic Resonance

This thesis deals with a classical description of $^1$H NMR as introduced by Bloch[25]. This approach is acceptable because $^1$H is a spin-1/2 system, all samples are at high temperature (300 K), and each sample contains approximately $10^{20}$ spins. The net magnetization is not quantized, but rather a vector that can be manipulated with an alternating magnetic field. Almost every NMR book includes the classical description and derivation. A good overview is presented by Cowan[26]. Fukushima and Roeder give substantial practical advice on building NMR probes[27]. Slichter's text covers a graduate course on NMR[28], and the classic text by Abragam[29] is a complete treatise on all aspects of NMR theory. Important papers by Hoult and Richards present a clear method for determining the signal strength in an NMR experiment [30, 31] and a description of the NMR receiver[32]. The articles in the journal *Concepts in Magnetic Resonance*[33, 34] are written from a pedagogical perspective, covering all aspects of NMR. New research can be found in the *Journal of Magnetic Resonance*[35] and *Magnetic Resonance in Medicine*[36].

### 2.1.1 Signal strength

NMR requires a magnetic field, $\vec{B}_0 = B_0\hat{z}$, created either with permanent magnets or with superconducting coils in spectrometers and imaging systems (MRI). Convention defines the direction of the field as $\hat{z}$ and refers to the $\hat{x}$–$\hat{y}$ plane as the transverse plane.

A small sample place inside a magnetic field will have a nuclear magnetization, $\vec{M}_0 = M_0\hat{z}$, in the same direction as the magnetic field. This magnetization can be

rotated by means of an oscillating magnetic field, $\vec{B}_1(t)$, that is perpendicular to the static field, $\vec{B}_0$, and at a specific frequency called the Larmor frequency, $\omega_0 = \gamma B_0$. The constant of proportionality, $\gamma$, is the gyromagnetic ratio and depends on the nucleus. Hydrogen, specifically $^1$H, has a gyromagnetic ratio of $2.675 \times 10^8\,\mathrm{s^{-1}\,T^{-1}}$ or $42.57\,\mathrm{MHz\,T^{-1}}$. The nuclear magnetization of a small sample with spin number $\mathbf{I} = \frac{1}{2}$ in a magnetic field, $B_0$, is given by,

$$M_0 = \frac{\gamma^2 \hbar^2}{2k_B} \frac{N B_0}{T}, \tag{2.1}$$

where the sample contains $N$ protons at a temperature, $T$; $\hbar$ is the reduced Planck constant; and $k_B$ is the Boltzman constant. Equation (2.1) gives clear guidance on increasing the magnetization: increase the sample size, increase the field strength, and lower the temperature. An implantable sensor goes against all of these. The sensor must be small, the remote measurement limits the field strength, and the temperature is fixed at 37 °C. It is these constraints on the sample that require an on board circuit.

An oscillating field applied perpendicularly to $\hat{z}$, such as,

$$\vec{B}_1(t) = B_1 \sin(\omega_0 t)\hat{x}, \tag{2.2}$$

perturbs the nuclear magnetization, $\vec{M}$, away from equilibrium. The transverse component, $\vec{M}_{xy} = \vec{M} \times \hat{z}$, will precess around $\hat{z}$ at a frequency equal to the Larmor frequency.

Much like music on an AM radio station, there is a slowly varying signal of interest on a high frequency carrier. It is desirable to eliminate the high frequency term,

$\sin(\omega_0 t)$. A rotating reference frame is applied such that the oscillating field can be described only by its time-varying magnitude and a phase term. The oscillating field is turned on momentarily and rotates $\vec{M}$ at a rate, $\omega_1 = \gamma B_1$, around the $x$ axis. The angle of rotation, $\phi$, is given by

$$\phi = \omega_1 t = \gamma B_1 t \tag{2.3}$$

Two useful pulses are those that rotate the magnetization by 90° and 180°. The first rotates the magnetization onto the transverse plane and satisfies the condition $\gamma B_1 t_{90} = \pi/2$. The second condition is simply twice the pulse area, $\gamma B_1 t_{180} = \pi$, and rotates the magnetization into the negative longitudinal direction, $\vec{M} = -M_0 \hat{z}$.

The component of the magnetization in the transverse plane precesses around $\hat{z}$ and induces a voltage in a loop of wire around the sample. Faraday's law of induction states that the voltage is proportional to the time rate of change of the magnetic flux. Conveniently, the magnetic flux can be calculated by, $M_0 \tilde{B}_1$, where $\tilde{B}_1$ is the magnetic field at the sample generated by unit current through the loop[31].The induced voltage is

$$v_{\mathrm{NMR}} = \omega_0 M_0 \tilde{B}_1 \tag{2.4}$$

where the frequency factor, $\omega_0$, is due to the time derivative of the oscillating magnetization[30]. This voltage will be measured by the coil, and the coil design is also important. A wire loop carrying unit current has a magnetic field at the center equal to

$$\tilde{B}_1 = \frac{\mu_0}{2r} \tag{2.5}$$

where $r$ is the loop radius[38]. If the sample size is fixed, the coil should be as small as the sample allows to maximize the induced voltage.

The underlying assumptions are that the sample is uniform, the magnetic field is constant, and the oscillating field is also of uniform magnitude. A spherical sample in a long coil would certainly qualify. A small coil completely filled with sample will have regions of lower field near the ends that cannot be ignored. The signal can be calculated by first dividing the sample into many smaller samples. Each sample is assumed to be uniform, and the contribution from each will be summed to give the overall signal.

### 2.1.2 Relaxation

Various mechanisms are responsible for how the magnetization returns to equilibrium after it has been perturbed with the oscillating field[39, 40]. Two relaxation time constants appear in Bloch's equations and are referred to as the spin-lattice or longitudinal relaxation time, $T_1$, and the spin-spin or transverse relaxation time, $T_2$. When a sample is initially placed in a magnetic field, the nuclear magnetization develops over time as follows:

$$\vec{M}(t) = \hat{z} M_0 \left(1 - e^{-t/T_1}\right). \tag{2.6}$$

A 90° pulse rotates the magnetization into the transverse plane, so $M_{xy} = M_0$ and $M_z = 0$. The transverse component decays towards zero and is given by

$$M_{xy}(t) = M_0 \exp^{-t/T_2}, \tag{2.7}$$

while the longitudinal component returns to equilibrium following the previous equation.

There is an assumption of a perfectly homogeneous magnetic field, but in reality this is rarely the case. Slight variations in the magnetic field across the sample result in a spatially varying Larmor frequency. If a 90° pulse is applied along $\hat{x}$ at time, $t = 0$, the magnetization is rotated into the $\hat{y}$ direction. The precession continues for a brief period of time, $\tau$. If the field variation across the sample is $\Delta B$, then a phase variation develops equal to

$$\Delta\phi = \gamma\tau\Delta B. \tag{2.8}$$

Hahn discovered that applying a 180° pulse in this state could correct for this deviation[41]. This 'refocusing pulse' effectively multiplies the phase by minus one. The fastest precessing regions that had gained phase $+\phi$ now have phase $-\phi$ and vice versa for the slowest regions. The phase continues to accumulate, and at a time $t = 2\tau$ there will be no phase variation across the sample. This momentary constructive interference is detected as an 'echo' by the receiver. Carr and Purcell extended this work to allow for a train of pulses and echoes to measure relaxation time[42]. Meiboom and Gill modified this to eliminate compounding errors due to imperfections in the oscillating field[43]. The CPMG sequence is used almost exclusively in systems with inhomogeneous fields and is shown schematically in figure 2-1. If the initial 90° pulse is along $\hat{x}$ then the 180° pulses are alternately applied along $+\hat{y}$ and $-\hat{y}$. This ensures that any imperfections in the oscillating field do not accumulate from one echo to the next. The peak of each echo is stored, and the decaying envelope gives the material's inherent relaxation rate. Appendix A discusses an acquisition modification used to increase the signal-to-noise ratio by using a least-squares estimate on the entire acquired echo.

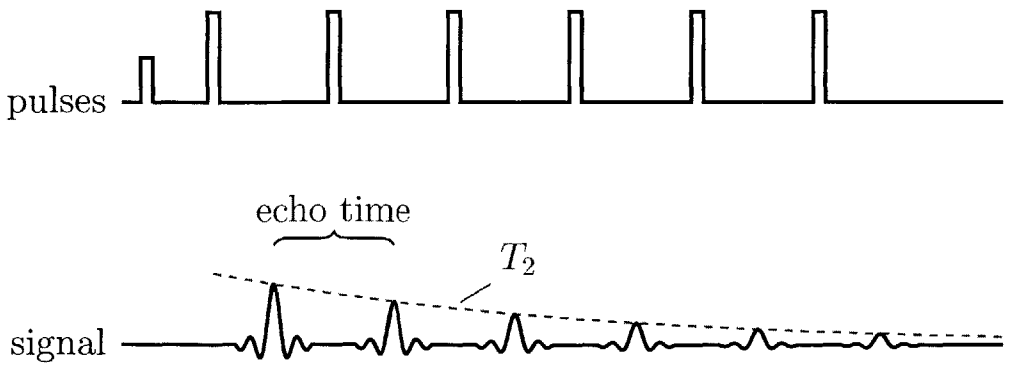


Figure 2-1: Transverse relaxation is measured using the CPMG pulse sequence. A 90° pulse rotates the magnetization into the $x-y$ plane. A train of refocusing pulses compensates for field inhomogeneities and the signal appears as brief "echoes". The envelope of the echo amplitudes (dashed) decays with a time constant, $T_2$.

Measuring longitudinal relaxation requires a different set of pulse sequences. The nuclear magnetization is orders of magnitude smaller than the applied field and so it is preferable to rotate the magnetization into the transverse plane for detection. Saturation recovery is the preferred method for measuring $T_1$ on systems with a grossly inhomogeneous magnetic field, such as the NMR-MOUSE[44, 45]. The sequence starts with a series of pulses that saturate the magnetization such that the net magnetization equals zero. The magnetization is allowed to recover for a time, $\tau$, at which point a spin-echo method is applied to measure $M_z(\tau)$. The sequence, shown in figure 2-2, is repeated for several different recovery times, and the full relaxation profile is acquired. Multiple echoes can be acquire, instead of just one, using the CPMG pulse sequence. This improves the estimate of $M(\tau)$[46].

Contaminants in a sample that perturb the field in their immediate vicinity can increase the relaxation rate. These contaminants could be regions of different permeability such as magnetic particles, bubbles, or paramagnetic species such as oxygen or gadolinium. The relaxation rates are often proportional to concentration.

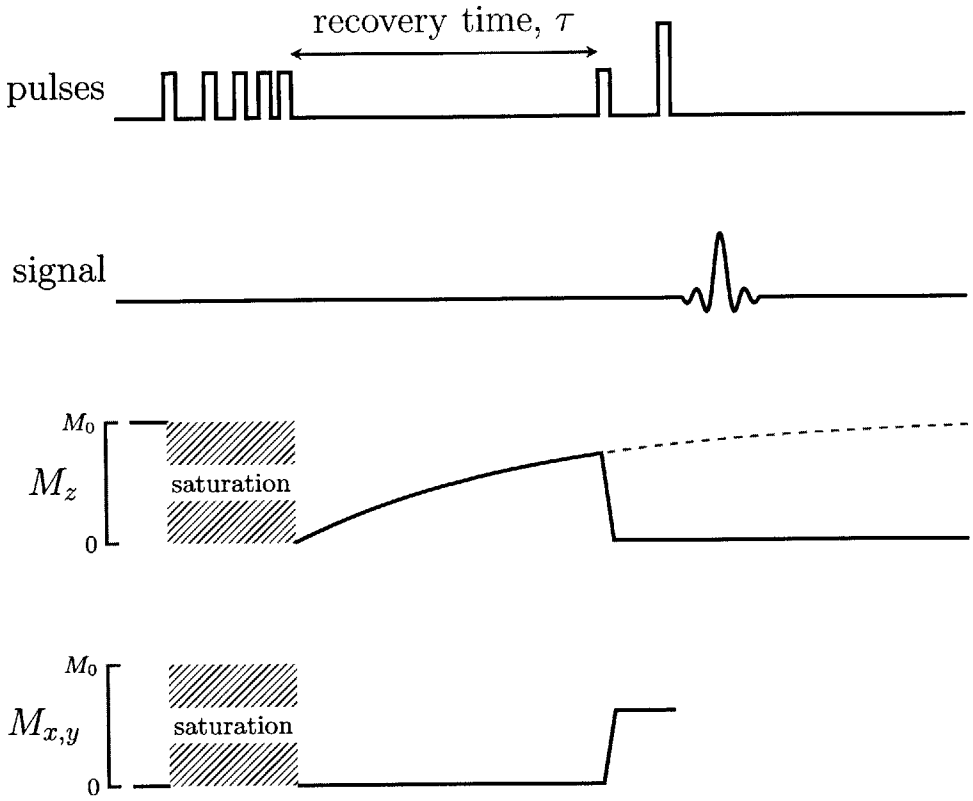


Figure 2-2: Saturation Recovery measures the longitudinal, or spin-lattice relaxation. A burst of pulses with decreasing intervals completely saturate the magnetization such that the net is zero. The system is allowed to recover for a time *tau* during which the $z$-directed magnetization approaches the equilibrium magnetization, $M_0$. The relaxation is interrupted with a spin-echo sequence to generate an echo with $M(\tau) = M_0(1 - e^{-\tau/T_1})$. The relaxation time, $T_1$, is measured by repeating the sequence for different recovery times.

The relaxation-concentration curves can be used as sensors. Magnetic nanoparticles tagged with antibodies form the basis of the contrast agents used in Chapter 6 for measuring soluble protein biomarkers. Chapter 4 deals with an oxygen sensor that exploits relaxation induced by paramagnetic oxygen in solution. Chemical exchange is a process by which hydrogen atoms on a polymer can be exchanged with hydrogen atoms on nearby water molecules. The rate of exchange is pH dependent and influences the measured relaxation rate. A relaxation-pH relationship arises that is used as a pH sensor in Chapter 5. The mechanisms are discussed in their respective chapters.

### 2.1.3 Hardware

Typically, in pulsed NMR, a single coil generates an oscillating magnetic field to manipulate the nuclear magnetization and also detects the NMR signal. A radio frequency (RF) switch inside the NMR spectrometer (KEA2, Magritek) alternately connects the coil to a power amplifier to generate the pulses and to a sensitive preamplifier to receive the echoes. The pulses typically last less than 10% of the overall duration allowing ample time for the oscillation to die down and for the switch to connect the preamplifier to detect the NMR signal[26, 27].

Two permanent-magnet systems are used in the experiments described here. A benchtop relaxometer (Minispec mq-20, Bruker) is used for testing samples in standard 5 mm glass tubes. The samples are inserted through a port in the top of the instrument and sits between two magnets. The arrangement creates a relatively uniform magnetic field with a Larmor frequency of 19.95 MHz.

A second system is a single-sided magnet (NMR-MOUSE, Magritek, Wellington, New

Zealand) that measures samples that are outside the instrument. The field, which runs parallel to the surface, decreases with distance away from the surface. The sensitive region is a flat sheet of sample approximately 250 µm thick. This magnet is particularly useful for measuring samples that won't fit into a traditional instrument. The magnet arrangement is shown in the cutaway view in figure 2-3. The field has a built in field gradient that allows the slice selective measurement. However, this gradient adversely affects the transverse relaxation measurements. Molecules diffusing along the direction of the gradient experience a changing Larmor frequency and a random accumulation of phase. The CPMG sequence cannot fully compensate for this phase accumulation, and the measured $T_2$ is significantly lower than on a homogeneous field magnet.

The figure also shows a rapid NMR screening system, dubbed the AutoNMR, that is designed to measure samples in standard plate format. A modular frame connected to a 3-axis motion stage allows for up to 168 samples to be measured sequentially. A circulating water bath maintains a constant magnet temperature to avoid a drift in the field strength over the course of a day. Custom software controls the robot and programs the pulse sequences.

## 2.2 Resonant Circuits

It is merely coincidence that a resonant circuit is used to detect the nuclear magnetic resonance signal. An untuned coil can measure the signal, but a circuit with a resonance frequency equal to the Larmor frequency greatly improves the signal-to-noise ratio[47, 48]. The inductor-capacitor circuit acts as a filter that rejects all signals except those at the frequency.

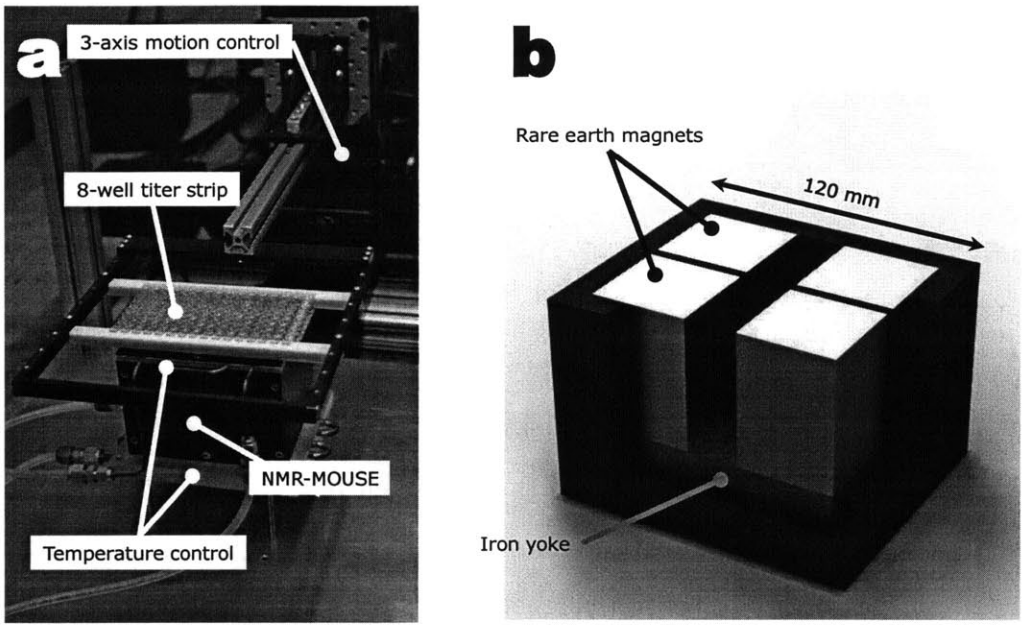


Figure 2-3: Plate format NMR (left) combines a commercially-available single-sided NMR probe with a 3-axis robot. The NMR MOUSE measures a thin slice above the surface thanks to its unconventional magnet arrangement shown on the right.

A capacitor, $C$, is connected with an inductor, $L$, in series as shown in figure 2-4. A resistor, $R$, captures the resistance of the inductor. This RLC circuit has a resonant frequency,

$$\omega_0 = \frac{1}{\sqrt{LC}}. \tag{2.9}$$

A sinusoidal driving current at the resonant frequency, $i(t) = \sin\omega_o t$, will cause

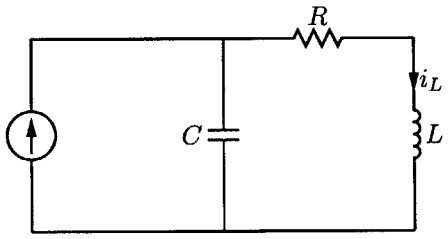


Figure 2-4: An RLC circuit models the capacitor-inductor circuit with the resistor representing the losses in the inductor. At very low frequency the resistance is R, while at high frequency the capacitor shorts out the current source.

an oscillating current inside the inductor that increases in amplitude over time as shown in figure 2-5. The energy from the source current slowly builds up inside the resonant circuit. The energy is stored in the electric field of the capacitor when $v_C(t)$ is maximum or in the inductor's magnetic field when $i_L(t)$ is maximum. Energy is dissipated in the resistor as the current flows in the circuit. The current and voltage build up until the energy dissipated in each cycle equals the energy supplied by the source. The quality factor, $Q$, is defined as the ratio of stored energy to dissipated energy and roughly corresponds to the number of cycles before the oscillations die down once the power is turned off. It also represents a measure of voltage or current gain. The system will always be driven at a fixed frequency, and, thus, it is most convenient to look at the frequency response of the resonator. The peak in the Bode plot (figure 2-6) shows the resonance behavior ($\omega = \omega_0$) very clearly as a tall

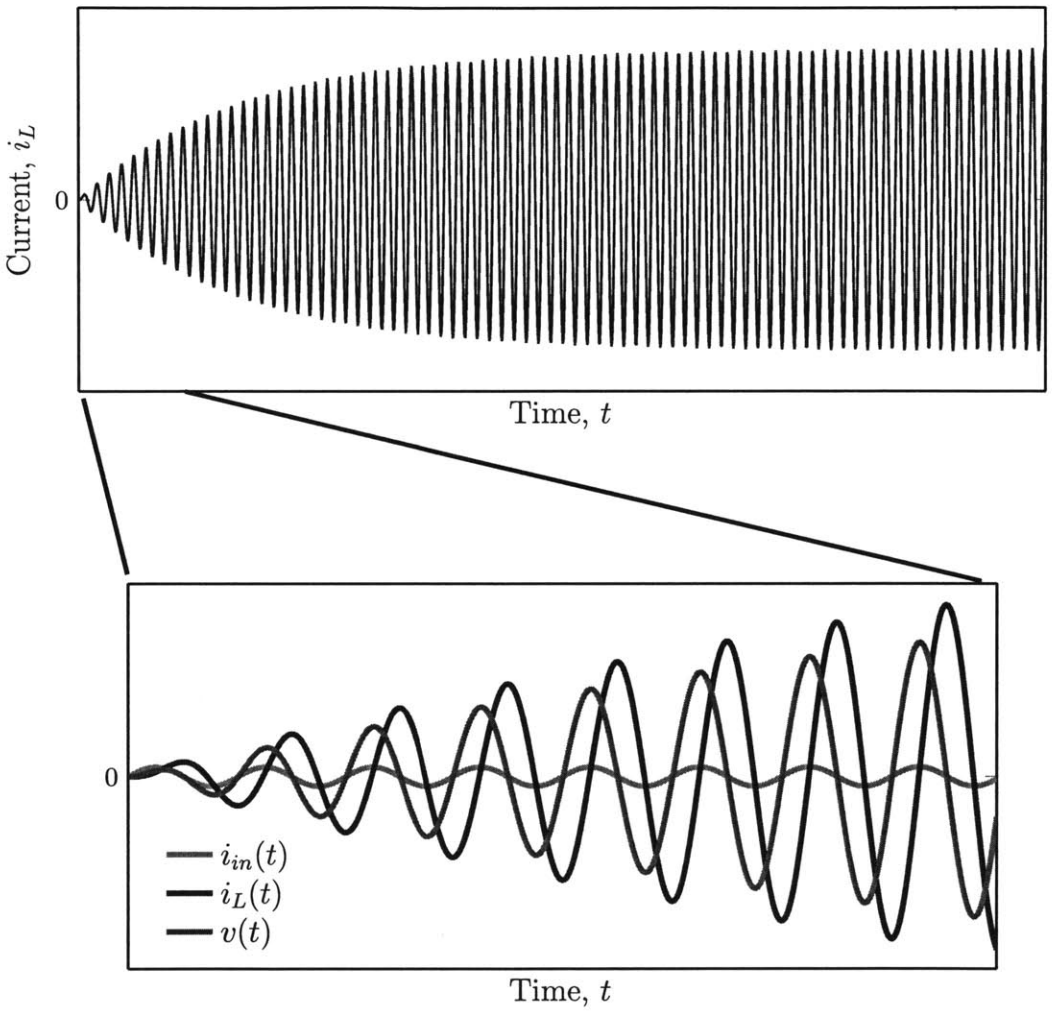


Figure 2-5: Response of the RLC circuit to a current input

peak. Low frequency signals flow through the inductor, whereas high frequency input signals are shorted by the capacitor.

The oscillating magnetic field inside the coil creates a radial gradient in the current density according to Faraday's law [49, p.3]. Solving in cylindrical coordinates yields a diffusion equation in the magnetic field $H_z$ of the form:

$$\frac{1}{\mu\sigma\omega r}\frac{d}{dr}rJ_\phi(r,\omega) = H_z(r,\omega), \tag{2.10}$$

$$-\frac{dH_z}{dr} = J_\phi. \tag{2.11}$$

Equation (2.11) shows a characteristic $1/\mu\sigma\omega r$ drop off in the current density perpendicular to the coil axis. The current flows along the inner surface of the coil. The concentrated current flows over a narrower cross-section of wire, and the resistance will be higher than the length and conductivity would predict. The equations are solved numerically using finite element software (COMSOL v. 4.3a, COMSOL Inc., Burlington, MA). The simulation calculates the field generated by a coil as well as its circuit model parameters. The field plots of figure 2-7 correspond to the model parameters in table 2.1.

The current density distribution inside the wires is shown in figure 2-8 at 2 MHz and at 20 MHz. The current is spread out throughout the wire's cross section at low frequency, but it becomes more concentrated near the inner surface as the frequency is increased.

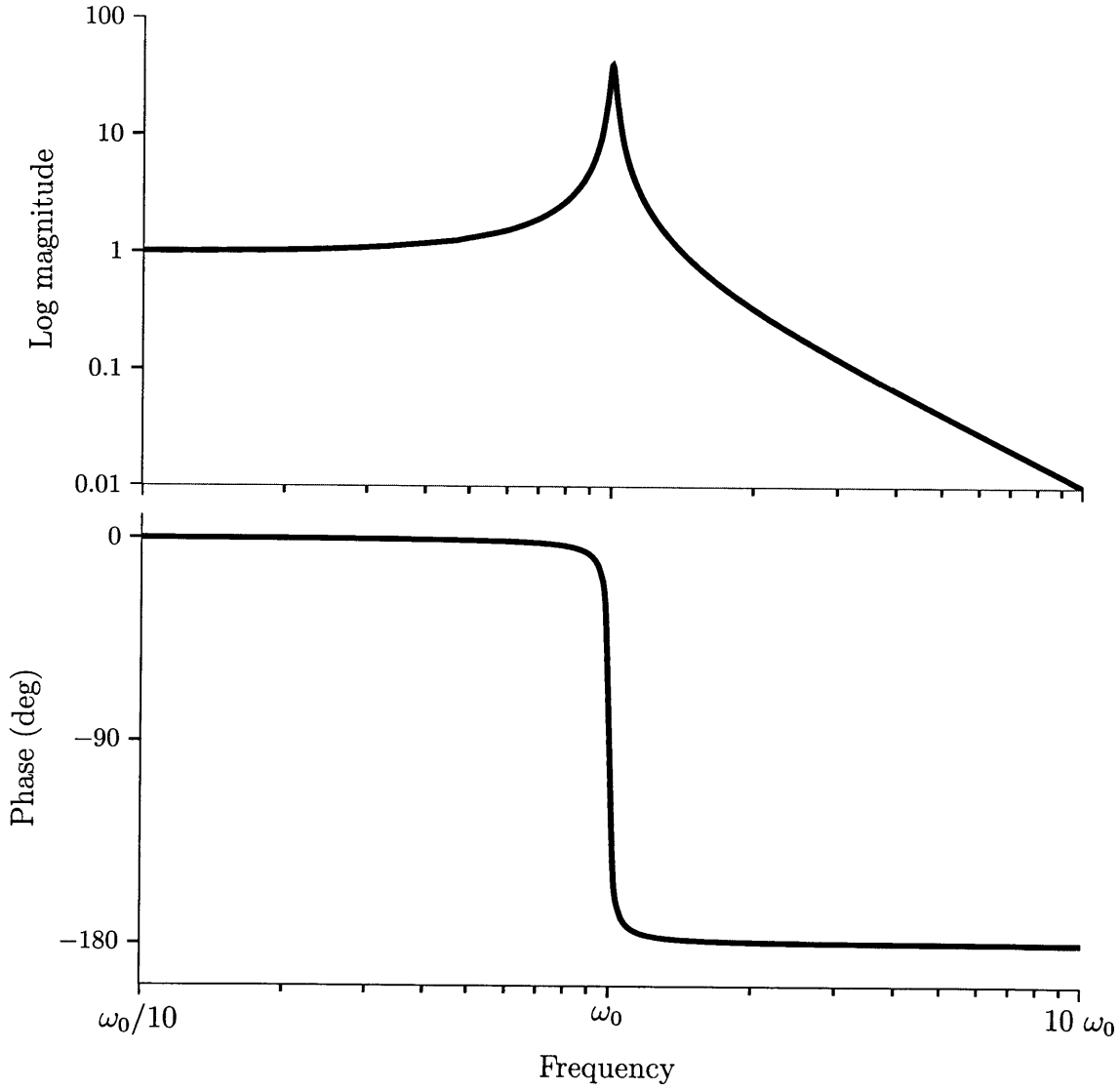


Figure 2-6: Frequency response of an RLC circuit

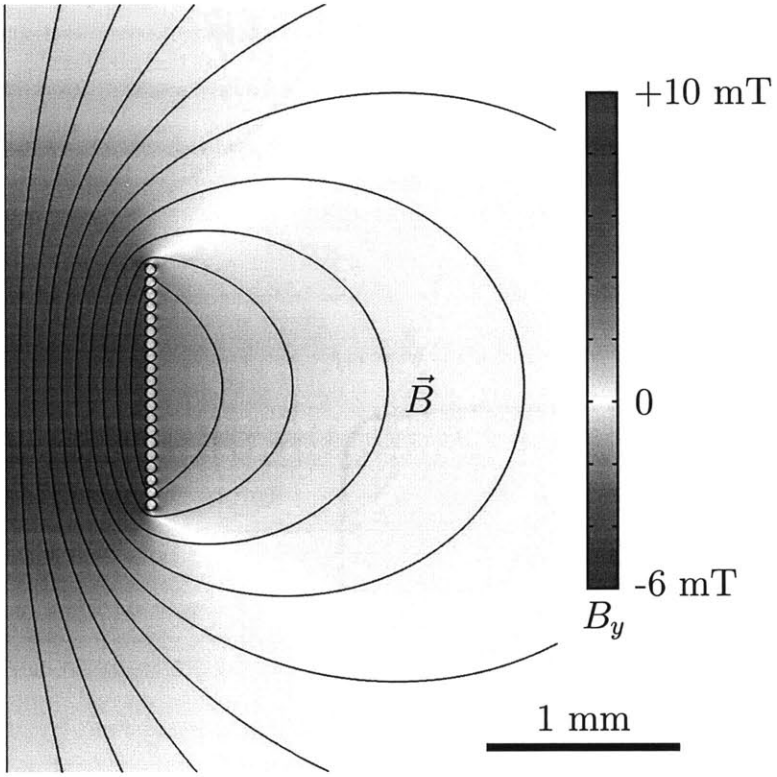


Figure 2-7: Two dimensional simulation of magnetic field in cylindrical coordinates $\hat{y} - \hat{r}$. A 20 turn coil is modeled with 1 A current flow. The field lines show the direction of $\vec{B}$, and the color represents the magnitude of the $\hat{y}$ directed field.

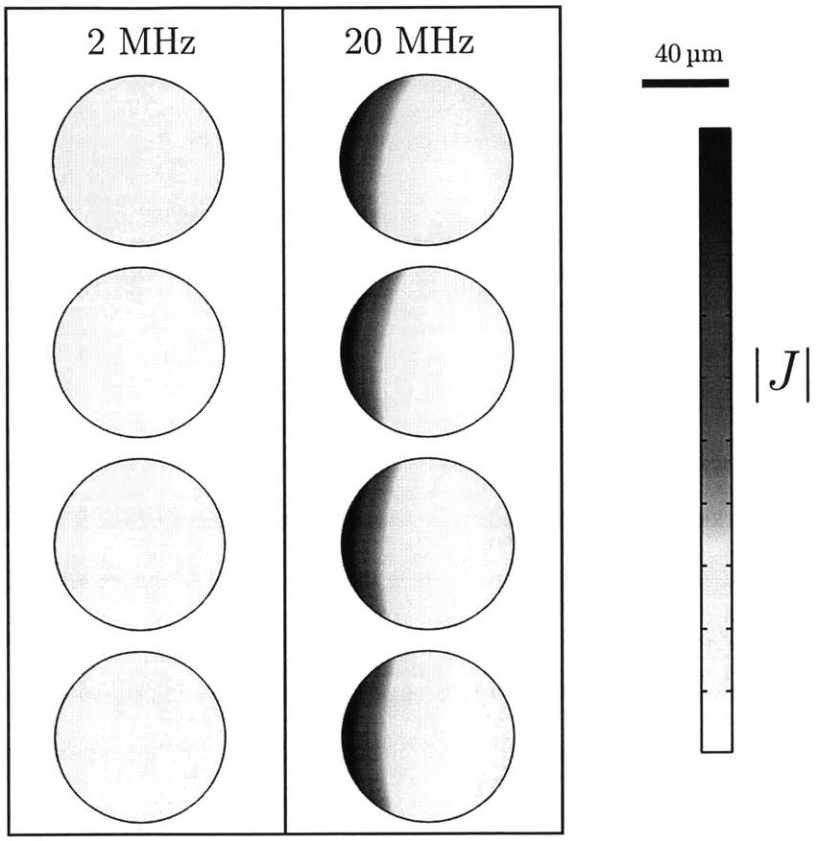


Figure 2-8: Two dimensional cross section of current distribution. The images are cylindrically symmetric about the left side of the page. The coil has a larger resistance at high frequency because the current flows mostly on the inner surface of the coil.

| Parameter | Value | Description |
|---|---|---|
| $f_0$ | 20 MHz | frequency |
| $N$ | 20 | number of turns |
| $d_{coil}$ | 1.8 mm | coil diameter |
| $r_{wire}$ | 40 µm | wire radius |
| $s$ | 92 µm | turn spacing |
| $I$ | 1 A | current |
| $L$ | 590 nH | inductance |
| $R$ | 1.7 Ω | a.c. resistance |
| $Q$ | 44 | quality factor |
| $B\|_{(0,0)}$ | 9 mT | field at the center |

Table 2.1: Simulation parameters and outputs for a 20-turn coil.

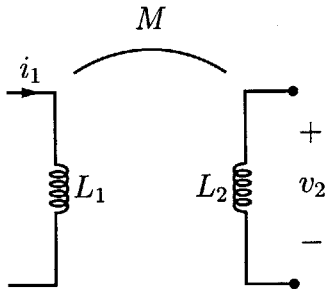


Figure 2-9: Mutual inductance represented in a circuit diagram.

## 2.3 Mutual Induction

Mutual inductance from a circuit perspective is the voltage induced in one conductor as a result of a changing current in a second conductor. The circuit diagram represented has two inductors, $L_1$ and $L_2$, with a mutual inductance between them, $M$, as shown in figure 2-9. Four equations relate the currents through the two inductors

to the voltages across them:

$$v_1 = L_1 \frac{di_1}{dt} \tag{2.12}$$

$$v_2 = L_2 \frac{di_2}{dt} \tag{2.13}$$

$$v_2 = M_{12} \frac{di_1}{dt} \tag{2.14}$$

$$v_1 = M_{21} \frac{di_2}{dt}. \tag{2.15}$$

Calculating the mutual inductance between two coils (see figure 2-10) requires knowledge of their geometry and relative orientation. Faraday's original experiments showed that a changing magnetic flux through a wire loop will induce a electromotive force around the loop. The changing magnetic flux is generated by the alternating current in a nearby coil[50]. Expressed mathematically the voltage in the loop is given by,

$$v = -\frac{d\Phi}{dt}, \tag{2.16}$$

where $\Phi$ is the magnetic flux through the loop. If this flux is generated by current, $i$, flowing in another conductor, then the mutual inductance is

$$M = \frac{\Phi}{i}. \tag{2.17}$$

The flux can be calculated by integrating the magnetic flux density, $\vec{B}$, over the surface, $S$, bound by the loop

$$\Phi = \iint_S \hat{n} \cdot \vec{B} dS, \tag{2.18}$$

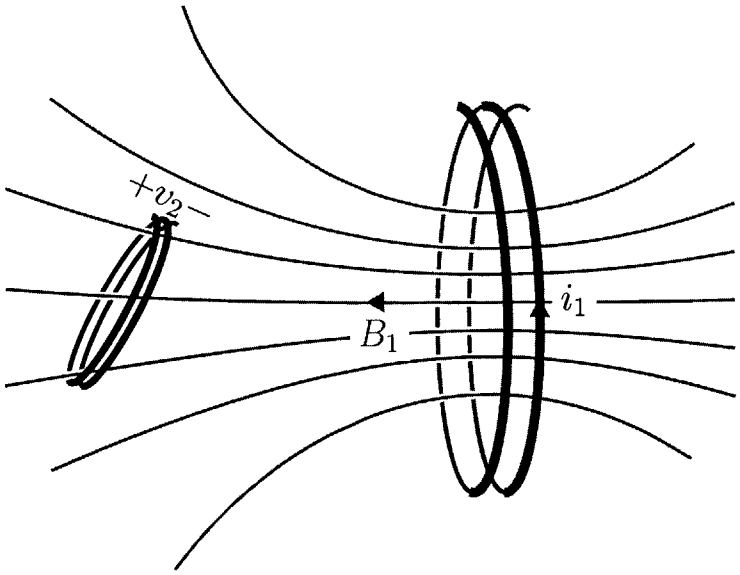


Figure 2-10: The field generated by a changing current in one coil induces a voltage, $v_2(t) = -M\frac{di_1}{dt}$, in a nearby coil.

where $\hat{n}$ is the normal to each differential surface element, $dS$[38]. This approach has two drawbacks. The field, $\vec{B}$, is calculated using the Biot-Savart equation at each differential surface element. This is computationally expensive because the magnetic field would need to be calculated at many points in the three dimensional space bound by the second coil. The second drawback is that it is not obvious where there the surface, $S$, lies.

The magnetic vector potential offers a much faster and cleaner approach. Conventionally denoted by $\vec{A}$, it is related to the magnetic flux density as follows,

$$\nabla \times \vec{A} = \vec{B}. \tag{2.19}$$

Stokes' theorem provides a way of converting the surface integral of $\vec{B}$ into a line

integral of $\vec{A}$, such that,

$$\iint \hat{n} \cdot \nabla \times \vec{A} dS = \oint \vec{A} \cdot d\vec{l}, \tag{2.20}$$

where $\vec{l}$ is the line bounding the surface $S$[51]. That line is the coil through which we want to calculate the flux. The vector potential from a line current, $C$, at a point in space, $\vec{p}$, is given by,

$$\vec{A}(\vec{p}) = \frac{\mu_0}{4\pi} \int_C \frac{\vec{I} dl}{r}, \tag{2.21}$$

where $r$ is the distance from the point $\vec{p}$ to the point along $C$ [38].

The mutual inductance between two coils can be calculated by integrating the vector potential $A$ along the second coil $C_2$. Combining Equations 2.17, 2.18, and 2.20 yields,

$$M = \frac{1}{i} \oint_{C_2} \vec{A} \cdot d\vec{l}, \tag{2.22}$$

which combined with equation (2.21) gives,

$$M = \frac{\mu_0}{4\pi i} \int_{C_2} \int_{C_1} \frac{I d\vec{l}_1}{|\vec{r_1} - \vec{r_2}|} \cdot d\vec{l_2} \tag{2.23}$$

where $\vec{r_1}$ and $\vec{r_2}$ are points along $C_1$ and $C_2$. The circular integrals can be omitted knowing that $C_1$ and $C_2$ will be closed loops when connected in a circuit. Rearranging the terms yields a simplified form,

$$M = \frac{\mu_0}{4\pi} \int_{C_2} \int_{C_1} \frac{d\vec{l}_1 \cdot d\vec{l_2}}{|\vec{r_1} - \vec{r_2}|}. \tag{2.24}$$

The calculation of $M$ is now reduced to an integration over two known paths. The

subscripts are interchangeable without any change in the form of the equation. This symmetry proves that there is only one mutual inductance between two coils.

Many papers exist that analytically solve for $M$. The simplest configuration involves two circular loops, and the calculation involves using parametric tables[52]. There are six degrees of freedom associated with the relative position of two wire loops of arbitrary shape. The simplest approach is to calculate the integral in equation (2.24) numerically as described in Appendix B. This method is extremely fast even on a modest computer.

## Summary

This chapter introduced three topics that will be combined to perform wireless NMR measurements inside the body. NMR contrast agents are exploited to give chemically-sensitive relaxation rates. The signal is contained in a very narrow band around the Larmor frequency and is efficiently detected with a resonant coil, which acts as a band-pass filter. Chapter 3 will introduce two coils linked through their mutual inductance. The NMR measurement is performed inside the sensor coil that is implanted in the body. The reader coil resides outside the body and provides the connection to the spectrometer.

# Chapter 3

# Wireless NMR

The wireless NMR system consists of two distinct components: a sensor that is implanted in the body and a reader that resides outside the body. Both the sensor and the reader contain a resonant coil, and they are linked to each other through their mutual inductance. The NMR measurement is performed only on the contents of the sensor with very little interference from the surrounding tissue. This chapter presents the theoretical framework for wireless NMR detection with special considerations made for measurements in living tissue. The design specifically addresses the precise manufacture of large quantities of sensors that are needed for in vivo testing.

## 3.1 Magnetic field amplification

A sinusoidally varying magnetic field induces a voltage across a coil. If that coil is part of a resonant circuit tuned to the field's oscillation frequency then there will be a gradual build up of current in the coil. Unlike the directly driven resonator shown

in Figure 2-5, the transfer of energy is achieved wirelessly.

The simplest case models a small coil, $L_S$, located at the center of a larger coil, $L_R$. The small coil has a finite resistance, $R_S$, and is tuned with a capacitor, $C_S$, to a resonant frequency, $\omega_0 = 1/\sqrt{L_S C_S}$. The large coil is driven by an infinite impedance current source and is not tuned. The time varying current is given by,

$$i_R(t) = e^{j\omega_0 t}, \tag{3.1}$$

where $j = \sqrt{-1}$. The mutual inductance between the two coils results in an induced voltage in the second coil,

$$v_S(t) = M\frac{d}{dt}e^{j\omega_0 t} = j\omega_0 M e^{j\omega_0 t}. \tag{3.2}$$

The circtui has an impedance equal to $R$ on resonance. The current in secondary coil is given by,

$$i_S(t) = \frac{v_S(t)}{R} = \frac{j\omega_0 M}{R}e^{j\omega_0 t}. \tag{3.3}$$

The two coils will each contribute to the magnetic field in space. The total magnetic field, represented in cylindrical coordinates, is calculated by superposition,

$$\vec{B}(r, y, \phi, t) = i_S(t)\tilde{B}_S(r, y, \phi) + i_R(t)\tilde{B}_R(r, y, \phi), \tag{3.4}$$

where $\tilde{B}$ refers to the field generated by unit current in each coil. The field along $\hat{y}$ is the most relevant for an NMR experiment since the static magnetic field, $\vec{B}_0$, is directed along $\hat{z}$. Substituting for the currents in Equation (3.3) and Equation (3.1),

the total field is given by,

$$B_y(r,y,t) = \frac{j\omega_0 M}{R} e^{j\omega_0 t}\tilde{B}_{Sy}(r,y) + e^{j\omega_0 t}\tilde{B}_{Ry}(r,y), \tag{3.5}$$

where components along $\hat{\phi}$ are ignored because of cylindrical symmetry. It is also convenient to multiply by $e^{-j\omega_0 t}$ to eliminate the explicit time dependence. The sinusoidal steady state field is given by,

$$B_y(r,y) = \frac{j\omega_0 M}{R}\tilde{B}_{Sy}(r,y) + \tilde{B}_{Ry}(r,y). \tag{3.6}$$

Taking the real and imaginary parts of $B_y$ separately reveals that the two coils are out of phase with each other:

$$\mathbf{Re}\left[B_y(r,y)\right] = \tilde{B}_{Ry}(r,y); \tag{3.7}$$

$$\mathbf{Im}\left[B_y(r,y)\right] = \frac{\omega_0 M}{R}\tilde{B}_{Sy}(r,y). \tag{3.8}$$

Figure 3-1 shows a cross sectional field map of a 40 turn coil of diameter 0.92 mm inside a 14 mm, 12 turn coil. The unit current field strengths are 12 mT and 0.36 mT respectively. The mutual inductance between the two coils is 380 nH. The smaller coil's resistance is 3 Ω. The field amplification for this configuration is,

$$H_B = \frac{\omega_0 M R^{-1}\tilde{B}_{Sy}(0,0)}{\tilde{B}_{Ry}(0,0)} = 52. \tag{3.9}$$

The quality factor of the small coil, $Q_S = \omega_0 L_S/R_S$ equals 49. The coil quality factor can therefore serve as a first order approximation to the field gain.

If the excitation frequency departs from the sensor's resonant frequency, $\omega \neq \omega_0$,

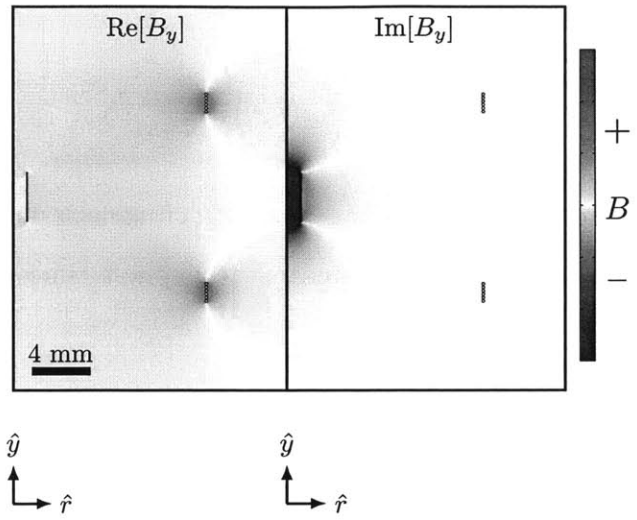


Figure 3-1: A large field amplification occurs if a coil is excited on resonance.

then the field strength inside the sensor is reduced. The bandwidth is determined by the sensor coil's quality factor as shown in Figure 3-2.

Two key advantages derived from the field amplification apply to an implantable sensor. First, the field gain points directly to a boost in the signal-to-noise ratio. Second, the NMR measurement is almost entirely localized to the material inside the sensor. The very low field outside of the sensor implies that very little signal will be detected there. The remainder of this chapter deals with the practical implementation of wireless NMR.

## 3.2 Circuit model

The spectrometer alternately connects the probe to a power amplifier (transmit mode) and a preamplifier (receive mode). Two circuit models are used to describe

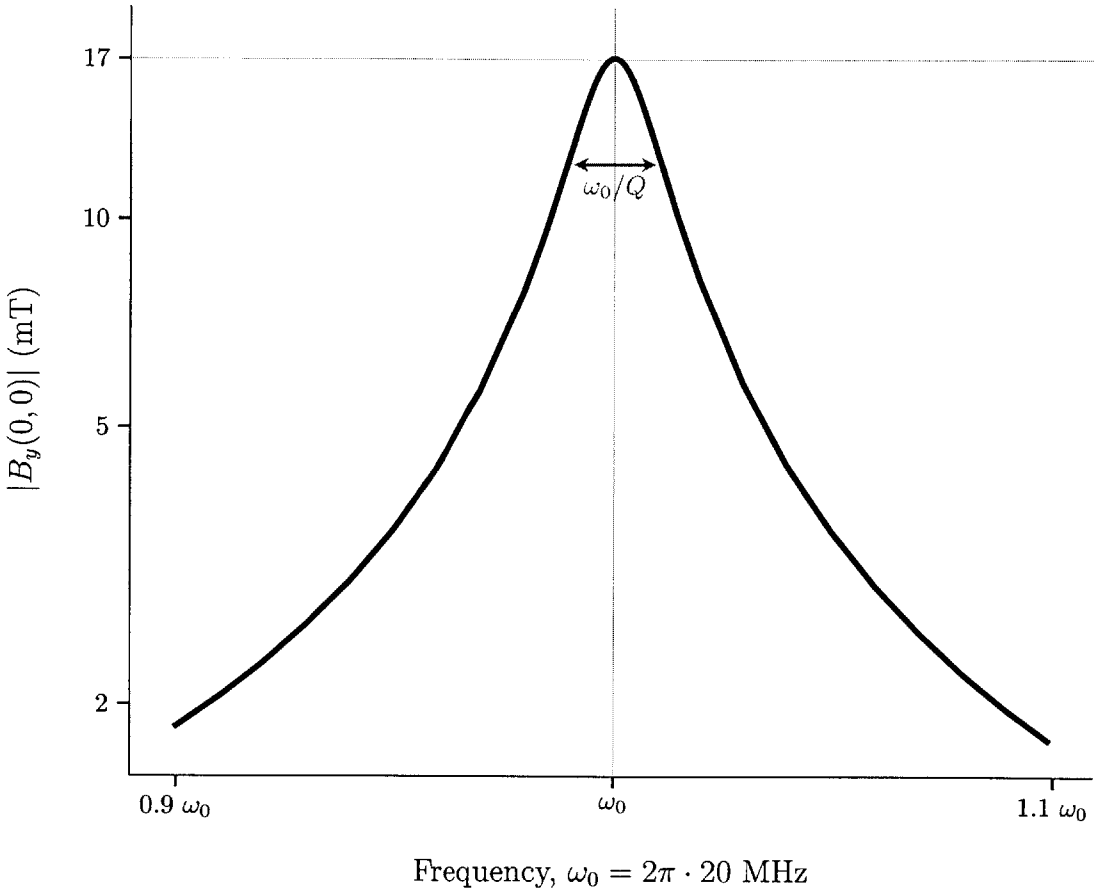


Figure 3-2: The field generated inside the sensor is greatly enhanced when the sensor is excited at the resonance frequency by a current flowing in the reader coil.

the transmit mode and the receive mode separately. The circuit abstraction will yield input-output transfer functions that are used to tune the entire system and to model the signal-to-noise ratio of the experiment. A two-dimensional finite element model calculates the coil parameters, and a three-dimensional computation of the mutual inductance captures the geometric orientation of the two coils. The capacitors are then chosen to maximize the signal-to-noise ratio of the experiment.

Transmission lines are omitted from the circuit analysis because the length is significantly shorter than the wavelength. A 20 MHz wave on a coaxial cable with a propagation velocity equal to 70% the speed of light in vacuum would have a wavelength, $\lambda \approx 10\,\mathrm{m}$. The cable connecting the coil to the spectrometer is 0.3 m long, so no wave effects are modeled. The coaxial cable will introduce a small capacitance, but this will be included in the two variable capacitors on the reader probe.

### 3.2.1 Transmit mode

The circuit diagram in Figure 3-3 shows the transmit path. The spectrometer power amplifier is modeled as a voltage source with an impedance $R_{IN} = 50\,\Omega$. Maximum power transfer is achieved when the probe impedance matches the source impedance. The two capacitors $C_M$ and $C_T$ will be selected to ensure power matching. The two resistors capture the losses in the coils; whereas, the capacitors are assumed to be lossless.

The coupled probes are modeled as a feedback system, which is shown in the block diagram of Figure 3-4. The current flowing in the sensor coil, $I_s$, is the critical circuit parameter during excitation and is placed at the output. The input is the voltage

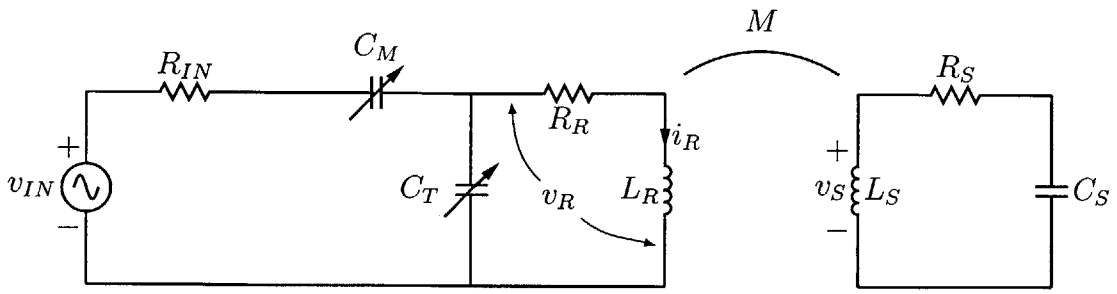


Figure 3-3: Transmit path showing a 50 Ω voltage source connected to the reader probe. The resistors model losses in the coils.

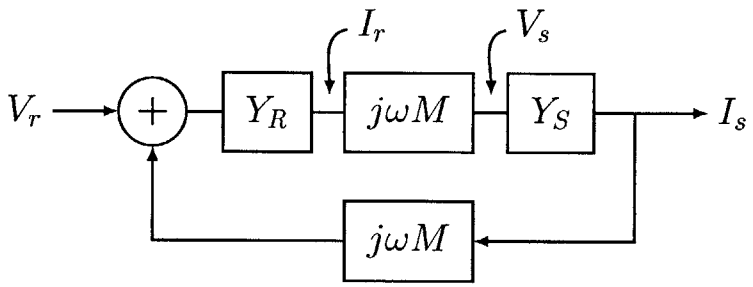


Figure 3-4: Block diagram of the coupled probes. Solution of the feedback loop gives the current in the sensor coil.

across the reader coil, $V_r$. The current through the reader coil is,

$$I_r = V_r Y_R, \tag{3.10}$$

where the reader coil admittance is

$$Y_R = \frac{1}{j\omega L_R + R_R}. \tag{3.11}$$

The resulting magnetic field induces a voltage across the sensor coil, $V_s = j\omega M I_r$. A current, $I_s = Y_S V_s$, flows through the sensor circuit that consists of a series connected

capacitor, inductor and resistor. The sensor admittance is

$$Y_S = 1/Z_S = (j\omega L_S + R + 1/j\omega C_S)^{-1} \tag{3.12}$$

where $1/\sqrt{L_S C_S} = \omega_0$. The feedback loop arises because the sensor current induces a voltage across the reader coil $V_r^- = j\omega M I_s$ that opposes the driving current. Solving the block diagram gives

$$\frac{I_s}{V_r} = \frac{j\omega M Y_R Y_S}{1 + \omega^2 M^2 Y_R Y_S} \tag{3.13}$$

that can be used to calculate the sensor current as a function of the input voltage for any two-coil system.

It is convenient to calculate the admittance $I_r/V_r$ when the two coils are coupled together. The current in the reader coil, $I_r$, is the output of the $Y_R$ block on Figure 3-4. The feedback loop still applies, but the block diagram is rearranged to put $I_r$ at the output. Solving for that node yields a coupled-probe admittance,

$$Y_{CP} = \frac{I_r}{V_r} = \frac{Y_R}{1 + \omega^2 M^2 Y_R Y_S}, \tag{3.14}$$

where the denominator is the same as in Equation (3.12), but the mutual inductance is absent from the numerator. If $M = 0$ then $Y_{CP} = Y_R$, which is the single-coil case. The coupled admittance, $Y_{CP}$, simplifies the circuit to look like a single-coil NMR probe (Figure 3-5).

The tuning and matching capacitors will transform the impedance, $Z_{CP}$, to equal the source resistance and maximize the power transfer from the amplifier. The total

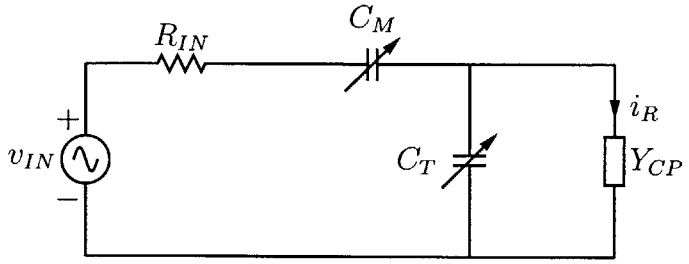


Figure 3-5: Simplified transmit path with the admittance $Y_{CP}$ representing the couple reader-sensor. A single-coil NMR probe has $Y_{CP} = (R + j\omega L)^{-1}$.

complex impedance from the point of view of the power source is

$$Z = \frac{1}{j\omega C_M} + \frac{1}{j\omega C_T + Y_{CP}}. \tag{3.15}$$

The matching capacitor adds only an imaginary component. The tuning capacitor, $C_T$, must be chosen so that the real part of the second term equals the source impedance at the resonant frequency:

$$\mathbf{Re}\left[\frac{1}{j\omega_0 C_M} + \frac{1}{j\omega_0 C_T + Y_{CP}(\omega_0)}\right] = \mathbf{Re}\left[\frac{1}{j\omega_0 C_T + Y_{CP}(\omega_0)}\right] = Z_{in}. \tag{3.16}$$

Solving for $C_T$ yields

$$C_T = -\frac{\mathbf{Im}\left[Y_{CP}\right] + \sqrt{\mathbf{Re}\left[Y_{CP}\right]/Z_{in} - \mathbf{Re}\left[Y_{CP}\right]^2}}{\omega_0}, \tag{3.17}$$

and Equation (3.15) can be rewritten as a sum of real and imaginary components:

$$Z = \frac{-j}{\omega C_M} + j\mathbf{Im}\left[\frac{1}{j\omega C_T + Y_{CP}}\right] + Z_{in}. \tag{3.18}$$

The imaginary parts must sum to zero so that $Z(\omega_0) = Z_{in}$. The capacitance $C_M$ is

the only unknown and is found by solving

$$\frac{1}{\omega_0 C_M} = \mathbf{Im}\left[\frac{1}{j\omega_0 C_T Y_{CP}(\omega_0)}\right]. \tag{3.19}$$

The tune and match capacitors can be calculated for any pair of coils in any orientation. The importance of having the reader and sensor tuned at the resonant frequency cannot be overstated. The tuning and matching capacitors are absolutely necessary to achieve a workable signal-to-noise ratio. Figure 3-6 shows the field inside the sensor coil when driven by a resonant (tuned) reader probe versus an untuned reader.

### 3.2.2 Receive mode

The spectrometer connects the probe to the preamplifier to detect the NMR signal. The circuit diagram is shown in Figure 3-7. The NMR signal appears as a voltage across the sensor coil, $v_{\mathrm{NMR}}$, and is on the order of $10^{-6}$ V. This is weak enough that the thermal noise originating in the resistive elements must be taken into consideration. The noise voltages, $\langle v_{N,S}^2 \rangle$ and $\langle v_{N,R}^2 \rangle$, represent the noise in the sensor coil and the reader coil respectively. The signal, $v_{\mathrm{NMR}}$, and the noise, $v_{N,S}$, both originate in the sensor coil, and they cannot be distinguished from one another. The measured voltage, when the receiver is turned on, is

$$v(t) = \alpha\left[v_{\mathrm{NMR}}(t) + v_{N,S}(t)\right] + \beta v_{N,R}(t), \tag{3.20}$$

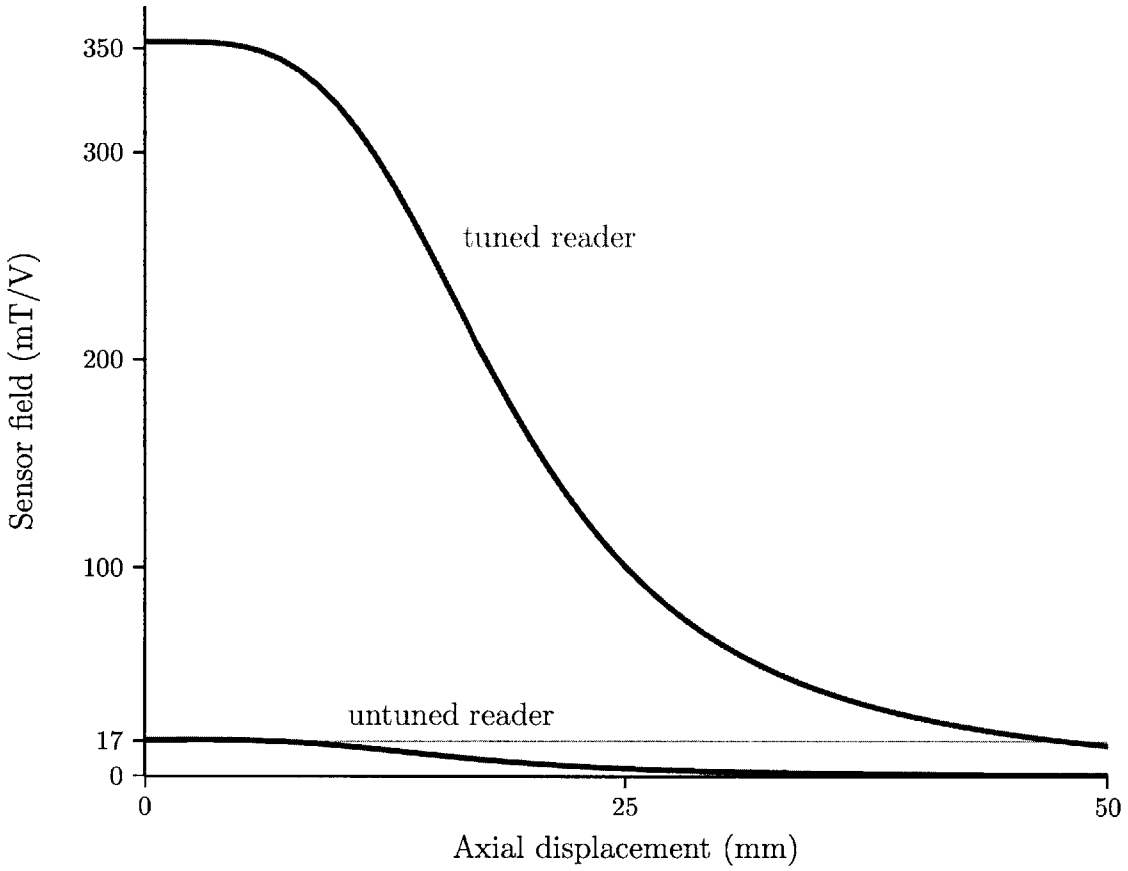


Figure 3-6: Simulation of the field inside the sensor coil as a function of distance from the reader coil. A tuned reader coil increases the field inside the sensor coil more than 20 fold.

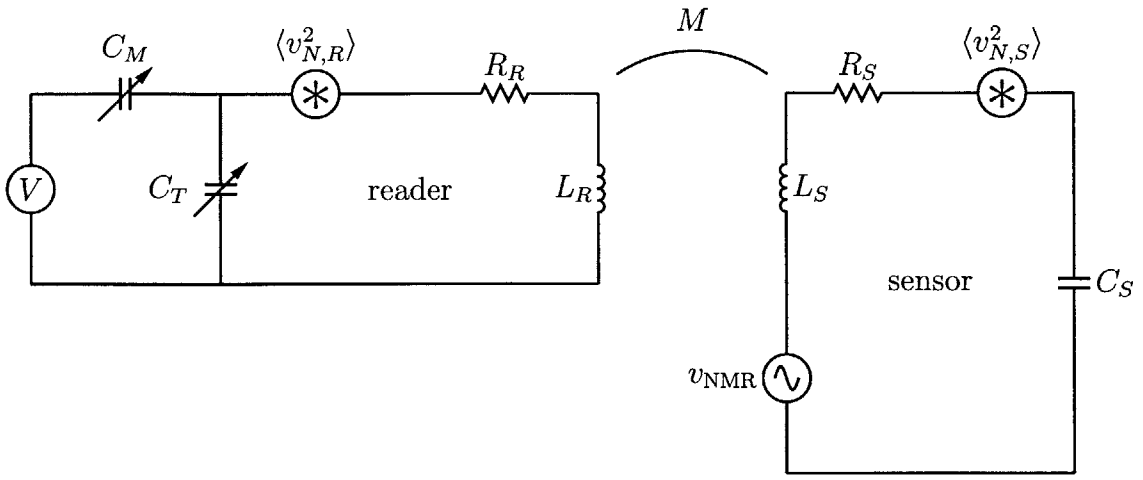


Figure 3-7: Signal reception path. The NMR signal appears as a voltage across the sensor coil. Resistive losses in the coils are modeled as noise sources.

where $\alpha$ and $\beta$ are gain terms to be calculated. Separating the signal terms from the noise terms yields the signal-to-noise ratio,

$$\mathrm{SNR} = \frac{\alpha v_{nmr}}{\alpha\sqrt{\langle v_{n,S}^2 \rangle} + \beta\sqrt{\langle v_{n,R}^2 \rangle}}, \tag{3.21}$$

where the best case scenario is not zero noise, but rather $\mathrm{SNR} = v_{\mathrm{NMR}}/\sqrt{\langle v_{n,S}^2 \rangle}$. This is achieved if the sensor noise is the dominant noise source, that is, if

$$\alpha\sqrt{\langle v_{n,S}^2 \rangle} \gg \beta\sqrt{\langle v_{n,R}^2 \rangle}. \tag{3.22}$$

A well shielded system will be limited by thermal noise, which is a fundamental physical phenomenon. A resistor, $R$, at an absolute temperature, $T$, has a frequency-independent noise spectral density

$$V_n^2 = 4k_B T R, \tag{3.23}$$

where $k_B$ is the Boltzman constant [53]. The time-averaged noise, $\langle v_n^2 \rangle$, depends on the receiver bandwidth [54]. If the resistor is connected in a circuit, a noise current will flow that is given by

$$I^2 = \frac{2k_BTR}{\pi} \int_0^\infty Y^2(\omega) d\omega, \tag{3.24}$$

where $Y$ is the circuit admittance [55]. The resonant circuit acts as a filter with a voltage transfer function, $H(\omega)$. The voltage noise through a transfer function becomes,

$$V^2 = \frac{2k_BTR}{\pi} \int_0^\infty H^2(\omega) d\omega. \tag{3.25}$$

The two relevant transfer functions for calculating the noise in Equation (3.21) are $H_S(\omega)$ and $H_R(\omega)$. These capture the voltage at the receiver due to a voltage in the sensor coil and the reader coil respectively. The NMR signal is calculated using Equation (2.4). This information is used to estimate the signal-to-noise ratio for any coil configuration.

The importance of the tuning and matching capacitors for the transmit mode applies also to the receive mode. Figure 3-8 shows the NMR signal received by a 14 mm diameter reader as it is moved away from a 2 mm sensor coil. The signal strength received by the tuned reader is stronger even at 50 mm away from the remote coil. The sensor noise is also amplified, but the resulting signal-to-noise ratio is still improved by a factor of 200. Schnall and coworkers implanted a large resonant coil inside an animal to improve the image resolution in MRI. The authors used an untuned 'sniffer' coil outside the animal in receive mode only. The MRI volume coil was used for excitation [56]. A resonant reader would have enhanced the sensitivity by several orders of magnitude.

Any applications with coupled coils should have both coils tuned to the same resonant frequency. The power transfer during a transmit mode is maximized and the signal-to-noise ratio during reception are both increased substantially with coupled resonators. This section focused on wireless NMR, but the enhancement applies to any application using coupled coils: the transmit pulse can be used to power a device remotely, and the receiver circuit applies to any signal generated inside the remote coil.

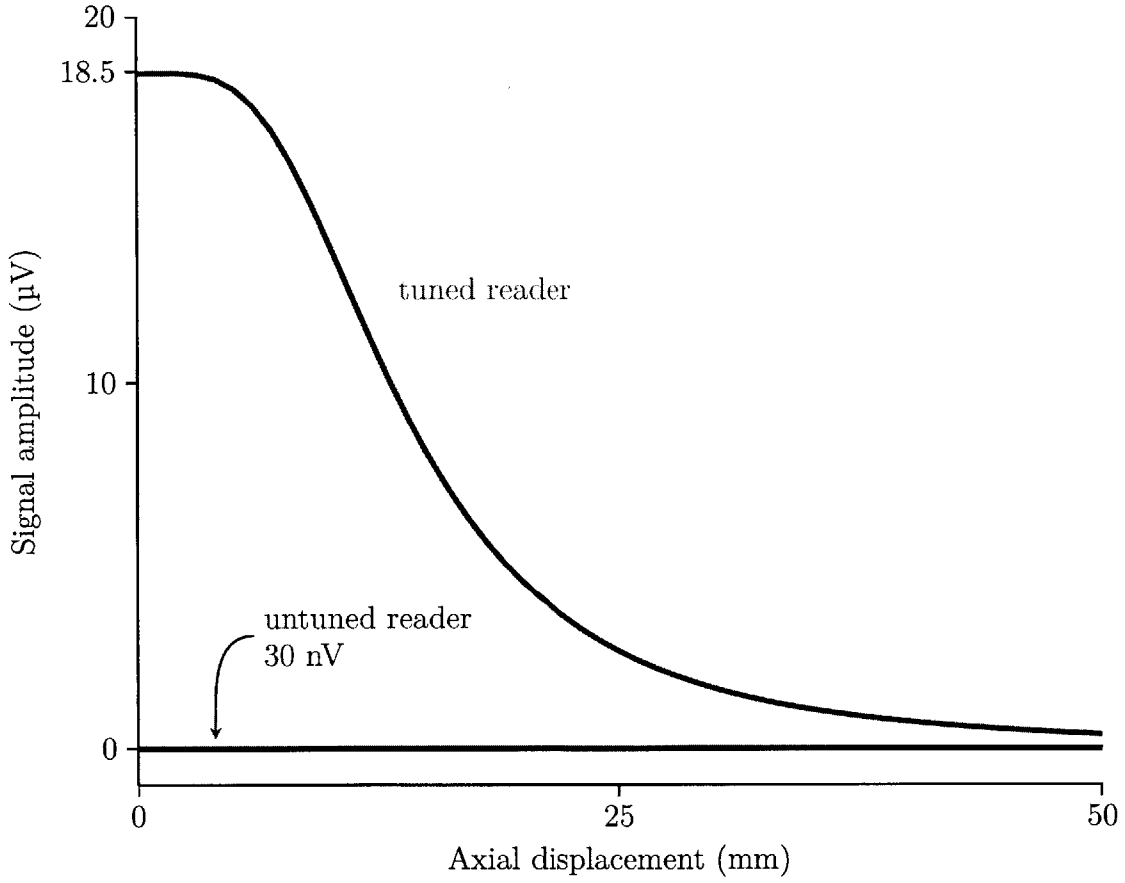


Figure 3-8: A tuned reader coil ensures enhanced reception of the NMR signal.

## 3.3 Design considerations

Designing an NMR probe for an implantable sensor introduces a unique set of requirements. The outer diameter of the sensor must match the bore size of a biopsy needle, and all materials must be suitable for implantation. The reader coil is designed for measuring through living tissue, which is conductive.

### 3.3.1 Sensor length

The sensor should be between 4 mm and 10 mm in length. The minimum length is the smallest practical amount of sample plus the length of the capacitor. The length involves a trade-off between sensitivity and response time. A large sample will give a more sensitive device but increases the time it takes for the analyte to diffuse into the chamber. Radial fluid access would decouple sensitivity and response rate. Allowing fluid access from the sides, however, requires a wider coil pitch, which will decrease the sensitivity. The better choice would be to add fluid access from both sides to the response time by a factor of four.

The coil was chosen to be approximately 4 mm long, making the sensor 6 mm long with the capacitor. A two dimensional field map is shown in Figure 3-9. The coil length is four times the radius and results in a large sensitive volume in the center of the chamber. The outlined box below the coil is the capacitor pocket. The overlaid contour map shows the magnetization projected onto the transverse plane after a 90° pulse is applied. The signal strength immediately outside of the device is 50% and drops off rapidly with distance. Multi-echo sequences will progressively eliminate the signal from outside the sensor because the refocusing pulses are also ineffective.

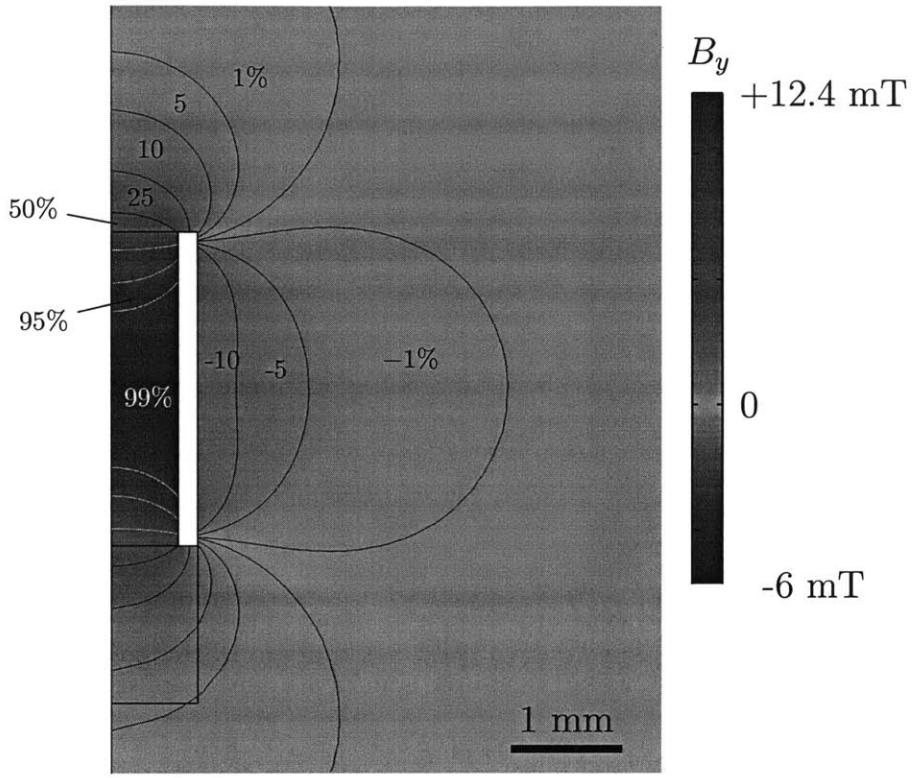


Figure 3-9: Field map of sensor coil showing high degree of uniformity in the sample chamber. The contour lines represent $M_{xy}/M_0$, the projection onto the transverse plane following a 90° pulse calibrated to the center of the chamber.

### 3.3.2 Wire diameter

Previous work suggested that the overall length of the coil determines the signal strength [57]. The basic argument is that there is a fixed current density in the copper wire. This is indeed the case for a fixed sample diameter. However, a sensor must fit through a biopsy needle and has a fixed outer diameter, and thinner wire

allows for a larger sample chamber. The chamber walls are three wire diameters smaller than the sensor diameter; wrapping the coil adds two wire diameters, and returning the wire to complete the circuit adds a third. A 2.2 mm diameter sensor with a 4 mm long chamber and a coil wound of 32 American Wire Gauge (AWG) wire will have a chamber volume of 6 $mm^3$. This volume can increase to 10 $mm^3$ if 40 AWG wire is used instead. Figure 3-10 shows the simulated signal-to-noise ratio from sensors with increasing wire diameter. The first case fixes the sample diameter, and the second case fixes the sensor diameter. Thinner wire is better even for a fixed sample size. The current flows along a thin layer on the inner face of the coil. Thinner wire packs more copper into that region, yielding a modest improvement.

### 3.3.3 Sensor diameter

The sensor was designed for implantation through an 11 gauge needle. Four sensors were fabricated with different diameters to explore the lower practical limit on sensor size. The capacitor pocket was not changed to investigate just the size of the chamber and coil (Figure 3-11). The sensors were tested in a 0.47 T homogeneous field magnet (Bruker mq-20). The uniform field ensures that the entire sample contributes to the signal rather than a slice through the center. The signal strength shown in Figure 3-12 is normalized to the 2.2 mm sensor on the single-sided magnet. The signal-to-noise ratio is approximately 10 times large for a sensor in a uniform field. A 1.6 mm sensor could be implanted through a 14 gauge needle. The thinner wire diameter becomes increasingly important for small diameter sensors. Simulations over a wider range of sensor coil diameters (Figure 3-13) shows a similar trend. The highlighted point corresponding to needle gauges below 11G. The largest possible sensor should be

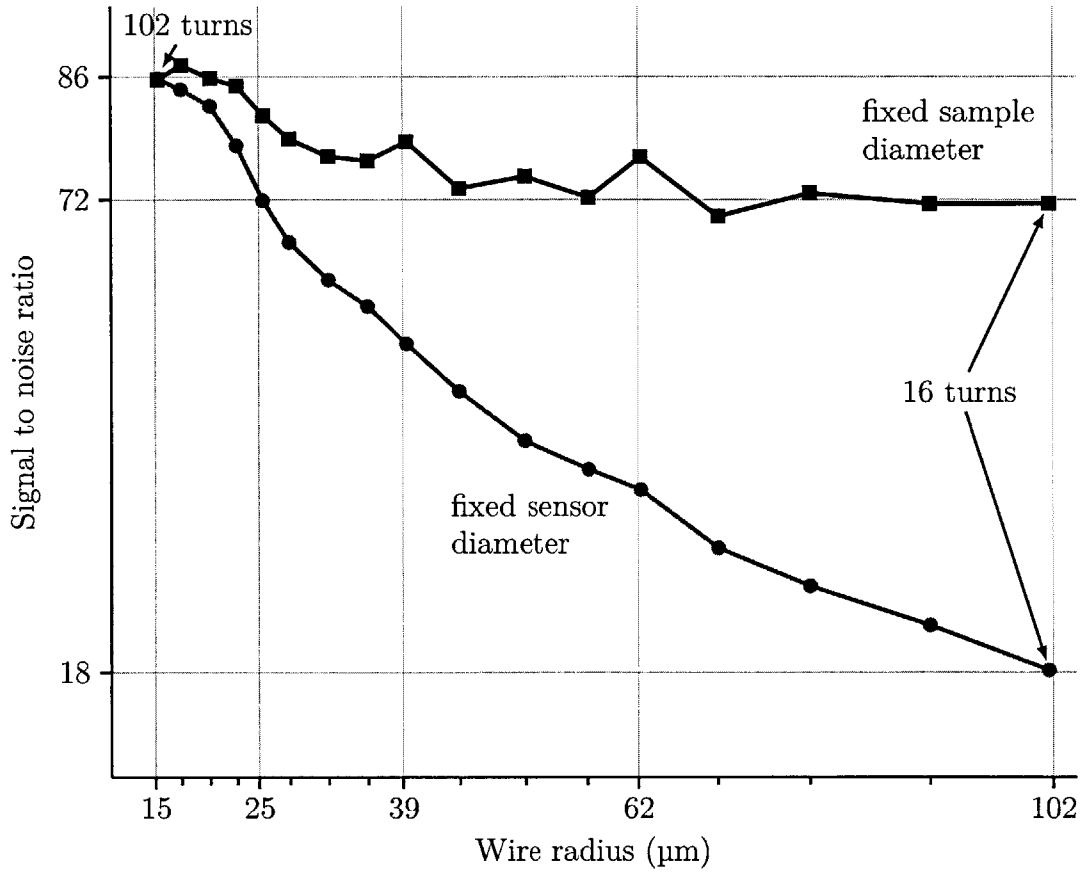


Figure 3-10: The signal-to-noise ratio as the wire diameter is increased. The smallest possible wire diameter will maximize the signal-to-noise by increasing the sample volume. The coil length is fixed and the wire is wound as compactly as possible; many more turns of the finer wire are needed to fill the length.

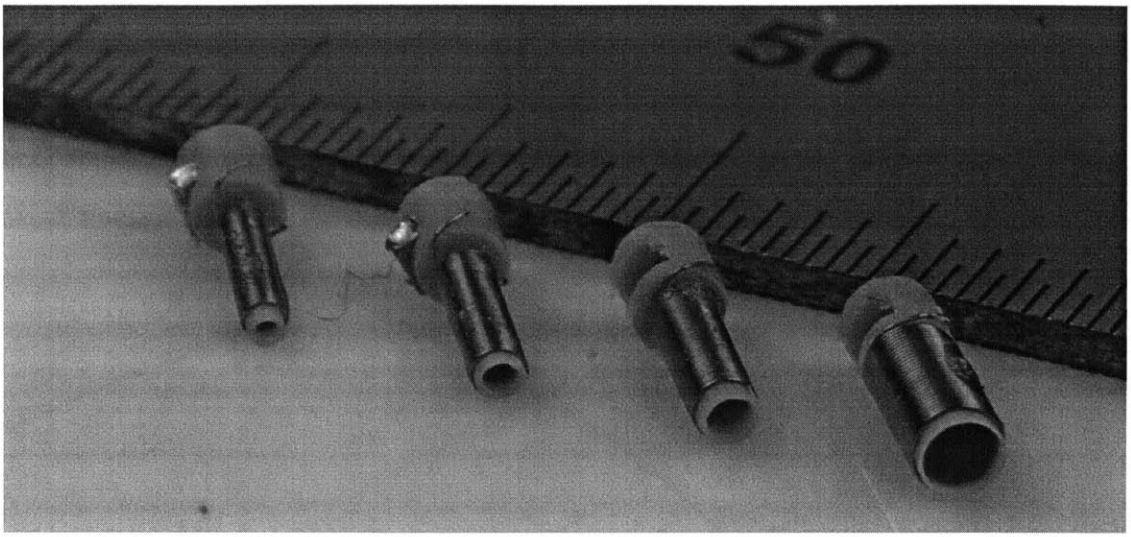

Figure 3-11: Photograph of sensors with smaller diameter coil and chamber to investigate the practical lower limit on sensor size.

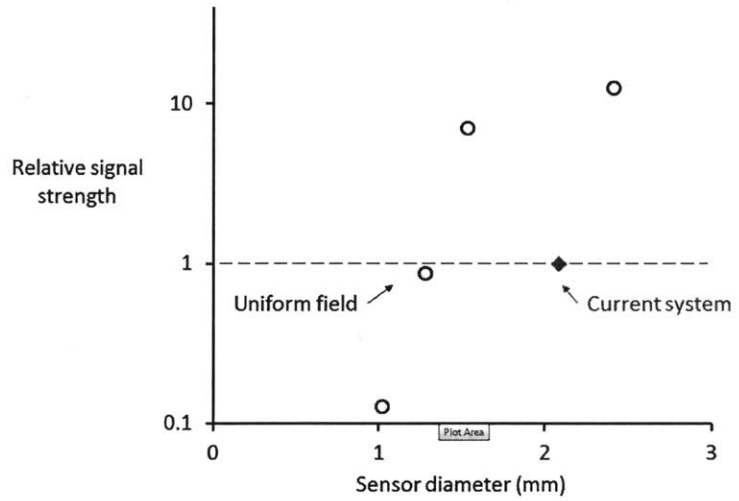


Figure 3-12: Signal strength versus sensor diameter normalized to the 2.2 mm sensor on the single-sided magnet. The largest sensor for a given application gives the strongest signal.

built for the application. The impact of wire diameter becomes even more critical for smaller sensors. Every effort should be made to maximize the sample volume.

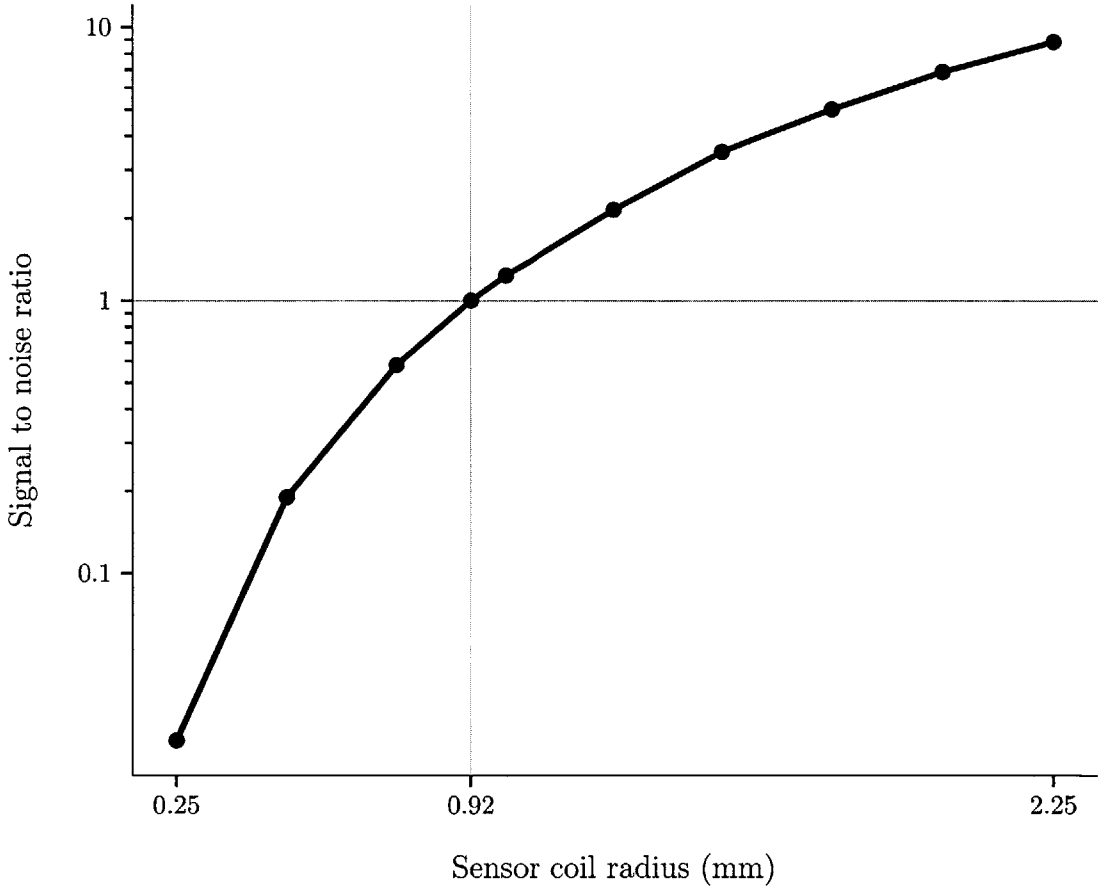


Figure 3-13: Simulated signal-to-noise ratio versus sensor diameter. Increasing the sensor volume increases the signal-to-noise ratio, but the gains are modest as the sensor becomes very large.

### 3.3.4 Reader coil diameter

The reader coil design is constrained by the tissue surrounding the device. A sensor implanted with a biopsy needle will be oriented along the direction of implantation. The reader coil should also be oriented with its axis along that direction. This may be perpendicular to the skin. The implantation in mice and rats, however, is along the axis of the body parallel to the skin's surface. The reader probe for rodents is designed so that the animal can fit through the coil. Mice can be restrained in a 26 mm diameter tube that allows for oxygen and anesthetic gas to be introduced. The reader coil is 28 mm in diameter to fit the restraining tube. The same probe is used to measure sensors implanted in the gastrocnemius (calf) muscle of a rat by inserting the leg into the reader coil. Practical considerations have fixed the inner diameter of the coil, but the number of turns and length are free variables to be explored.

### 3.3.5 Number of turns on the reader coil

Increasing the number of turns on the reader coil decreases the received NMR signal. Figure 3-14 shows the simulated signal strength from a sensor inside the reader as a function of number of turns on the reader coil. The sensor remains the same, thus any increase in the NMR signal will also apply to the noise from the sensor. The overall signal-to-noise ratio will therefore be determined by the noise originating in the reader coil.

A reader with more turns will have a greater resistance and inductance. The resistance increases approximately linearly with the number of turns, $N$, but the inductance increases by approximately $N^2$. The resulting higher coil quality factor,

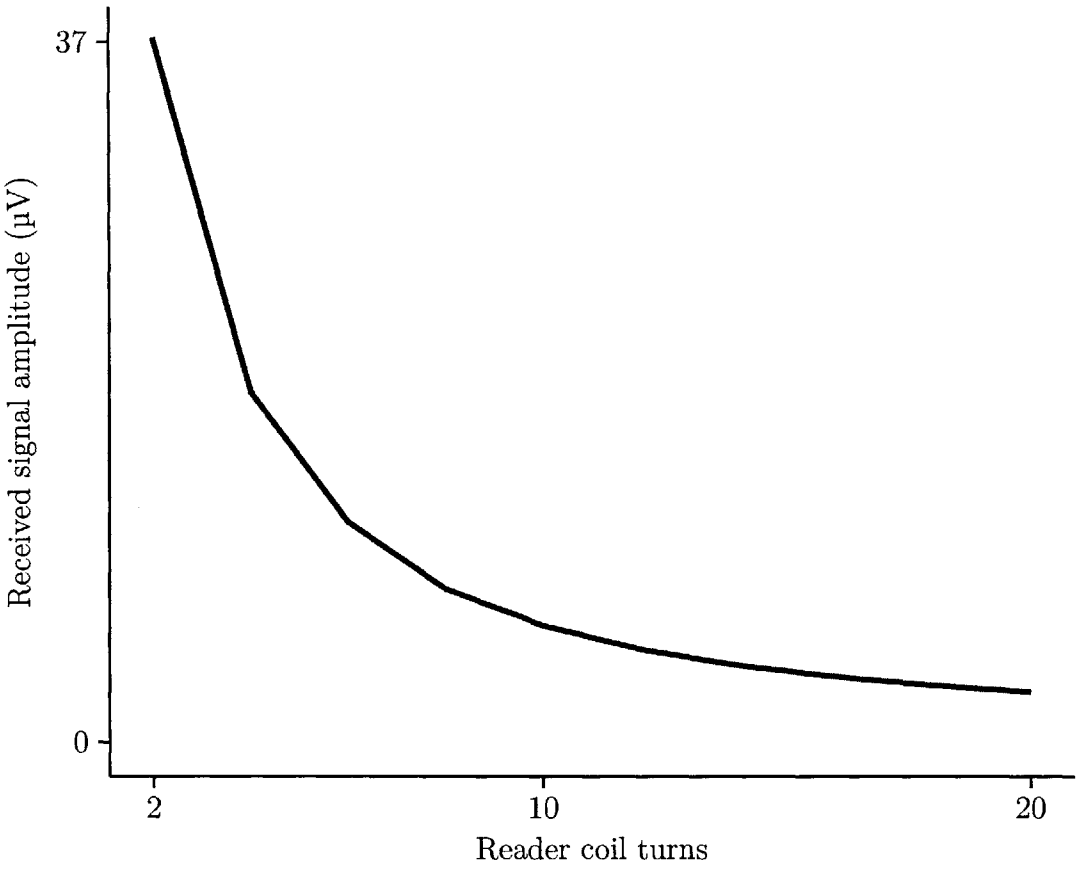


Figure 3-14: The received signal amplitude decreases as the number of turns on the reader coil is increased.

$Q = \omega L/R$, improves the filtering of the noise. Figure 3-15 shows that the reader noise dominates when the reader coil has fewer than 6 turns. The resultant signal-

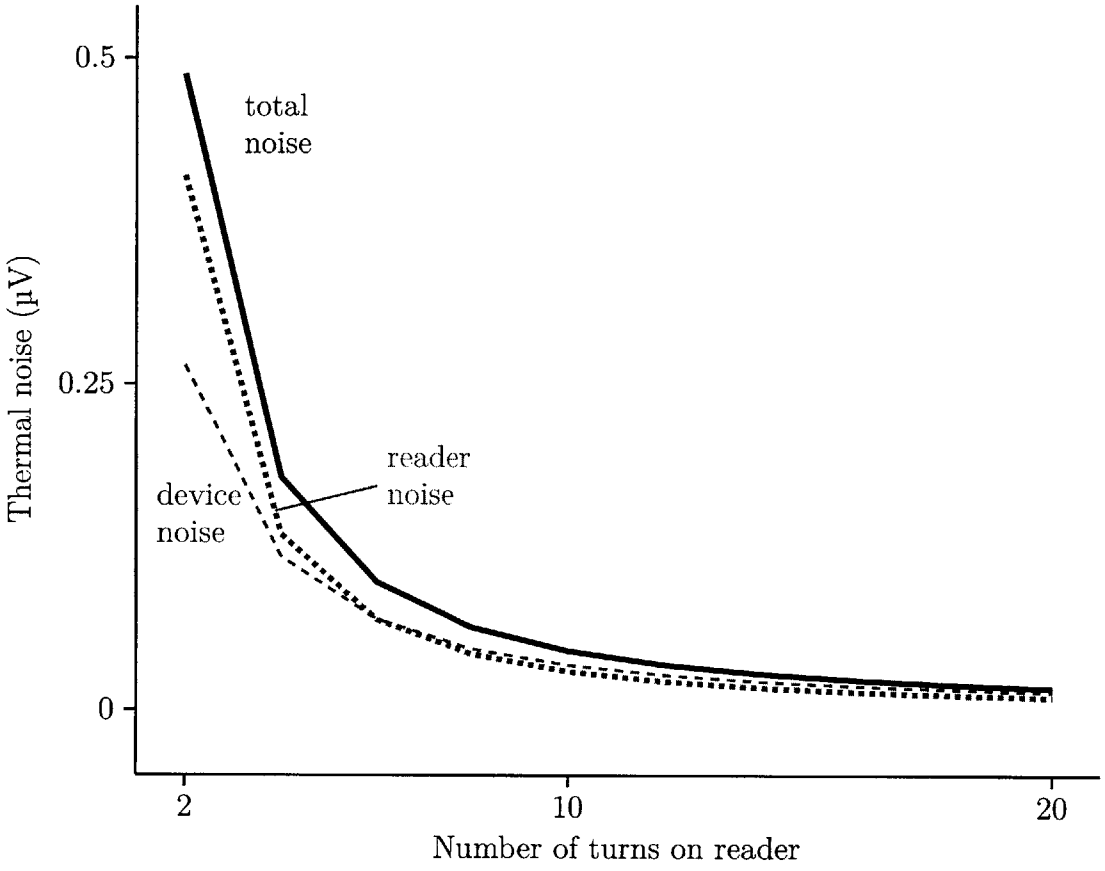


Figure 3-15: Thermal noise at the receiver due to losses in the reader and sensor coils. The thermal noise from the reader coil dominates the sensor coil noise when the reader coil has fewer than six turns. If thermal noise is the only noise source then the reader coil should be designed so that the sensor noise is dominant.

to-noise ratio is shown in Figure 3-16. Paradoxically, a higher sensor to receiver gain does not improve the overall signal fidelity.

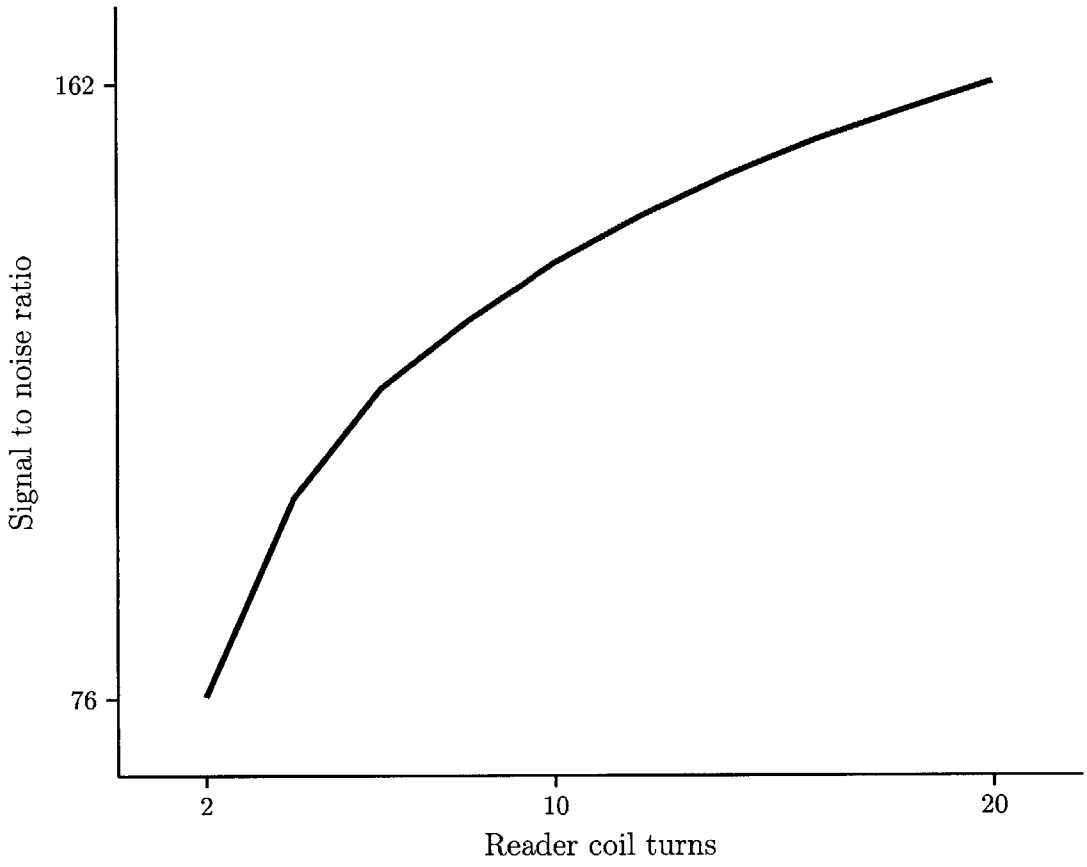


Figure 3-16: Considering only the thermal noise, the signal-to-noise ratio increases with the number of turns on the reader coil.

### 3.3.6 Noise and EMI

Figure 3-16 corroborates work on inductively coupled coils for NMR spectroscopy. The high-field magnets increase the signal, and the excellent shielding ensures that the sensor coil is the dominant source of noise [58]. The question is whether the same applies to a low-field NMR measurement through tissue.

The signal must be strong enough to be digitized efficiently. The analog to digital converter expects the incoming signal to span a certain voltage range. A 16 bit digitizer divides the anticipated signal span into 65,536 discrete levels. Each data point is rounded to its nearest level. If the actual signal is weaker and spans only a fraction of the range, the rounding becomes significant and is referred to as quantization error [59]. The signal must be strong enough to be detected, regardless of the signal-to-noise ratio.

The preamplifier adds a constant voltage noise plus current noise that is proportional to the probe impedance. There is an optimal probe impedance that minimizes the preamplifier noise [32]. Ideally, the spectrometer is designed with the receiver path optimized for noise and the transmit path optimized for maximum power transfer [60]. Most spectrometers are made of discrete components that are all designed with $50\,\Omega$ impedance. The spectrometer (KEA, Magritek, Wellington, New Zealand) was connected to a $50\,\Omega$ resistor recorded a noise level of $0.3\,\mu V$. Figure 3-15 suggests that the reader coil noise would dominate on a two-turn coil but that the amplifier noise might dominate otherwise.

The final consideration is electromagnetic interference (EMI). The sensor will be implanted in living tissue that has a conductivity $\sim 1\,S\,m^{-1}$. The conductive tissue acts as an antenna picking up noise from the environment. Shielding will eliminate EMI,

but shielding a patient is impractical and would defeat the purpose of a portable system. The noise level was measured with a mouse inside the reader coil. The recorded level varies from 0.8 µV to 1.5 µV, which is greater than the thermal noise.

The signal-to-noise ratio is fundamentally limited by thermal noise, but additional noise sources dominate when measuring in living tissue. The best signal-to-noise ratio is achieved by maximizing the voltage gain between the sensor and the receiver.

### 3.3.7 Reader coil length

Figure 3-17 shows a contour map of mutual inductance versus position with the sensor parallel to reader axis. The reader is a two-turn loop centered at the origin. The bold contour lines outline a region where the mutual inductance is within ±1% of the value at the origin. The diagram is rotationally symmetric about the $\hat{x}$ axis. Inserting a space between the two turns increases the overall reader length and reduces the maximum mutual inductance. However, the uniform region over which the sensor can be moved without requiring retuning becomes larger. The sensor can be measured anywhere in this region even if the precise location is unknown. A coil with one radius separation between the two turns is known as a Helmholtz coil. The expanded ±1% region is shown in Figure 3-18.

### 3.3.8 Tissue conductivity

The simulations so far have assumed that the sensors are in free space, not in conductive tissue. This assumption is certainly valid for benchtop tests, but the sensor will be implanted into living tissue that has an electrical conductivity between $0.2\,\mathrm{S\,m^{-1}}$

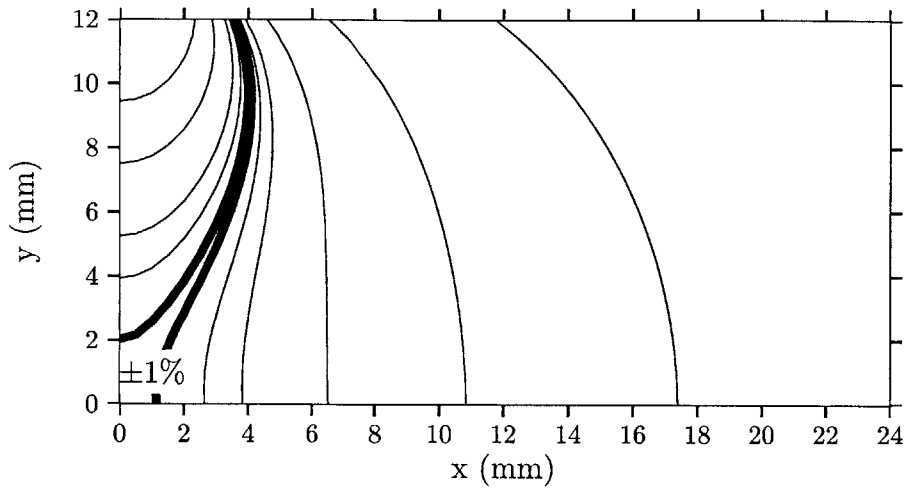


Figure 3-17: Mutual inductance between a two-turn reader coil and a sensor coil versus position. The diagram is rotationally symmetric about the $\hat{x}$ direction. The thick line represents the volume over which $M$ changes less than 1% from the origin.

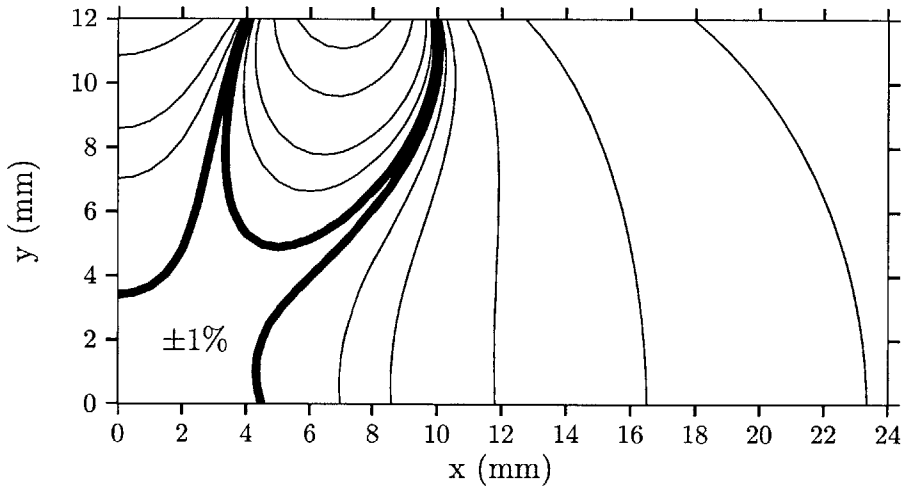


Figure 3-18: Mutual inductance contour map when the two turns of the reader coil are separated by one radius. The 1% region is significantly expanded compared to Figure 3-17.

and $0.7\,\mathrm{S\,m^{-1}}$ [61]. The conductivity is responsible for pickup of noise from the environment as discused in Section 3.3.6, but there is inherent loss in the tissue.

The oscillating field generated by the reader coil induces a current in the conductive fluid inside the body. This current generates a field that opposes the reader's field. The moving charges experience a resistance that will also be a source of thermal noise. The advantage of the implanted probe is that only a weak field is needed to generate a high field inside the sensor (see Figure 3-1).

Figure 3-19 shows the field inside the sensor and the reader coil's effective resistance as a function of conductivity at 20 MHz. The field does not experience a significant drop off until the conductivity is well above that of normal tissue.

A higher Larmor frequency is almost always preferred in NMR. Both the magnetization (Equation (2.1)) and the induced voltage (Equation (2.4)) are proportional to $\omega_0$. Field strengths of 2 T to 3 T are available from permanent magnet systems but only for small sample sizes. The loss at high frequency is more pronounced and would be noticeable even in moderately conductive samples. Figure 3-20 shows that a lower frequency probe performs better for very high conductivity samples.

## 3.4 Practical considerations

Section 3.2.1 showed that the two variable capacitors on the reader probe can match virtually any coil configuration to the source impedance. Correctly tuning the probe becomes tricky when the sensor is hidden inside tissue.

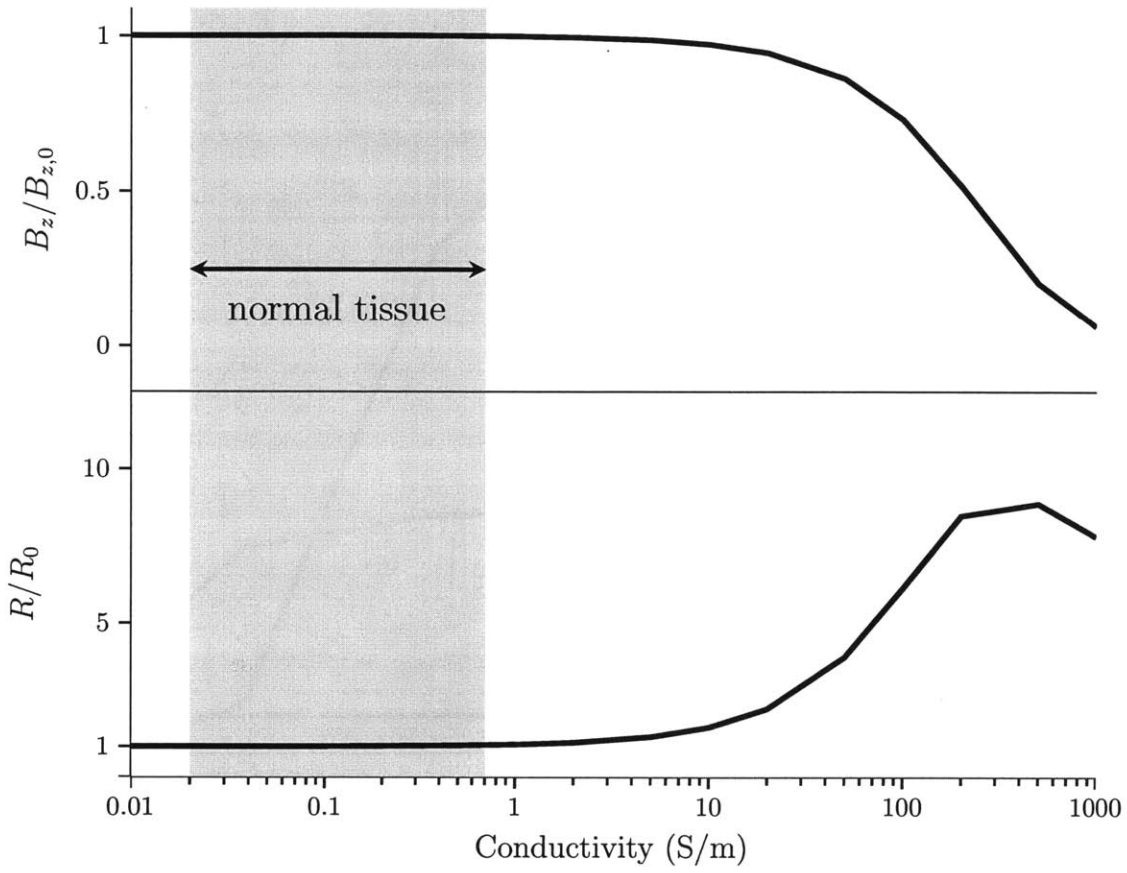


Figure 3-19: The field strength inside the sensor is virtually unchanged over the range of conductivity expected inside the body. The increased resistance of the reader coil captures the loss in the conductive medium.

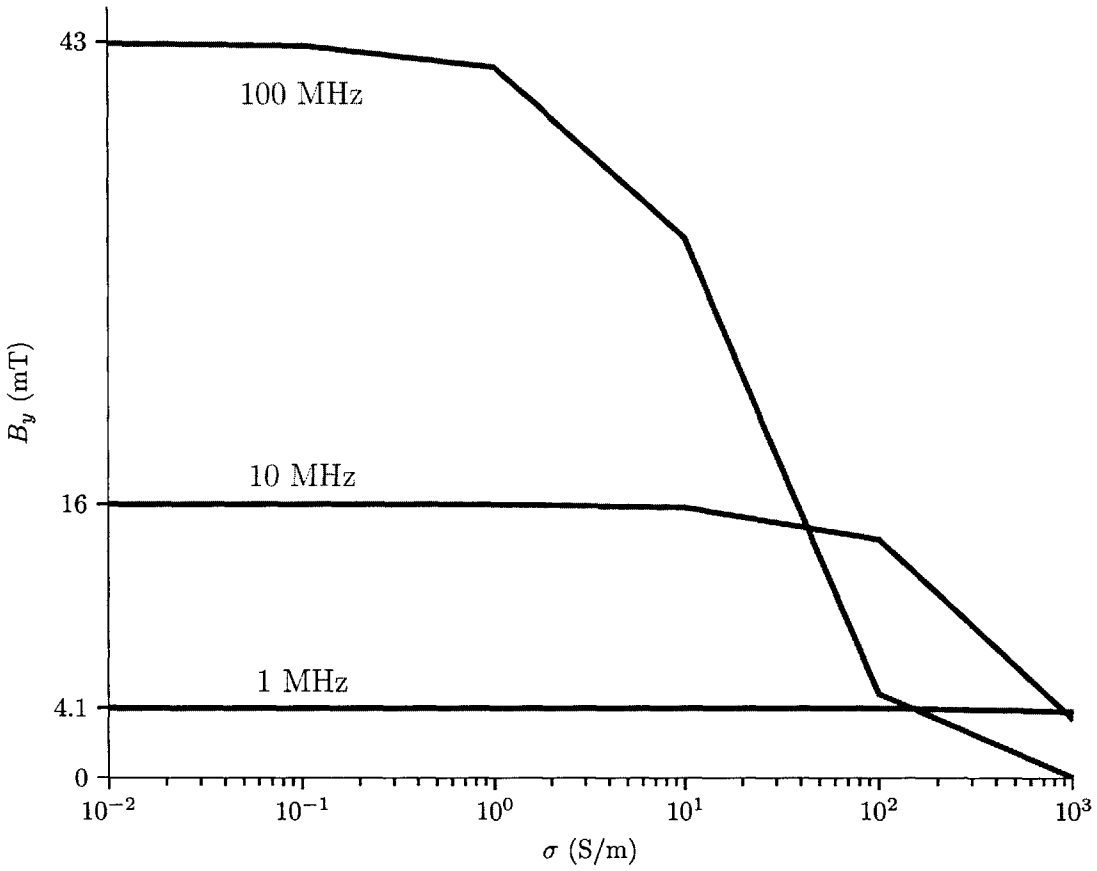


Figure 3-20: Plot of sensor field versus the conductivity of the surrounding medium. Higher frequency operation is generally preferred except in very high conductivity media.

### 3.4.1 Tuning frequency

If the sensor resonant frequency, $\omega_S$, does not equal the Larmor frequency, $\omega_0$, the reader can still be tuned and matched to $50\,\Omega$. Figure 3-21 shows how the signal-to-noise ratio varies over a $\pm 20\%$ mismatch between the sensor frequency and the Larmor frequency. Small variations in frequency have very little effect on the signal-to-noise-ratio.

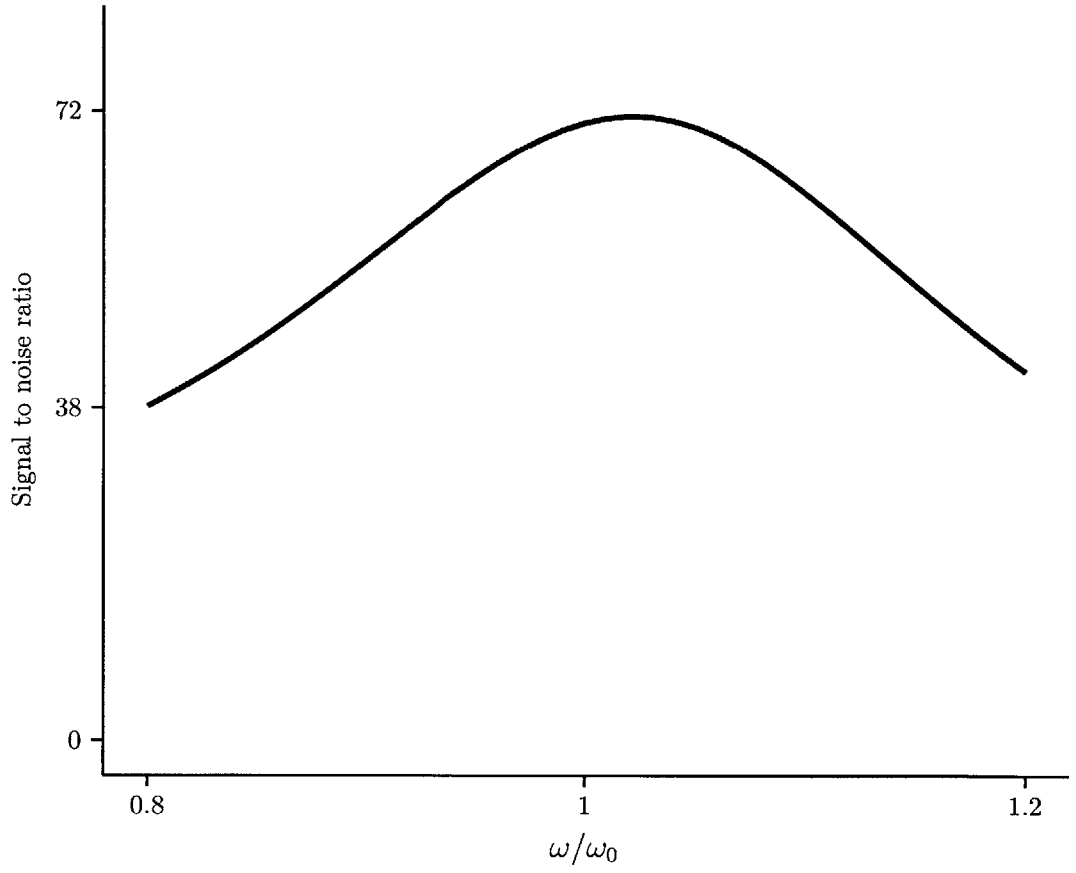


Figure 3-21: Plot of signal-to-noise ratio as a function of mismatch between the sensor resonant frequency and the Larmor frequency. Maximum SNR is achieved on resonance, but slight deviations in the sensor's resonant frequency do not matter.

The main challenge with tuning is that it is possible to tune when the sensor is not in the optimal position. The tuning will give the local maximum SNR, but not the global maximum. It would be helpful to be able to tune the reader without a sensor present to ensure that when the sensor is in the right place the optimal signal-to-noise ratio will be achieved. Figure 3-22 shows a scheme whereby the reader is tuned to a lower frequency without the sensor present. The sensor is then positioned at the center of the reader coil, and the signal-to-noise ratio is simulated. The precise frequency offset will depend on the coils, but for this configuration the maximum possible SNR is achieved if the reader is tuned such that $Z(\omega = 0.9\omega_0) = 50\Omega$ without the sensor present. The reader is then moved closer to the sensor until the highest signal-to-noise ratio is recorded. That is the global maximum, and it is already tuned optimally.

### 3.4.2 Misalignment

The reader coil is designed to reduce the effect of lateral misalignment on the mutual inductance and on the tuning. It is much harder to compensate for angular misalignment, however. The mutual inductance can be reduced to zero if the sensor is at a 90° angle to the reader coil.

A sensor was rotated about $\hat{z}$ in a uniform field to investigate the extent of reduction in mutual inductance as a result of angular misalignment. Figure 3-23 shows that the signal amplitude is reduced by approximately 50% when the sensor is rotated by 45°, and a signal is still measurable with a 60° deviation.

If the sensor is rotated to have a component of its axis along the magnetic field direction, $\hat{z}$, then the effective oscillating field is also reduced to $B_{1,eff} = B_1 \cos\theta$.

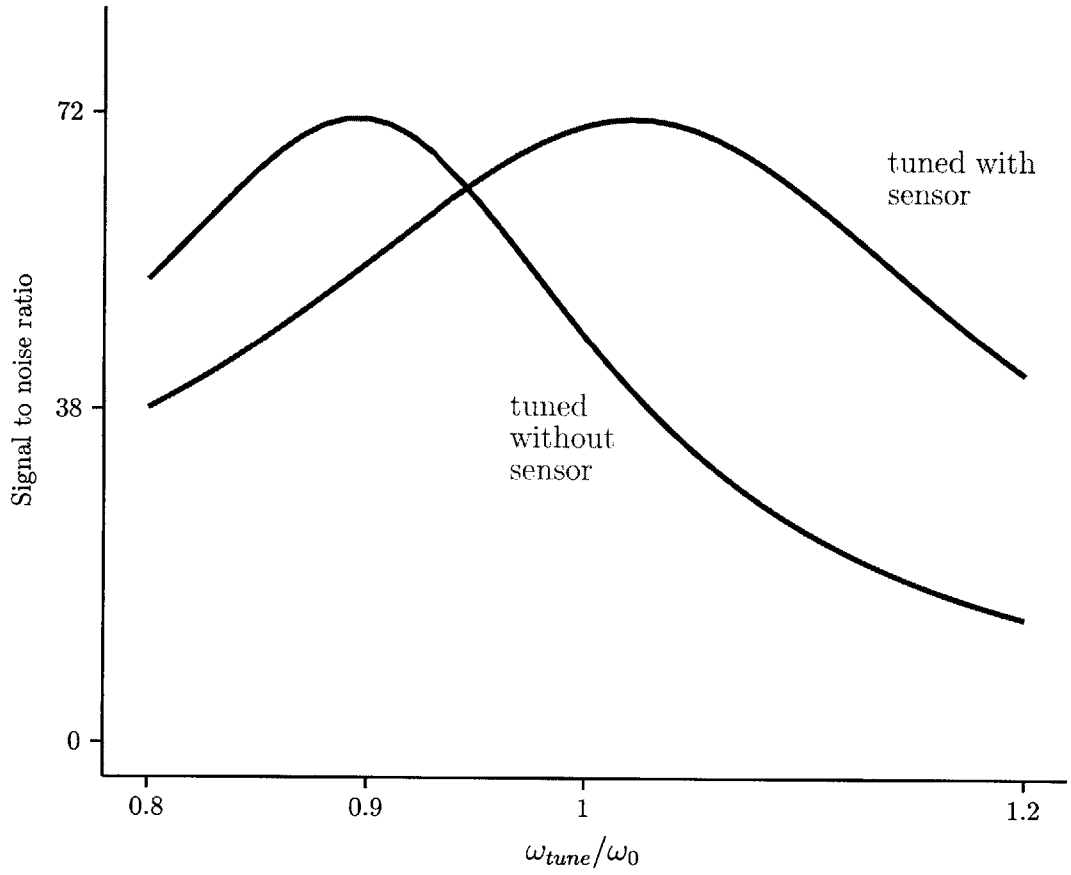


Figure 3-22: The reader coil can be tuned to a lower frequency without the sensor to maximize the signal-to-noise ratio when the sensor is inserted. The SNR is equivalent to tuning at the resonant frequency with the sensor inside. This method provides a way to tune when the precise location of the sensor is unknown.

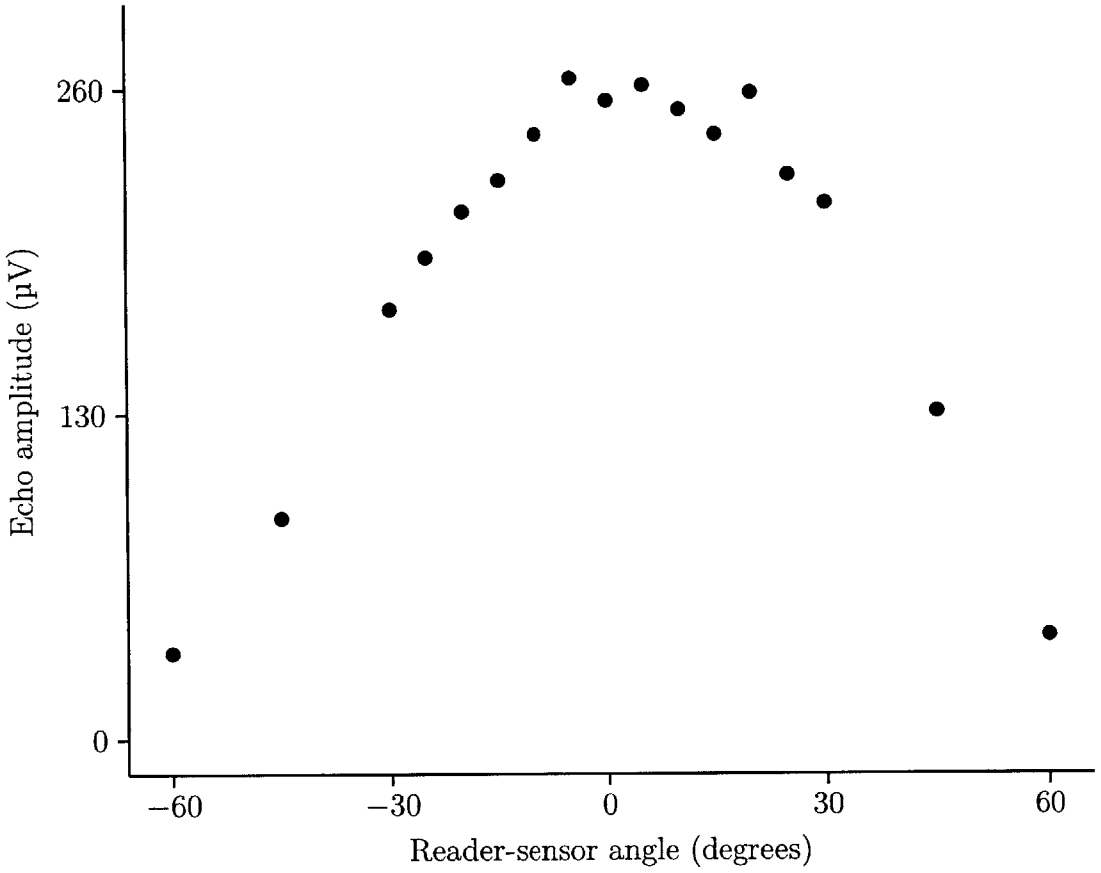


Figure 3-23: Measured echo amplitude versus the angle between the reader and sensor axes. The signal is relatively insensitive to angular deviations less than 20° and is detectable even with deviations as large as 60°.

### 3.4.3 Remote measurement

A sensor implanted in a human cannot be measured inside a reader coil, but, instead, the reader coil is pressed up against the skin. This arrangement corresponds to values of displacement $x > 4$mm on the mutual inductance contour map in Figure 3-17. The Helmholtz configuration may not be the optimal coil for a remote measurements.

The field strength at a distance $x$ from a current loop of radius $r$ can be calculated using the Biot-Savart equation. The field along $\hat{x}$ is

$$\vec{B}(r,x) = \frac{\mu_0 I}{2} \frac{r}{(r^2+x^2)^{3/2}} \hat{x}. \tag{3.26}$$

If the implantation depth is known then $x$ is fixed. The optimum coil radius can be calculated by maximizing $B_x(r,x)$ with respect to $r$. Differentiating and solving for $r$ in terms of $x$, the optimum reader diameter for a fixed depth of measurement is $x/\sqrt{2}$. Figure 3-24 shows the field strength inside the sensor as a function of separation for two different reader coils. A 14 mm radius reader coil is the optimum coil for measuring at approximately 10 mm depth. A portable system for measuring sensors in humans could have a set of concentric coils. The appropriate coil could be chosen based on the implantation distance. Figure 3-24 also hints at a method for measuring the implantation depth. If the two coils are connected such that the fields are in opposite direction, then the fields will cancel where their two curves cross. The mutual inductance to a sensor would be zero at that distance and non-zero everywhere else. The known depth can then be used to pick the appropriate reader to perform the measurement.

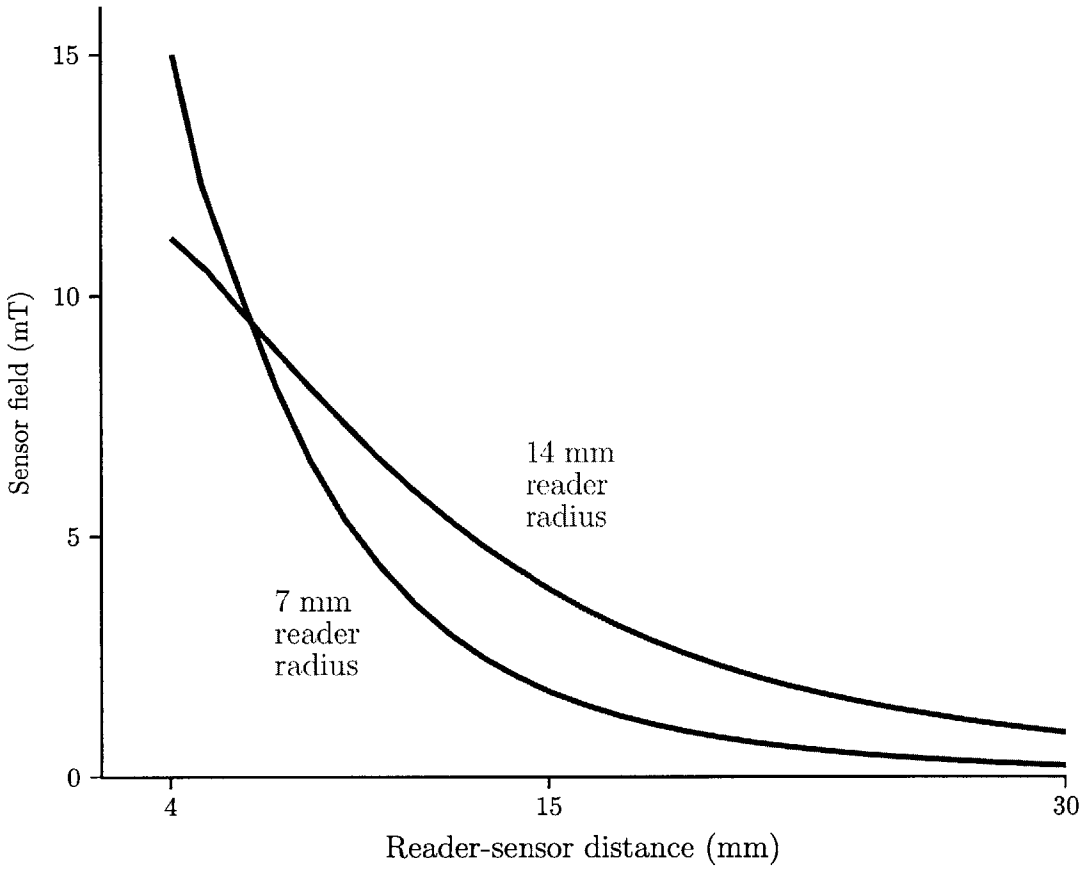


Figure 3-24: Field strength inside the sensor at a distance from the reader coil mimics the human system configuration. A larger radius coil improves the sensitivity at larger distances. There is an optimum coil radius for each measurement depth.

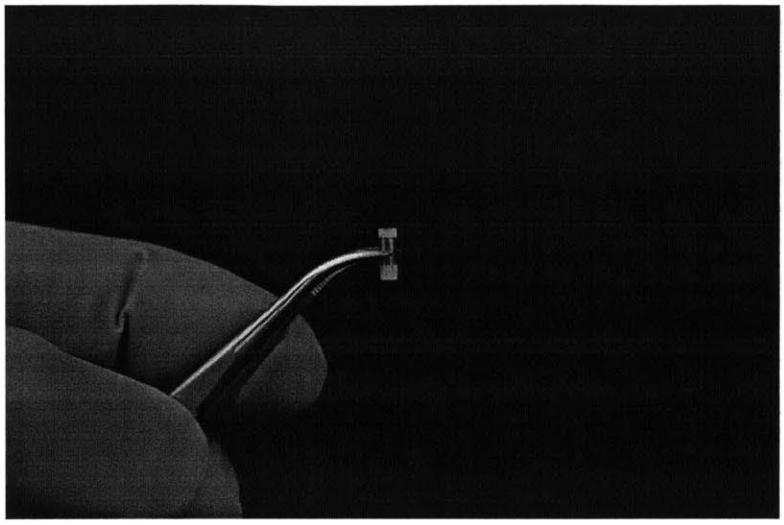

Figure 3-25: Photograph of an implantable sensor

## 3.5 Sensor fabrication

The sensor is designed to be implanted through a biopsy needle. It must retain sensitivity during its stay in the body and provide useful information that will inform a clinician's medical decisions. It should not cause an adverse reaction in the surrounding tissue both for the patient's well-being and to avoid measuring its own impact on the tissue.

Biopsy needles are available in a variety of sizes; smaller aspirator needles are less invasive, while larger core biopsy needles yield a larger sample and better results. The sensor is designed to fit a standard 11 Gauge needle that has an inner diameter of 2.3 mm. One example of a soft tissue core biopsy needle is the Quick-Core® Biopsy Needle Set (Cook Medical, QCS-14-9.0-20T) that consists of a needle, a guide cannula, and a trocar. A photograph of the three parts is shown in figure 3-26.

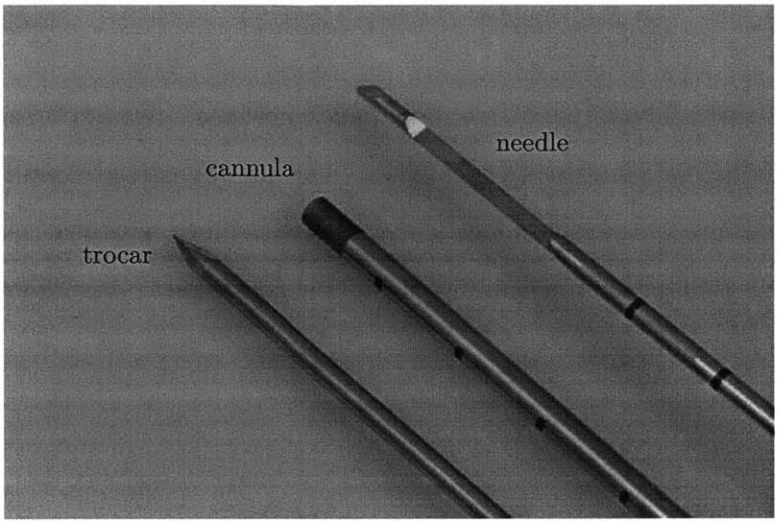


Figure 3-26: Core biopsy needle. A trocar facilitates insertion into the body. The cannula provides a channel through which the biopsy needle can obtain multiple tissue samples.

The implantation of a sensor into a gelatin phantom is shown in a photo collage in figure 3-27. The cannula and trocar are assembled together forming an introducer needle. The physician inserts the needle under image guidance into the region to be tested. The trocar is removed and the biopsy needle can be inserted through the cannula to take many samples. This particular model can excise a 20 mm long tissue sample from up to 9 cm deep into the body. The sensor would be implanted after the samples are removed.

A more practical tool for testing the sensors is a microchip injector designed for implanting radiofrequency identification (RFID) tags in pets and livestock. The injector is normally supplied sterile and preloaded with an RFID tag. Subcutaneous implantation is fast and painless, and anesthesia is not necessary. The parts of the injector are shown in figure 3-28. A syringe plunger with an extended arm deploys the sensor through the needle, while the barrel provides support. The inner diameter

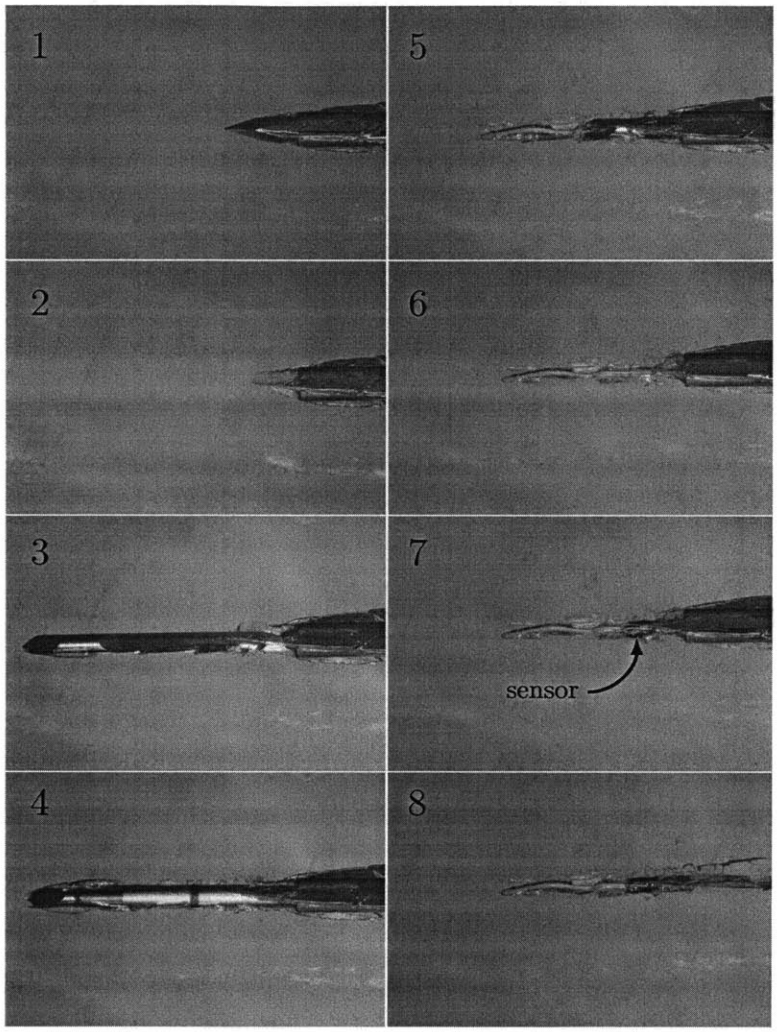


Figure 3-27: Sensor implantation following a mock biopsy procedure on a gelatin phantom.

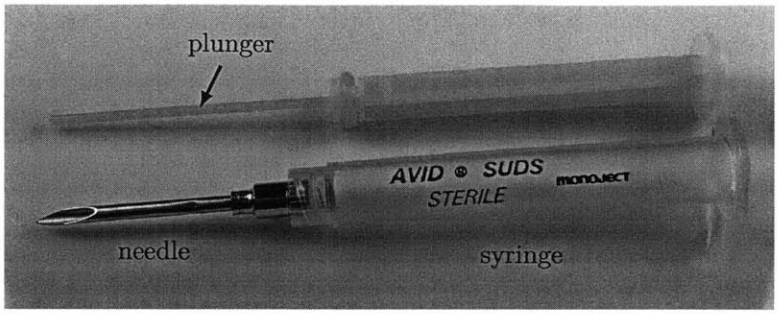


Figure 3-28: Subcutaneous implantation needle.

of this injector is 2.23 mm.

A 2.2 mm diameter sensor easily fits through either the biopsy needle or the chip injector. The main components of the sensor are shown in figure 3-29. A plastic body provides mechanical support to the NMR probe, which is comprised of a coil and a capacitor. The sample chamber holds the contrast agent, which determines what the sensor can detect. The manufacturing steps are described in the following sections.

### 3.5.1 Machining the plastic body

The body of the probe is machined out of a solid block of polyetheretherketone (PEEK), a high temperature thermoplastic that is used extensively in orthopedic medical devices [62, 63]. PEEK has a high enough melting point that the capacitor and coil can be soldered in place. Direct soldering avoids transfering the fragile circuit onto the body and increases the yield.

The plastic body is machined using a precision milling center (Model S, Cameron Micro Drill Presses, Sonora, CA). The mill has a high-speed spindle (E3000C, Nakan-

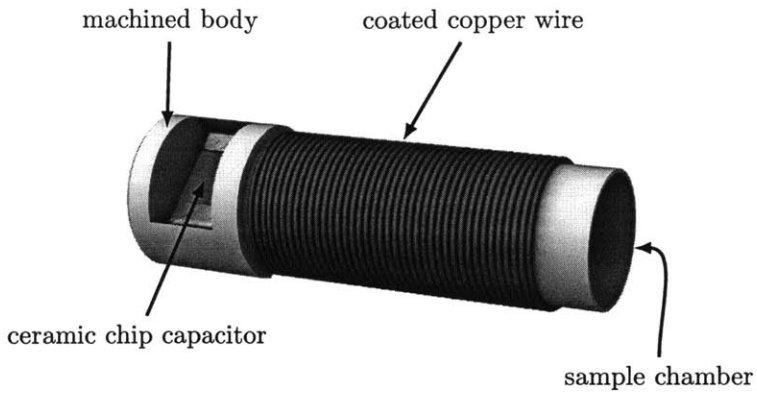


Figure 3-29: Key components of implantable sensor

ishi Inc. Kanuma-shi, Tochigi, Japan) that can handle small carbide cutting tools (Harvey Tool, Rowley, MA). Forty sensors are milled from a single PEEK block measuring 65 mm long, 40 mm wide, and 20 mm thick. Figure 3-30 shows the first milling steps. The chamber and coil bobbin are cut as an upright hollow cylinder with a wall thickness of 50 µm. A small pedestal is milled beneath that will house the capacitor. The stock is mounted vertically so that the cylinders are on their side. The capacitor pocket is milled into the pedestal as shown in figure 3-31. Two holes are drilled to feed through the coil wires. Two relief holes are drilled at the end to allow air to escape during potting. The completed body is parted from the stock and is ready for coil winding. It takes approximately one minute of cutting time per base.

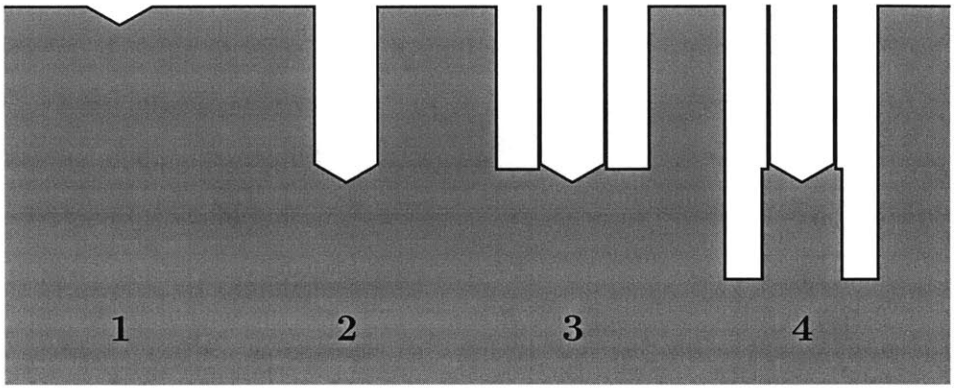


**SIDE VIEW**

Figure 3-30: Machining the sensor body and cavity. The cavity is drilled (1-2) and the coil support bobbin are milled using carbide end mills (3). The lower portion will house the capacitor and is cut to the final sensor diameter (4).

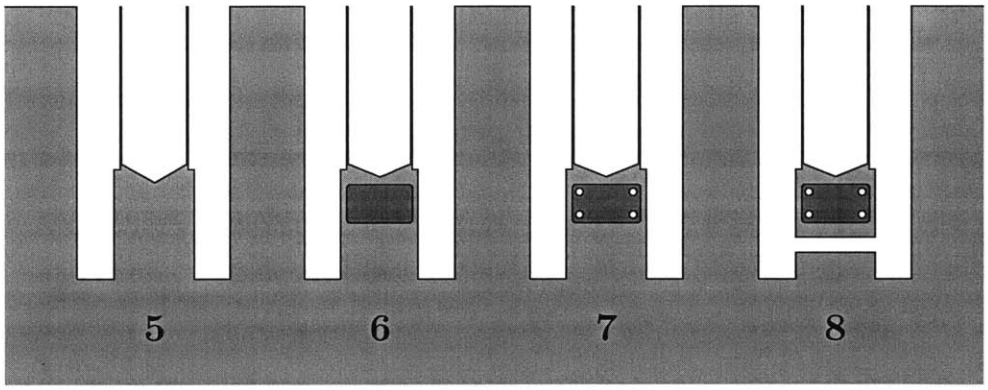


**TOP VIEW**

Figure 3-31: Machining the capacitor pocket. The stock is rotated 90°, and a pocket is cut for the tuning capacitor (5-6). Wire through-holes are drilled (7) before the completed body is parted from the stock (8).

### 3.5.2 Winding the coil

The body is supported on a steel rod and mounted on a coil winding machine (Optima 1100, Synthesis Winding Technologies Pvt. Ltd., Bangalore, India). The wire is fed into the capacitor pocket and secured. The winder rotates the bobbin while maintaining constant tension in the wire.

The sensors used in vivo had 42 turns of 40 AWG coated copper wire (MWS Wire Industries, Westlake Village, CA). The wire has a 79 µm diameter copper core with a 3 µm thick polyurethane-nylon coating. Coils are wound with each successive winding in contact with the previous one to give a wire spacing of 92 µm. The coil is secured either with a heat gun or a small dot of medical grade cyanoacrylate gel. The wire is cut from the machine and fed through the opposite wire hole. The body with the new coil is removed for testing.

### 3.5.3 Tuning the resonant circuit

Many sensors are required for animal studies, so it is important that they are produced identically. Precision machining and controlled coil winding are a necessary first step. Proper tuning will ensure that all sensors have the same resonant frequency.

The coil inductance, $L_S$, is measured on an LCR meter (SR720, Stanford Research Systems, Sunnyvale, CA) with the aid of surface mount device tweezers. The inductance is typically 1.2 µH with approximately one percent deviation from the mean. A suitable capacitor must be chosen to tune each coil.

Surface mount capacitors are the obvious choice for a compact probe. Capacitors

with the metric designation 1608 measure 0.8 mm by 0.8 mm by 1.6 mm and can fit perpendicularly to the axis of the sensor. They are supplied in a dispensing roll with a nominal capacitance tolerance of 10 %. Each capacitor is measured with the LCR tweezers. The NMR probe is tuned by choosing a capacitor, $C_S = 1/(\omega_0^2 L_S)$.

The capacitor is loaded into the sensor pocket with the coil wires close to the capacitor connections. A small amount of solder paste (Quickchip) is applied on either side and soldered using a temperature controlled soldering iron (Weller W150). The protruding wires are trimmed leaving a fully functional NMR probe.

The final product will be completely encapsulated in epoxy, but it is helpful to confirm that the soldering and tuning were successful. A 20 mm diameter, 10 turn coil attached to a network analyzer (Hewlett-Packard 4396A) measures the frequency response of the sensor.

### 3.5.4 Potting in epoxy

The sensor is a fully functional NMR probe after the capacitor is soldered. The sensor can be tested on the benchtop. Potting in epoxy provides mechanical stability and insulates the probe from conductive tissue. All sensors are potted in medical grade two-part epoxy (Loctite M31-CL, Henkel Corporation). Epoxies are chemically inert once cured and are used to seal electronics in implantable medical devices[64]. This particular epoxy has a low viscosity and a 30 min work time that make it ideal for injecting into a mold around the sensor. It can be sterilized using either steam autoclave or ethylene oxide[65]. It is certified against biological tests (ISO 10993) that showed no adverse tissue effects after two weeks implantation [66].

The sensors are potted in a two-part acetal mold. The bottom part has four posts

to align the sensors and prevent any epoxy from filling the sample chambers. The top part has four 2.2 mm holes that will mold the outer surface of the sensor. The two parts are sealed together and the epoxy is injected through a filling port. The relief holes inside the capacitor pocket allow any air to escape. The epoxy cures overnight at room temperature. The mold is separated, and a gentle tap releases the sensors from the mold. A photograph of the NMR probe is shown in figure 3-32. The resonant frequency and quality factor of the potted sensors are measured using the network analyzer. The sensors are washed in a soap solution in a sonicating bath for 15 min. They are rinsed first in deionized water and then in isopropanol.

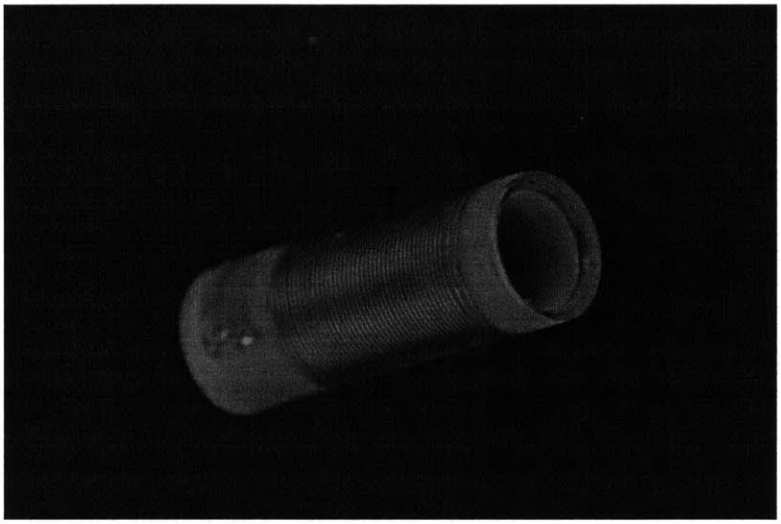

Figure 3-32: Photograph of a completed NMR probe. A sensor is made by filling the chamber with the appropriate chemically sensitive contrast agent.

Precision machining and choosing the right capacitor for each inductor yields a very tight frequency distribution. Twelve sensors fabricated this way had a mean center frequency of 15.35 MHz with a standard deviation of 18 kHz (or 0.1%). The average sensor quality factor was 41, meaning that the devices have a bandwidth of $f_S/Q_S =$ 380 kHz. Compared to the probe bandwidth, the sensors are identical.

### 3.5.5 Filling with the assay material

The contrast agents for pH and oxygen are solids. The sensor chamber can be filled with the monomers, and polymerization occurs directly inside the chamber. The plastic shows no cross-reactivity and does not inhibit the reaction.

Liquid based contrast agents, on the other hand, require a membrane to keep them inside the sensor. The membrane must allow the target to diffuse freely. The cardiac sensors (Chapter 6) were disc shaped devices with ample area to adhere a semipermeable membrane. The biopsy implantable sensors would require a minor modification to the chamber opening to allow a membrane-sealing ring to mechanically seal a membrane. Polyethylene membranes with nanometre sized pores are sufficiently compliant for snap-fit fixtures and have been used successfully to retain the nanoparticle contrast agents.

## 3.6 Reader fabrication

The majority of tests were performed on rodents and a specialized reader was designed to accommodate anesthesia and restraint. The reader coil has two identical coaxial coils separated by a distance of one radius. The current direction is the same in both coils to ensure that the fields add constructively in the center. The bobbin is machined out of acetal copolymer with a diameter of 28 mm. Two turns of 0.2 mm coated copper wire are wound on each side to form the coil. A tuning circuit is formed of two variable capacitors (Model 5641, Johanson Manufacturing Corporation, Boonton, NJ) potted in epoxy. The tuner and coil are both mounted onto a circuit board. The entire structure slides into a machined metal enclosure

that shields and grounds the coil.

## 3.7 Testing the complete system

The complete measurement apparatus for in vivo studies is built on a mobile cart as shown in figure 3-33. The anesthesia cart supplies oxygen with 1%-2% isofluorane gas. The magnet is mounted on a vertical lift with a temperature controlled stage. The lift adjusts the magnet independently of the reader coil to locate the sensor within the animal.

The computer and spectrometer (KEA 2, Magritek, Wellington, New Zealand) are on the middle shelf. Power supplies, the temperature controller, and water pump are on the lower shelf. The cart, keyboard and (computer) mouse are fully washable and sterilizable to prevent cross-contamination between animals.

The CPMG experiment outlined in section 2.1.2 can be used to confirm that the reader-sensor are working correctly. The first pulse in the sequence is increased in amplitude and the signal amplitude is recorded. The pulse amplitude is attenuated from a 100 W amplifier. The echo peak is highest when the 90° condition is met. Figure 3-34 shows the echo amplitude as a function of pulse amplitude. The maximum echo corresponds to the complete mapping of the magnetization onto the transverse plane. Doubling the pulse duration reduces the pulse amplitude required for a 90° pulse by 6 dB. A transverse relaxation measurement performed in vivo is shown in figure 3-35. The data are fit to a form $S(t) = S_0 e^{-t/T_2}$ to calculate the relaxation time.

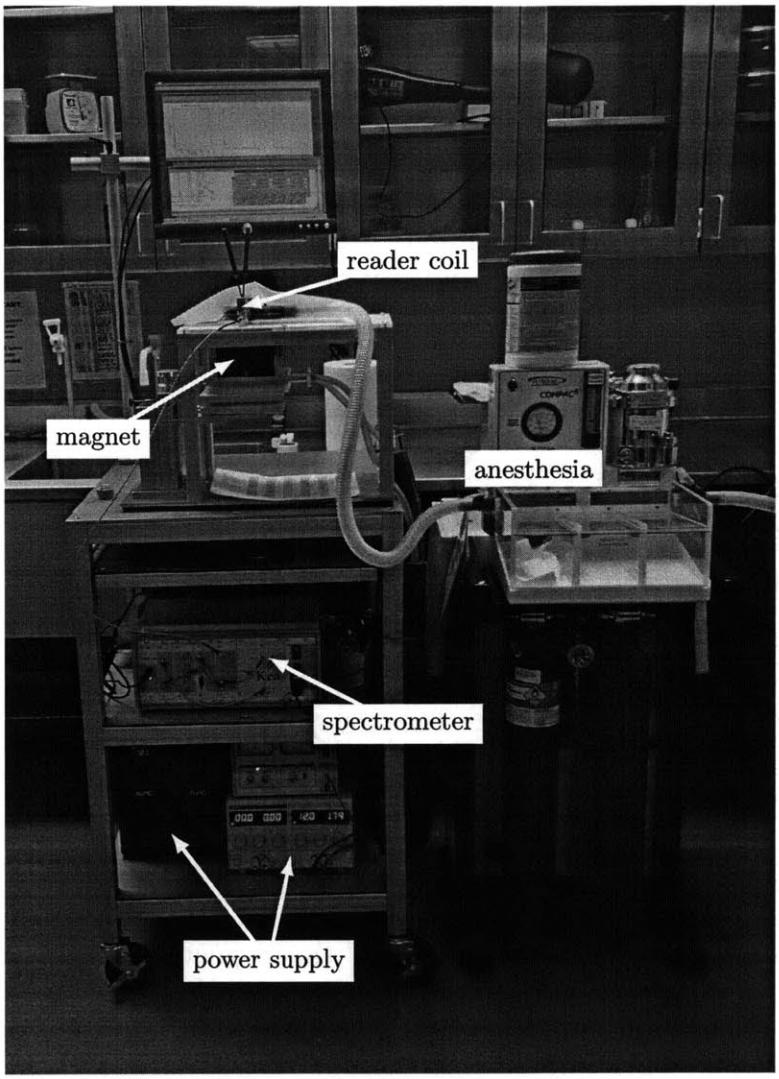


Figure 3-33: Complete measurement apparatus for preclinical testing.

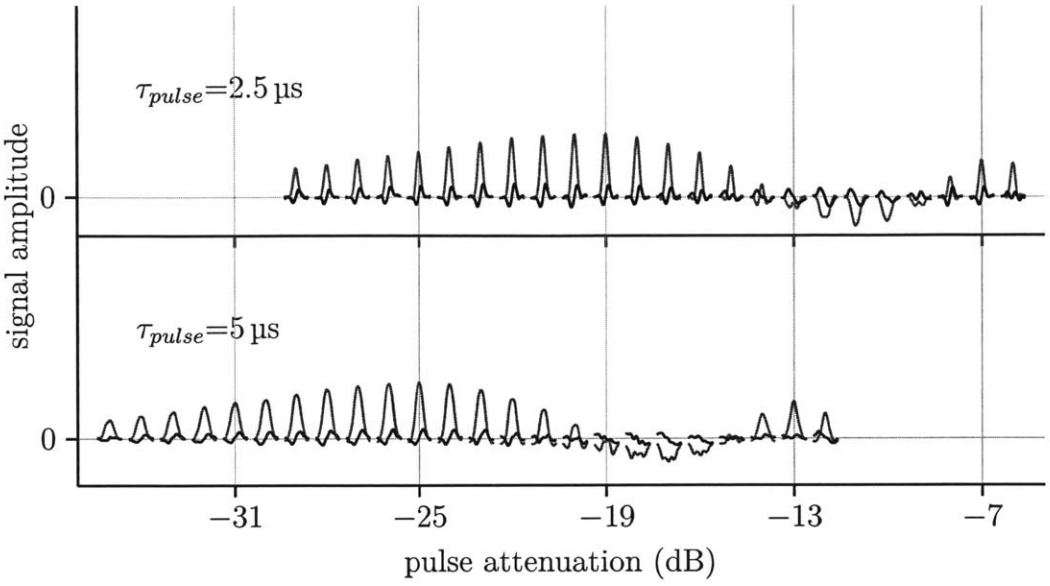


Figure 3-34: Verifying the measurement of an echo and scaling with pulse amplitude. The maximum echo amplitude represents the 90° condition.

## 3.8 Conclusion

This chapter presented both the theoretical view of wireless NMR as well as the physical manifestation of an implantable NMR probe. The probe allows high sensitivity remote measurement of a sample with very little interaction from the surrounding tissue. MRI is the only other method capable of isolating the signal from a specific point in space. An implanted NMR probe is ideal as a sensor since only one measurement is required from the entire sample .

Designing an NMR probe for implantation introduces a unique set of requirements. The largest sensor should be used for each application. The sensor size should be as large as the implantation needle, and the thinnest possible wire maximizes the sample volume and gives the best signal to noise ratio.

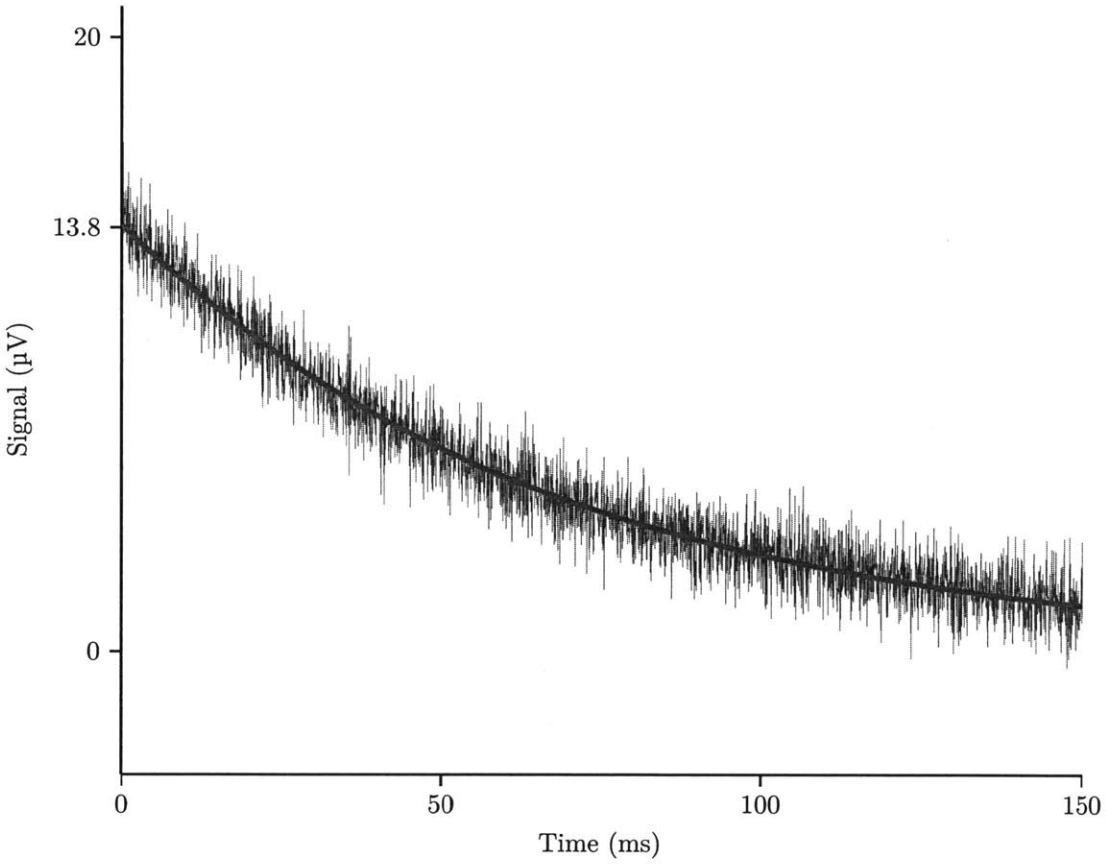


Figure 3-35: Transverse relaxation measurement acquired with an implanted sensor.

The reader must be optimized both to the sensor and to the target tissue. Small animals can be inserted into a reader coil, and a Helmholtz-type coil is optimal as it gives the best field uniformity. Larger animals and humans require a remote measurement for which an optimum reader radius exists. Loss inside the surrounding tissue is negligible. The large field amplification inside the sensor reduces the tissue losses even in extremely conductive media or at high frequencies. This could have applications both in higher field microimaging or in vivo spectroscopy where the tissue losses are more severe.

The implantable probe becomes a sensor only with the appropriate chemically sensitive NMR contrast agent. The following chapters present a few possible targets of interest.

THIS PAGE INTENTIONALLY LEFT BLANK

# Chapter 4

# Oxygen sensing

Living organisms depend on oxygen, and the overall health of living tissue can be assessed by measuring tissue oxygenation. A pulse oximeter is included on the cart that measures a patient's vital signs during any visit to the doctor's office or the hospital. The oxygen level of blood is calculated by tracking the color change between oxygenated and deoxygenated blood as the heart beats. This method does not work in the absence of a pulse or in tissue [67]. Similarly, blood oxygen level dependent (BOLD) MRI looks at perfusion differences across tissue. The contrast typically requires careful controls to determine which parts of the brain are activated by the stimulus [68]. Both techniques are extremely powerful but require known perfusion models to function. They do not work if blood flow is irregular or restricted.

Poorly oxygenated tissue is a result of poor local perfusion and has no impact on the oxygen level in the rest of the body. A generic whole-blood test cannot detect the oxygen state of a specific tissue. That information needs to be acquired directly at the site of interest. Normal tissue has an oxygen tension of approximately 5 kPa or

40 mmHg in customary units. Tissue below 2 kPa is hypoxic; anything below 200 Pa is considered severely hypoxic or anoxic [69]. The work in this chapter was performed in collaboration with Vincent Liu, Yibo Ling, and Syed Imaad.

## 4.1 Oxygen and cancer therapy

Radiotherapy creates DNA radicals that must react with oxygen to cause damage that will kill the cell [69]. Oxygenated tumors have been shown to require a lower radiation dose, while poorly oxygenated tumors are resistant to radiotherapy. Tumor hypoxia is predictive of the patient's outcome [70]. Low oxygen has also been implicated as a driving force for metastasis [9]. Knowledge of the tumor oxygenation would guide dose selection prior to treatment. Unlike a needle probe, an implanted oxygen sensor can be used over the course of therapy completely non-invasively.

The drug tirapazamine is actively being investigated to improve the action of chemotherapy and radiotherapy on hypoxic cells. Hypoxic conditions reduce the drug to form free radicals, which are believed to enhance the therapy [69]. However, clinical trials have not had promising results. A trial of tirapazamine in advanced non-small-cell lung cancer showed no benefit from adding tirapazamine [71]. A separate Phase III clinical trial investigated whether combining tirapazamine with cisplatin and radiation would improve outcomes in patients with advanced squamous cell cancer of the neck and head. The authors concluded that tirapazamine did not improve outcomes in patients "not selected for the presence of hypoxia" [72]. Tirapazamine is not expected to work in oxygen-rich tumors. An implanted oxygen sensor could identify patients with hypoxic tumors for whom tirapazamine is expected to work. The clinical trials could then be repeated in a hypoxia-selected population. If tirapazamine

were approved for treatment of patients with hypoxic tumors, a measurement of the oxygenation state of the tumor would be necessary, and an implanted oxygen sensor could provide that information.

## 4.2 Oxygen as a contrast agent

Paramagnetic species in solution reduce the longitudinal relaxation time [40, 29]. Molecular oxygen is paramagnetic because of two unpaired outershell electrons and must often be purged to measure a material's inherent $T_1$ [73]. Siloxanes are excellent hosts for oxygen as a contrast agent owing to their intrinsically long relaxation time coupled with a high oxygen solubility. A blend of two siloxane materials is used as an NMR oxygen contrast agent [74]. Polydimethylsiloxane (PDMS) serves as a matrix to support dodecamethylpentasiloxane (DDMPS). The formulation was developed through careful study of many different siloxanes. The final choice was a balance between the long-term stability of the larger molecular weight siloxanes and the high sensitivity of the shorter chains.

The transverses relaxation rate of a solution of viscosity, $\eta$, at a temperature, $T$, containing $N$ ions per cm$^3$ is given by

$$\frac{1}{T_1} = \frac{16\pi^2}{15} N_{ion} \langle \mu^2 \rangle \frac{\gamma^2 \eta}{kT}, \tag{4.1}$$

where $\mu$ is the net magnetic moment of the ion, $\gamma$ is the gyromagnetic ratio, $k$ is the Boltzman constant [29, p. 304]. This form is not appropriate for studying oxygen diffusion in a matrix-embedded material because it is impossible to measure viscosity. It is, however, possible to measure oxygen diffusivity in a solid either by using NMR

to track the diffusion of $T_1$ as the oxygen partial-pressure is adjusted [75]. The derivation of Equation (4.1) assumes that the ions and solute molecules are spheres with equal radii and diffusivities. The Stokes-Einstein relation is used to introduce the viscosity and temperature dependences. The ions are assumed to have point dipoles in the center, and the effective magnetic moment, $\mu$, is calculated assuming that the particles can only approach each other as close as one diameter.

Oxygen is much smaller than the siloxanes, and the closest distance of approach will be $(r_O + r_S)$. The diffusion coefficient of oxygen in the siloxane is also expected to be higher than the self-diffusion coefficient of the siloxane. The net distance between two diffusing particles after time $\tau$ is $\sim \sqrt{2\mathcal{D}\tau}$. If the diffusivities are very different then $2\mathcal{D} \rightarrow \mathcal{D}_O + \mathcal{D}_S$ [29]. The relaxation time due to dissolved oxygen is now given by

$$\frac{1}{T_1} = \frac{4\pi}{5} \frac{N\gamma^2\langle\mu^2\rangle}{(r_{Ox} + r_S)(\mathcal{D}_O + \mathcal{D}_S)} \tag{4.2}$$

where the explicit temperature dependence is lost. The diffusivity and solubility, however, will vary with temperature. The material's inherent relaxation is not included but will be considered using the relaxation time measurements in the next section. The equation suggests that the shortest $T_1$ is achieved in a material that has a high solubility but low diffusivity.

Table 4.1 has physical data for methyl siloxanes with between two and five silicon atoms per molecule. Siloxane self-diffusion coefficients were reported in the literature by McCall and Anderson [76]. Solubility was measured using gas chromatography [77]. Oxygen diffusivity was measured by relaxometry as the material was exposed to different oxygen environments. Calibrating the measured relaxation time in known concentrations of gas, the oxygen diffusion was tracked by measuring the

| Molecule | $N_{Si}$ | Mol. mass g/mol | $O_2$ Solubility mol/cm$^3$[77] | $O_2$ Diffusivity $\times 10^6$ cm/s$^2$[76] | Diffusivity $\times 10^6$ cm/s$^2$[75] |
|---|---|---|---|---|---|
| HMDSO | 2 | 162.4 | 2.2 | 20 | 4.2 |
| OMTSO | 3 | 236.5 | 1.18 | 17 | 2.95 |
| DMTSO | 4 | 310.7 | 0.71 | 14 | 2.14 |
| DDMPS | 5 | 384.8 | 0.49 | 13 | 1.59 |

Table 4.1: Siloxane molecule physical parameters and interaction with oxygen. The values are used in Equation (4.2) to estimate $T_1$.

| Full name | Molecule | $T_{1,N_2}$ ms | $T_{1,air}$ ms | $T_{1,pred}$ ms |
|---|---|---|---|---|
| Hexamethyldisiloxane | HMDSO | 7080 | 2000 | 2150 |
| Octomethyltrisiloxane | OMTSO | 5870 | 1740 | 1650 |
| Decamethyltetrasiloxane | DMTSO | 4670 | 1580 | 1420 |
| Dodecamethylpentasiloxane | DDMPS | 3920 | 1470 | 1100 |

Table 4.2: Measured and predicted values of $T_1$ for siloxanes in air. The sensitivity is ultimately determined by the very high inherent $T_1$ values of the material.

$T_1$ across the material. This approach yielded oxygen diffusivities in liquid siloxanes and matrix-embedded materials. The diffusivities reported for liquids are much high than the matrix embedded materials and are likely due to convective effects. The matrix embedded materials will not experience convection, and those diffusivities are used in the calculations [75]. All measurements were reported at room temperature (25 °C).

Measured and predicted values for $T_1$ are shown in Table 4.2. Longer chain siloxanes have lower relaxation times both in nitrogen and in air. The oxygen sensitivity of a sensor is determined by the total change in $T_1$ between the oxygenated and deoxygenated states and by the accuracy with which that change can be measured.

## 4.3 Oxygen sensitivity

A sensitivity metric for comparing materials must take into account the change in $T_1$ between high and low oxygen partial pressures as well as the baseline relaxation rates. The material has an inherent relaxation time, $T_1$, that is reduced to $T_{1,O}$ when fully oxygenated. The normalized signal from a saturation recovery sequence is

$$S(\tau) = 1 - e^{-\tau/T_1}, \tag{4.3}$$

where $\tau$ is the time that the material is allowed to recover from zero magnetization. The signal difference between the deoxygenated and oxygenated states is

$$\Delta S(\tau) = e^{-\tau/T_1} - e^{-\tau/T_{1,O}} \tag{4.4}$$

Differentiating with respect to time gives a recovery time, $\tau_{max}$, that maximizes the signal difference:

$$\tau_{max} = \frac{T_1 T_{1,O}}{T_1 + T_{1,O}} \ln \frac{T_{1,O}}{T_1}. \tag{4.5}$$

The total signal change $\Delta S_{max} = \Delta S(\tau_{max})$ is

$$\Delta S_{max} = \left(\frac{T_1}{T_{1,O}}\right)^{-\frac{T_{1,O}}{T_{1,O}+T_1}} - \left(\frac{T_1}{T_{1,O}}\right)^{-\frac{T_1}{T_{1,O}+T_1}}, \tag{4.6}$$

which, if $T_1 >> T_{1,O}$, simplifies to give,

$$\Delta S_{max} \approx \frac{T_1 - T_{1,O}}{T_1}. \tag{4.7}$$

That is, the metric for maximizing the signal is the fractional change in $T_1$.

The noise, $n$, on each measurement is independent of the sample and can be reduced by acquiring more data. Comparing materials requires a fixed measurement time, $t_m$. The scan time in a saturation recovery sequence is approximately $\tau_{max}$ such that the number of scans in a time, $t_m$, is

$$N_{scans} = \frac{t_m}{\tau_{max}}. \tag{4.8}$$

The measurement can also be improved by acquiring multiple echoes for each intensity measurement. The number of echoes that can be acquired will depend on the material's transverse relaxation time, $T_2$, and the echo time, $TE$. The total number of echoes will be proportional to $T_2/TE$. The signal-to-noise ratio will therefore be given by

$$\text{SNR} \propto \frac{\Delta S_{max}}{n} \cdot \sqrt{\frac{t_m T_2}{\tau_{max} TE}}. \tag{4.9}$$

The factors $t_m$ and $TE$ are chosen arbitrarily, and $n$ is fixed. All three are set to unity for simplicity. Under the assumption that the inherent $T_1$ is much longer than the oxygenated $T_1$, the signal-to-noise ratio equation is simplified:

$$\text{SNR} \propto \frac{T_1 - T_{1,\text{O}}}{T_1} \cdot \sqrt{\frac{T_2}{t_{max}}}. \tag{4.10}$$

This metric suggests seeking a materials with the largest possible fractional $T_1$ change with long transverse relaxation times. Liquid siloxanes have exceptionally long relaxation times, but their volatility limits long term implantation. A covalently bonded siloxane, instead of matrix-embedded liquid, is worth pursuing because it would have an indefinite lifetime. Solids can be characterized by exceptionally long $T_1$ but almost always have very short transverse relaxation times.

## 4.4 Oxygen sensitivity experiments

A blend of 30% PDMS (Sylgard 184, Corning) in DDMPS (Sigma) was used in the sensors. An amount of curing agent (Sylgard) equivalent to 1/10 the mass of PDMS was added. A sensor was filled with 10 µl of the siloxane and heated to 80 °C for 90 min. The sensor was mounted inside a gas flow tube inside the reader coil. A gas mixer (Pegasus systems) controlled the fraction of oxygen in nitrogen flowing at 50 $cm^3 min^{-1}$. Intensity data were acquired using a saturation recovery sequence at a single recovery time, $\tau$ =600 ms. The sensor responds reversibly to changes in the oxygen fraction and equilibrates in under 10 minutes (Figure 4-1). The resulting calibration curve of signal intensity versus oxygen fraction is shown in Figure 4-2. A linear response is not expected so the intensity is fit to a second order polynomial representing the series expansion of Equation (4.3). Fitting to this form yields an oxygen sensitivity of better than 1%. The single-point saturation recovery sequence is much faster than a full $T_1$ measurement and captures the dynamics of the sensor response. The $T_1$-weighted intensity can be converted to $T_1$ by solving Equation (4.3). In vivo experiments require a complete $T_1$ measurement, because the equilibrium magnetization will change between experiments.

## 4.5 Tissue oxygen measurements

Sensors filled with the siloxane blend were implanted in the calf muscle of Sprague-Dawley rats with a biopsy needle. The tissue oxygenation was modulated by switching the inspired gas from pure oxygen to air and by restricting the blood flow to the leg. The former approach monitors the transition to normal oxygenation from a

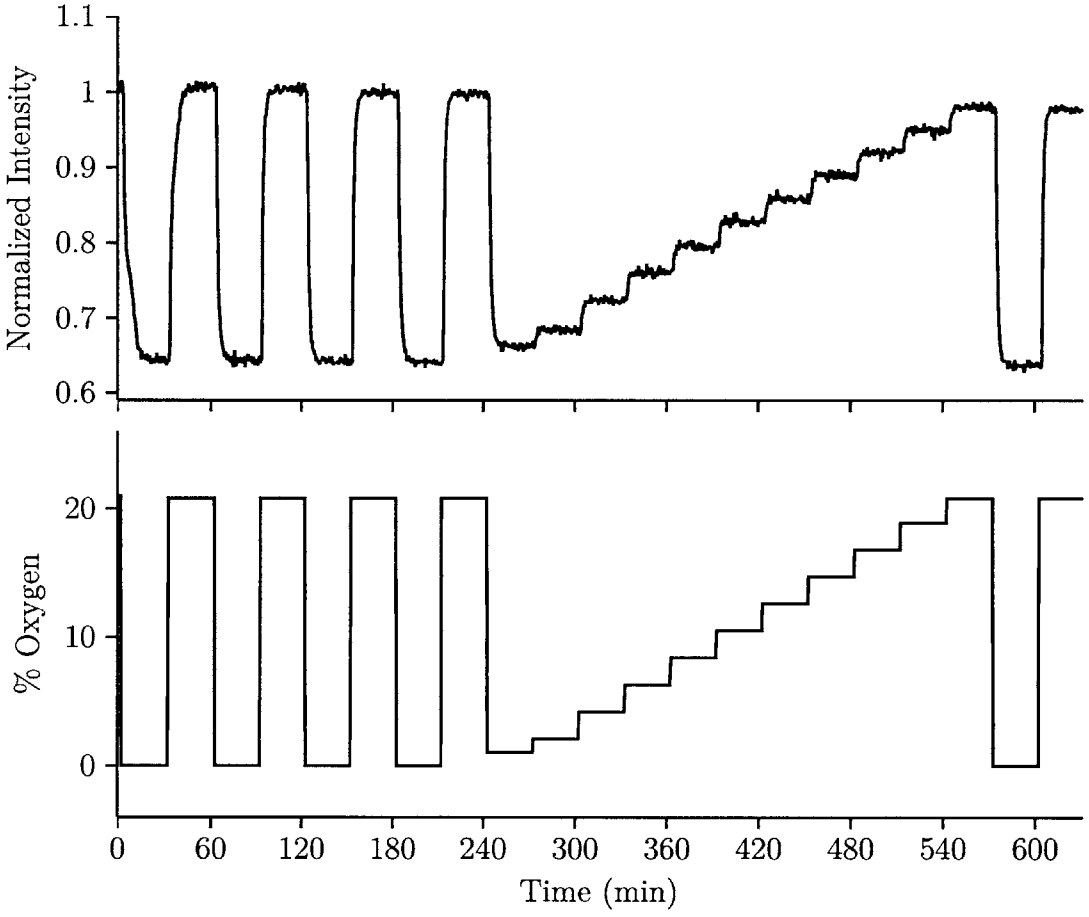


Figure 4-1: The oxygen sensor response (top) to changing oxygen fraction in a balance of nitrogen (bottom). Each condition was maintained for 30 min. A saturation pulse sequence with 600 ms recovery time yields a very fast $T_1$-weighted intensity measurement for monitoring dynamics.

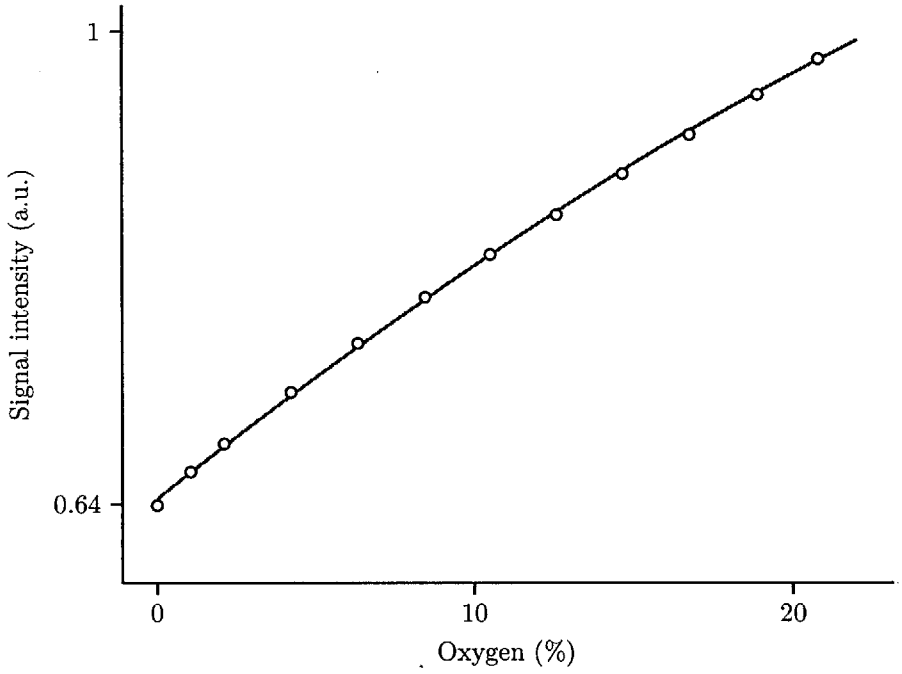


Figure 4-2: Calibration curve of $T_1$ weighted intensity versus oxygen fraction in nitrogen. The error bars are smaller than the marker size.

hyperoxygenated state, whereas the latter explores a hypoxic condition that mimics trauma or compressive injury.

### 4.5.1 Inspired oxygen

Rats are anesthetized using isofluorane gas delivered in a balance of oxygen. Changing the carrier gas to medical grade air, consisting of 21% oxygen in nitrogen, allows the tissue to return to ambient oxygenation. A single device was implanted in a rat gastrocnemius muscle, and measurements were made twelve days later. Oxygen was maintained for one hour before switching to air. The gas was changed back to oxygen 30 min later. The transition from oxygen to air caused an increase in $T_1$; no change was observed in the transition back to oxygen. Other researchers have noted that the recovery is both slower and less pronounced [78]. It is likely that a longer wait time at each level is needed.

### 4.5.2 Restriction of circulation

An oxygen sensor was implanted in the calf muscle of an anesthetized Sprague-Dawley rat using a biopsy needle. The sensor was monitored for two hours. The relaxation time increased over the course of the measurement, consistent with a decreasing oxygen concentration inside the sensor chamber. The sensor was initially in ambient air and then implanted into muscle, which has a lower oxygen concentraion. The sensor $T_1$ is expected to increase immediately after implantation as the oxygen diffuses out of the sensor. Approximately one hour was needed to equilibrate with the tissue. There is evidence that some of the liquid phase siloxane (DDMPS)

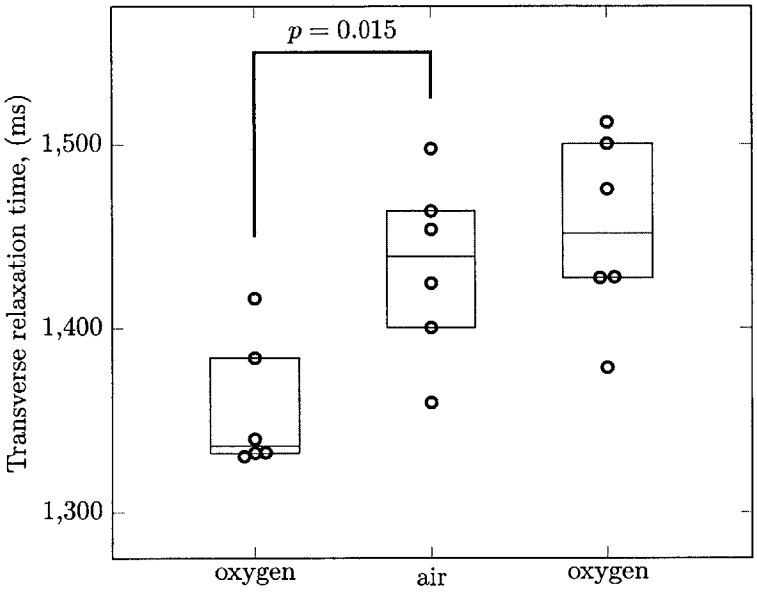


Figure 4-3: Boxplot of $T_1$ measured by a sensor implanted in a rat calf muscle. The inspired gas was changed from oxygen to air, and an increase in $T_1$ followed. A second transition back to oxygen did not show a corresponding difference. A longer time might be needed for the recovery.

diffused into the muscle tissue. The equilibrium signal amplitude, $S_0$, decreased by 30% two hours after implantation.

A measurement eight days after implantation included a flow restriction to the leg. The animal was kept under anesthesia for over an hour to ensure that the muscle and sensor were fully oxygenated. A nylon cuff, lightly tightened around the thigh, reduced the blood flow to the limb. An increase in the relaxation time was observed after the restriction ($p < 0.01$), consistent with a lower oxygen tension in the muscle tissue. The data are shown in Figure 4-4.

## 4.6 Prospects

Tissue oxygen tension is an important parameter not only for cancer but also for heart disease, traumatic injury, and compartment syndrome. The experiments shown in this chapter demonstrate a method for wirelessly measuring tissue oxygenation. The siloxane is not a contrast agent but has a very high oxygen solubility and a long inherent $T_1$. The oxygen that diffuses into the siloxane significantly impacts the measured $T_1$ as predicted by the theoretical model. The silicone is hydrophobic and fully dense; it will exclude water, proteins, and immune cells when implanted in the body. The other gases that can diffuse into the polymer, such as nitrogen and carbon dioxide, are not paramagnetic and will not influence the measurement. The sensor will only measure oxygen inside the body.

Some of the liquid siloxane may be escaping from the matrix into the muscle tissue. Other siloxanes should be explored that covalently bond the long chains to a backbone molecule. Covalently bonded molecules cannot escape from the sensor chamber,

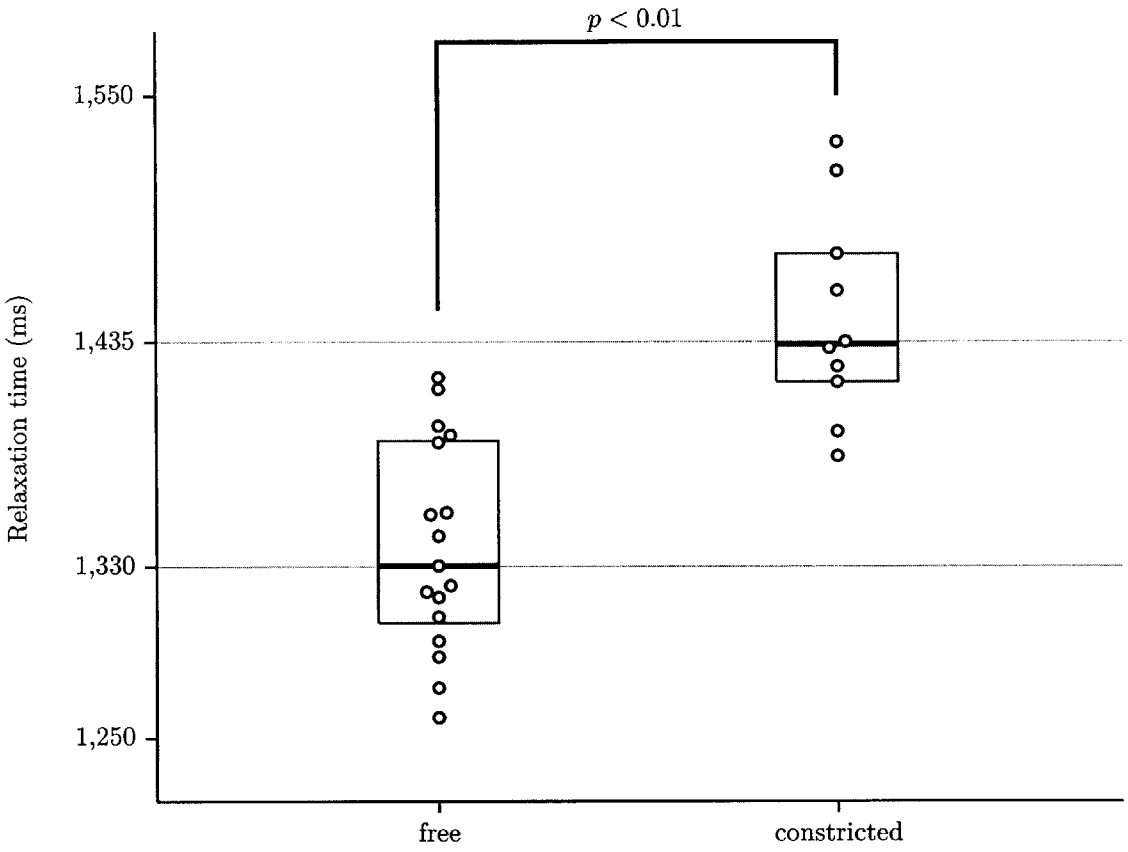


Figure 4-4: $T_1$ measured in a calf muscle under free and constricted circulation. A significant increase in relaxation time is observed after applying light pressure to the thigh.

and the sensor will be stable indefinitely. The covalent bonding, however, is likely to reduce the transverse relaxation time, $T_2$, and the overall sensitivity will suffer. The sensitivity metric of Equation (4.10) can be used to select the best candidate material.Alternatively, a uniform-field magnet could provide sufficient signal to differentiate between the matrix and liquid components to compensate for any change in the blend ratio.

THIS PAGE INTENTIONALLY LEFT BLANK

# Chapter 5

# pH sensing

Measuring pH in the body can serve as a general and non-specific indicator of tissue health. Damaged cells release their acidic contents into the surrounding environment. Solid tumors are known to be acidic compared to normal tissue because cancer cells undergo anaerobic respiration, producing lactic acid as a by product [79]. Tumors induce the formation of blood vessels to provide oxygen and nutrients, but these vessels form in a haphazard arrangement that leaves some regions poorly perfused. Cancer cells begin to die in those regions, which become necrotic and more acidic [11]. Chemotherapy, when effective, initiates the cells' self-destruct mechanism (apoptosis), and the acidic contents of the cell are released into the extracellular space. The tumor environment is usually pH 6.5 and becomes more acidic, around pH 5.5, when the treatment is successful [70]. None of the local pH changes in the tissue would manifest themselves in systemic measurements of pH; the body has multiple buffering mechanisms to maintain very strict control over the pH. Tissue pH must, therefore, be measured at the site of interest.

## 5.1 Electrochemical pH sensors

Electrochemical probes are the gold standard for measuring pH, and certain models are built into a hypodermic needle for tissue measurement. Direct tissue measurements are possible, but these probes cannot be left behind for repeat measurements. Each measurement is invasive and requires anesthesia and image guidance. Plus, the heterogeneous makeup of tumor cells and vessels results in regions of higher and lower pH. Repeat measurements that seek to track therapy are unlikely to measure the same location twice. Instead of measuring a trend over time, they would determine the range of pH across space. An implanted sensor will monitor a single location over time. It is the preferred approach for detecting changes in pH in response to treatment because it will eliminate variations due to placement.

Electrochemical sensors are extremely fast and accurate if calibrated against known pH buffers. A voltage, measured across two electrodes, is converted to a pH by calibrating against known buffers. Long term or repeat monitoring is possible, but periodic recalibration is required. The electrodes are prone to contamination and are incompatible with certain ion species. The possibility of implanting the pH electrode in the body permanently presents many insurmountable challenges. One study implanted a small vessel with an electrode solution directly into a tumor. This created a clean chamber into which a needle probe was inserted to measure the pH. This arrangement enabled the repeat sampling of the same point in the tumor and eliminated the possibility of contamination, but it still required multiple invasive procedures for the patient. The researchers demonstrated that the tumor pH decreases when the chemotherapeutic is successful and highlighted the benefits of tracking intratumoral pH in the clinic. Their approach may not translate into the

clinic; as the authors themselves noted, "a modified system of measurement would be required for routine clinical application [...] The obvious problem with this approach is the innate, potential discomfort for patients" [70].

The wireless implantable sensor presented in this thesis overcomes these limitations while still measuring the same location. Implanted during the biopsy procedure, the sensor is no more invasive for the patient than existing practice. Repeat measurements are completely non-invasive. The work in this chapter was performed in collaboration with Vincent Liu.

## 5.2 HEMA-BIS gels for pH measurements

The sensing medium consists of hydroxethyl methacrylate (HEMA), which has a long history of use in contact lenses [80]. The gel is formed by crosslinking HEMA with bismethacrylate (BIS). The reaction is a simple free-radical polymerization that occurs in an oxygen-free environment and that is completed in several hours at room temperature. The wireless sensors can be filled directly with the prepolymerized mixture, and the reaction proceeds inside the chamber.

The gel is a weak acid with an acid dissociation constant p$K_a$. Protons on the gel can be exchanged with protons on the surrounding water molecules, and the rate of exchange is pH-dependent [?]. The NMR relaxation of protons on the polymer is very fast compared to the relaxation in water. The combination of pH dependent exchange with differing relaxation rates gives rise to pH-dependent NMR contrast. Acidic conditions with pH values below the p$K_a$ result in more protons associated with the polymer chain. The resulting $T_2$ is shorter because the fraction of faster

relaxing protons is greater. Basic conditions, pH > p$K_a$, fully dissociate the acid, and the polymer has a smaller impact on the overall relaxation.

The gel is a weak acid, and its buffering ability must be fully overcome to measure the $T_2$ versus pH calibration curve. A small amount of gel is tested in a large bath of pH-adjusted fluid; the large volume excess of the bath over the sensor ensures that the bath pH will not be affected by changes inside the gel. The gel is loaded into a sensor, which confines the measurement to the gel, and no signal is detected from the fluid bath. The sensor was mounted inside a 6 mm diameter plastic tube and centered inside the reader coil. Approximately 500 mL of saline solution was maintained at 37 °C in a circulating water bath. The solution pH was adjusted with concentrated hydrochloric acid or soduium hydroxide and measured with a pH meter (Omega). Continuous flow over the sensor was maintained with a peristaltic pump (Masterflex).

Data acquired over a period of approximately 25 days are shown in Figure 5-1. The saline pH was adjusted in discrete steps between pH 4.8 and pH 7.5. The sensor responds reversibly and equilibrates in approximately 24 hours. The equilibrium $T_2$ versus pH data are shown in figure 5-2. The $T_2$ is shortest at low pH, which is consistent with more coordination of the protons on the polymer chain. The $T_2$ increases with increasing pH, as expected, but drops above pH 6.8. This drop is likely due to a second exchange mechanism becoming active. There are multiple exchangeable protons along the polymer chain, each with a potentially different dissociation constant [81]. Each site may also differ in its chemical shift such that a high-field spectrometer could distinguish each individual site. A sensor measured with a single-sided magnet cannot observe chemical shift. and only the aggregate relaxation is detected. Tumor pH, however, will mostly be restricted to the left portion

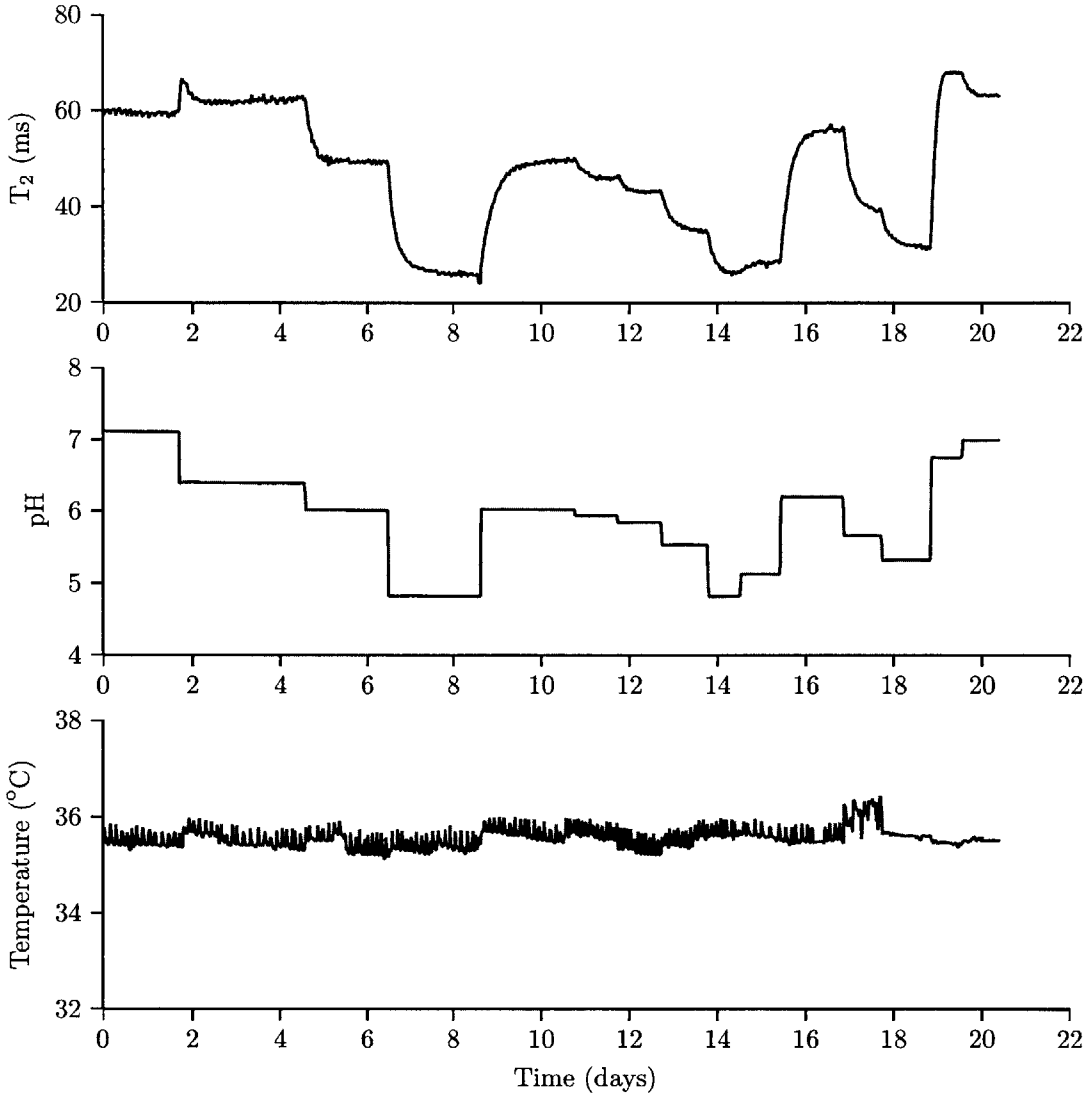


Figure 5-1: Measurements of $T_2$ versus pH of a saline solution using HEMA-BIS gel inside a sensor. A peristaltic pump maintained a constant flow of saline from a temperature controlled bath over the device. A pH probe in the bath monitored both temperature and pH.

of the curve, and it is the low-pH regime that is of interest.

The monotonic portion can be modeled as a weak acid with a dissociation value p$K_a$. The model assumes that there are two distinct relaxation rates; relaxation is fast on the polymer chain and slow in free water. The pH versus $T_2$ data are fit to the following form:

$$\frac{1}{T_2} = \frac{1}{T_{2,0}} + \frac{1}{T_{2,b}(1 + 10^{\mathrm{pH-pK_a}})}, \tag{5.1}$$

where $T_{2,0}$ and $T_{2,b}$ represent relaxation parameters to be found. More basic conditions, pH $\gg$ p$K_a$, result in $T_2 - > T_{2,0}$, whereas acidic conditions pH $\ll$ p$K_a$ eliminate the exponent, and $1/T_2 = 1/T_{2,0} + 1/T_{2,b}$.

The gel would need to be modified to measure healthy tissue because normal pH is outside the monotonic regime; the acidic pH of a tumor, however, is within the sensitive range. The sensitivity in this regime can be explored using the measurements that generated the calibration curve. The predicted pH from each $T_2$ measurement is compared to the pH of the saline bath. Figure 5-3 shows a histogram of the difference between predicted and actual pH values from 1,010 measurements. The limit of detection is better than 0.1 pH units across the monotonic regime.

## 5.3 Temperature dependence

The temperature of the saline bath was changed between room temperature and approximately 50 °C. The measured relaxation time decreases with increasing temperature. The data are plotted in Figure 5-4 for three different values of the solution pH. The temperature range expected in the body will not vary by more than a few degrees Celsius. The temperature-induced change in $T_2$ is unlikely to significantly

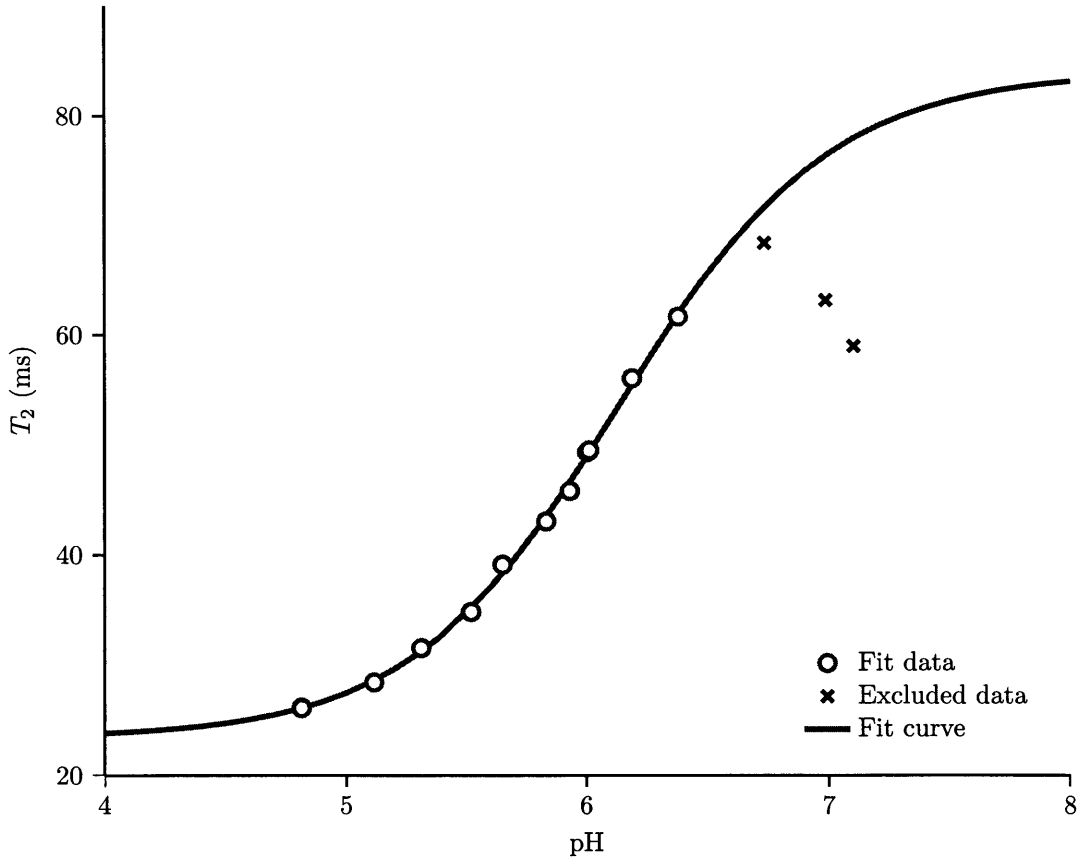


Figure 5-2: $T_2$ versus pH calibration curve.

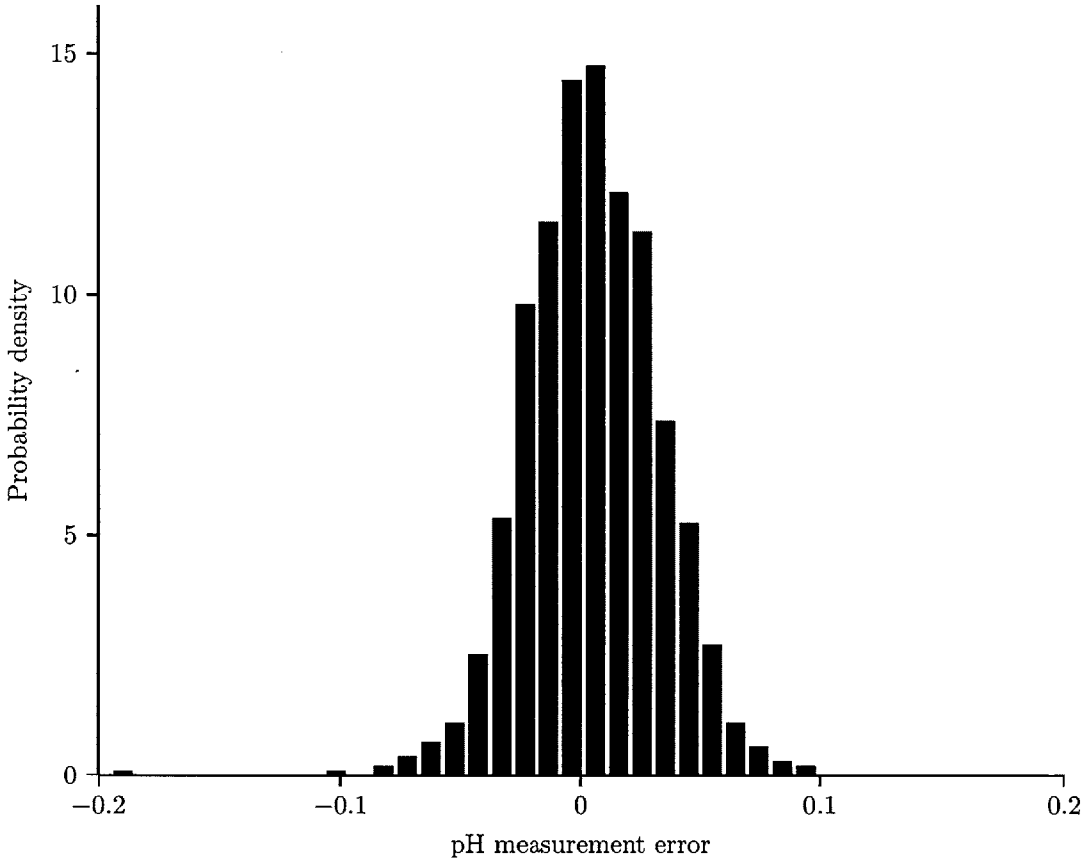


Figure 5-3: Histogram of pH measurement error establishing a limit of detection better than 0.1 pH units.

impact the measurement, but the calibration curves should be acquired close to body temperature.

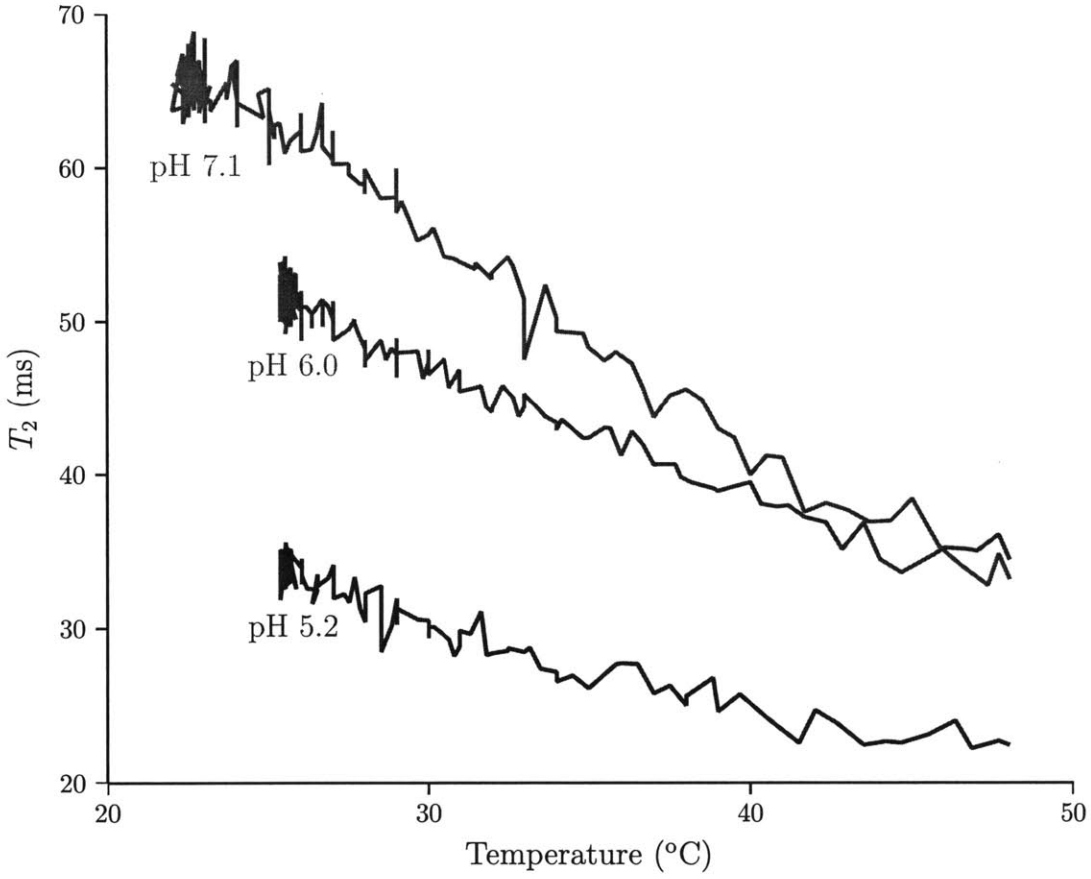


Figure 5-4: The measured $T_2$ decreases with temperature. The expected temperature deviation in vivo is very narrow compared to the studied range, but the calibration curve must be performed at body temperature.

| Parameter | Value | Description |
|---|---|---|
| $N_{scans}$ | 16 | number of averaged scans |
| TR | 1250 ms | repetition time |
| TE | 50 µs | echo time |
| $N_{echoes}$ | 3000 | number of echoes |
| $Att_{90}$ | -18.5 dB | pulse attenuation |
| $t_{90}$ | 2.5 µs | pulse duration |
| $N_{samples}$ | 32 | samples per echo |
| $dt$ | 0.5 µs | dwell time per sample |

Table 5.1: Acquisition parameters for measuring the transverse relaxation time, $T_2$.

## 5.4 Pilot study

Four C57-BL6 breed mice were inoculated subcutaneously with melanoma cells derived from the same breed. Sensors were implanted after one week using a biopsy needle. One was implanted directly inside the tumor, a second was implanted adjacent to the tumor and a third was implanted on the contralateral side. A fourth animal had no sensor implanted to ensure that the signal was indeed from the sensor and not from the surrounding tissue. The animals received daily injections of doxorubicin into the peritoneal cavity and the sensors were measured. No signal could be detected from the mouse that did not have an implanted sensor, confirming that the signal is from inside the sensor and not a measurement of the tumor by the reader coil.

Each relaxation measurement took approximately four minutes with the acquisition parameters listed in Table 5.1. Multiple measurements were acquired and averaged during post-processing. The echo amplitudes were estimated using the least-squares method outlined in Appendix A.

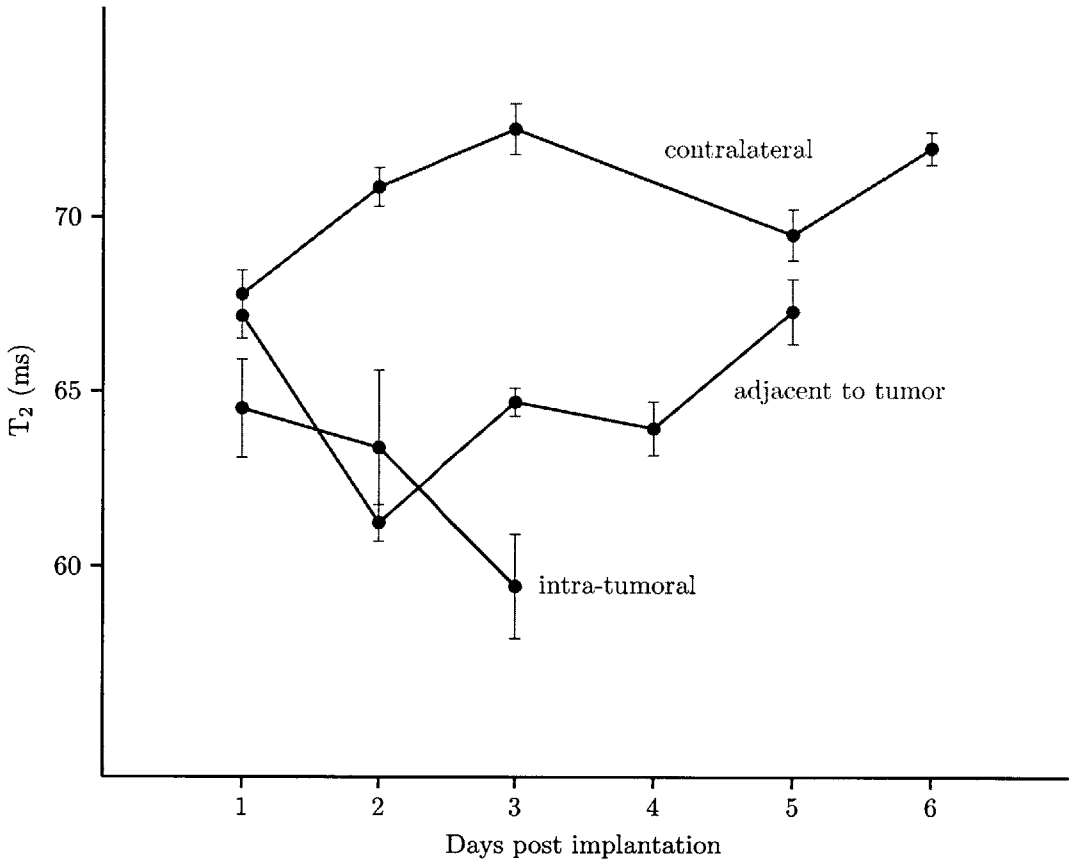


Figure 5-5: Relaxation time measurement for sensors implanted inside, near, and contralaterally to the tumor. The sensors on the tumor side measured a shorter $T_2$, consistent with a lower tissue pH.

The results from the three implanted sensors are shown in Figure 5-5. The sensor on the contralateral side shows a sustained high $T_2$ over the course of 6 days. The sensor implanted adjacent to the tumor shows a lower $T_2$ for the first few days but the lowest pH is recorded in the sensor implanted inside the tumor. This experiment demonstrated in vivo operation of the implantable NMR probes. The difference between the tumor-side and contralateral implantation are in agreement with the expected pH of cancerous tissue versus normal tissue.

## 5.5 Detecting chemotherapeutic efficacy

Determining chemotherapeutic efficacy represents a challenging problem in the clinic but one that can have profound impact on the course of cancer therapy. The difficulty in a research model is to separate the morphological changes in a growing tumor from the immediate effect of the treatment. If the tumor proliferates rapidly, some regions may become starved of nutrients and become necrotic. Necrosis is different than apoptosis, which is the cells' controlled self-destruct mechanism, that can be induced by chemotherapy. The pH change is a general indicator of cell death regardless of the origin.

A pilot study between treated and untreated animals suggests that 95% significance would be achieved with six mice per group. Twelve mice were inoculated with the melanoma cells. Sensors were implanted inside the tumors approximately ten days later. The mice were randomly assigned to a treatment group (N=6) or a control group (N=5). The treatment group received daily intraperitoneal injections of doxorubicin. The dose was proportional to the mass of the mouse (0.02 mg/g). The control group received a saline injection of similar volume. The mice were monitored

carefully for any signs of distress, and the experiment continued for four days.

The sensors were measured daily after each injection. The results show no separation between the two groups (Figure 5-6). The spread in $T_2$ measured on Day 1 is expected because tumors are heterogeneous and each sensor measures a slightly different environment. Because the initial pH may vary depending on location, it may be better to look at changes in pH over time rather than an absolute pH. However, there is still no discernible difference between the treated and untreated mice.

It is useful to investigate the normal range of pH (or relaxation time) in untreated tumors. The pH will depend on the exact location of the sensor inside the tumor. All of the measurements on Day 1 were prior to treatment and are included in the analysis. Figure 5-7 shows a slow decrease in the mean $T_2$ at a rate of approximately 1.5 ms/day. The slope is negative with 95% confidence indicating that the tumors are becoming more acidic as they grow. The majority of measurements are between 55 ms and 65 ms corresponding to pH 6.5 and higher. The lowest pH measured using the implanted sensor was approximately pH 6.

A tumor growth study without an implanted sensor showed significant tumor cell death even in the untreated mice. One histologic section stained with hematoxylin and eosin (H&E stain) is shown in Figure 5-8. The dark brown spots are melanin and are characteristic in melanoma. The H&E stains cell nuclei blue/purple while the cytoplasm and other proteins are pink. Significant regions without cell nuclei are necrotic and contain no living cells. Apoptosis, caused by the chemotherapy, would be visible inside the regions with living, well-perfused melanoma cells. The extent of tumor necrosis is apparent in a side-by-side comparison of treated and untreated tumors (Figure 5-9). The similar staining pattern suggests that the drug dose was not sufficient to cause a significant change in the tumor compared to its natural

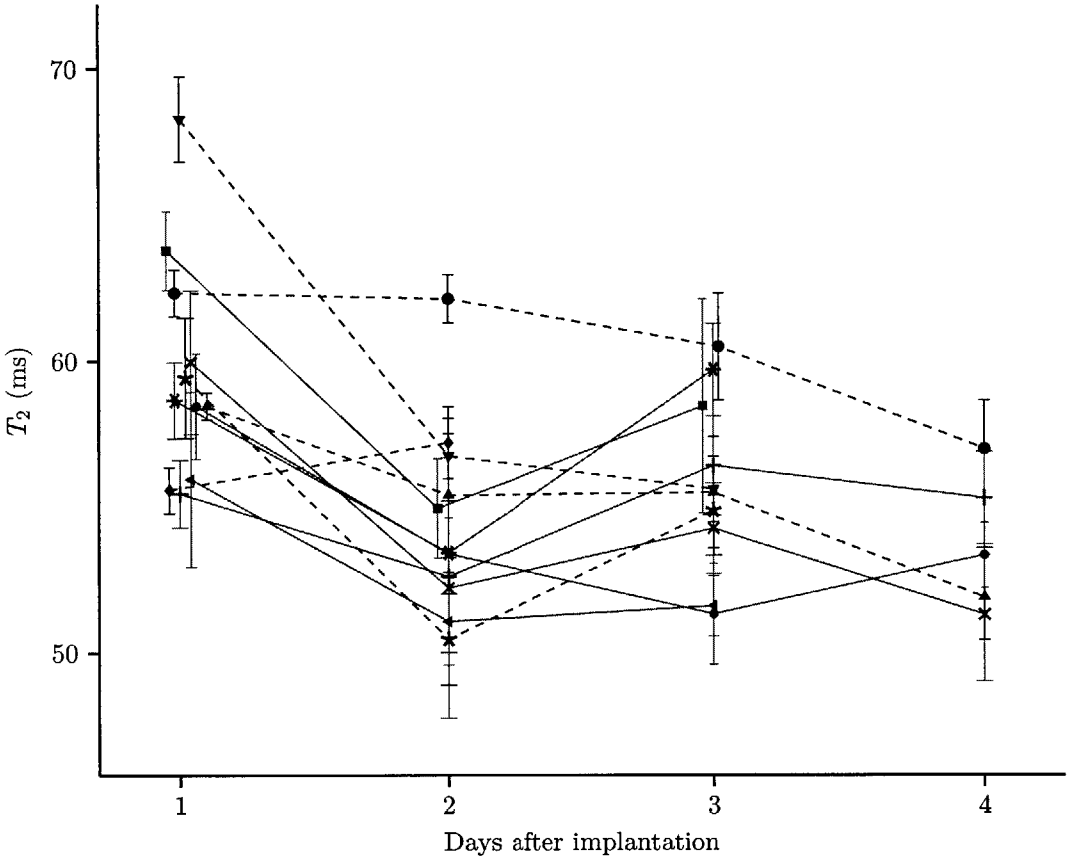


Figure 5-6: Measured relaxation times for sensors implanted in mouse tumors. Those animal receiving treatment (doxorubicin) are shown as solid red lines, and the control group that received saline injections are shown in dashed black lines. Each line represents a different animal. No discernible pattern emerges between the two groups suggesting that this dose had no effect on the tumor pH.

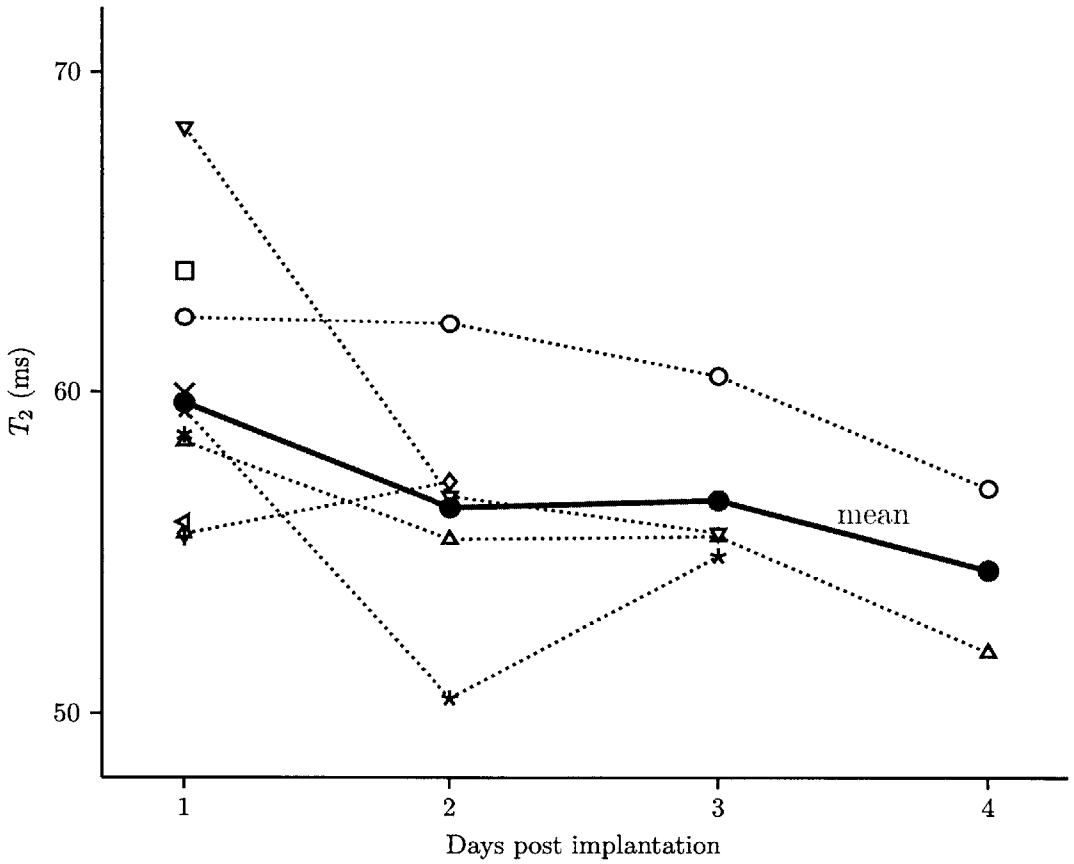


Figure 5-7: Measured relaxation times for implanted sensors that received no treatment. The mean $T_2$ (thick red) decreases over the four days of implantation consistent with a net trend towards more acidic conditions in the tumors.

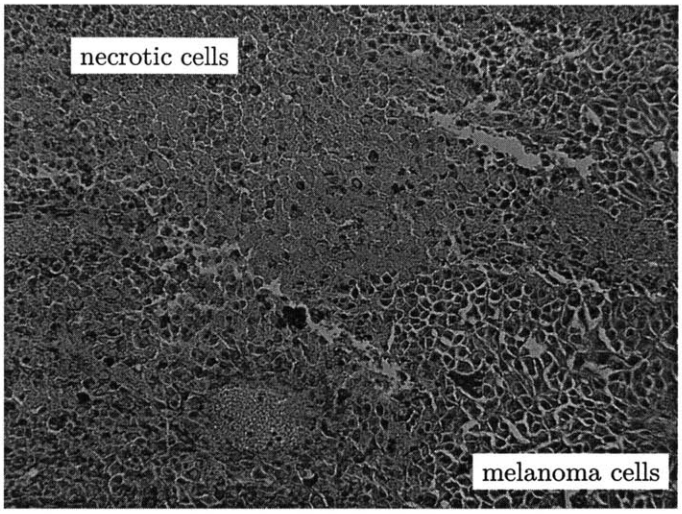


Figure 5-8: Histologic section of an untreated tumor (H&E stain). Significant regions of necrotic tissue are mostly stained pink. Healthy melanoma cells have purple-stained nuclei. The brown spots are melanin, characteristic of melanoma.

progression. A higher dose is likely necessary to ensure that chemotherapy-induced apoptosis, and not necrosis, is the predominant cause of decreasing pH.

## 5.6 Conclusion and future work

The implantable probe loaded with HEMA-BIS gel was shown to detect pH accurately in pH adjusted saline over the range of pH expected inside a tumor. The sensors are reversible, equilibrate in 24 h, and are stable for almost a month.

Implanted inside tumors in a mouse melanoma model, the sensors were unable to distinguish between treated and untreated mice. Histological analysis found similar patterns of necrosis in both groups suggesting that there was no underlying difference for the sensors to detect. It is, indeed, possible that the sensors correctly

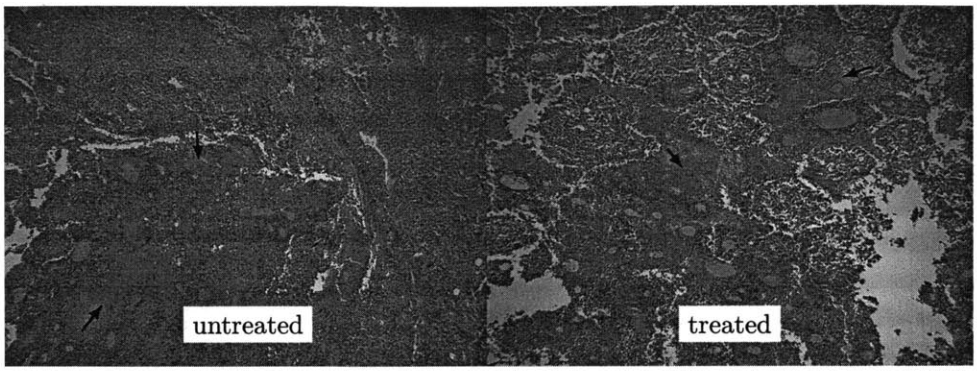


Figure 5-9: H&E stained sections of treated and untreated tumors. Substantial regions of necrotic tissue (pink with no purple stained nuclei) are apparent in both sections.

demonstrated that the drug was not effective.

Histology also revealed an increase in the amount of necrotic tissue over time; this is consistent with gradual decrease in $T_2$ over the course of the measurement. The spread in relaxation time measured across animals is expected. The pH will vary depending on where inside the tumor the measurement is made. Implanted sensors have a significant advantage over needle probes because they measure the same spot repeatedly.

This study does not definitely prove pH as a marker for detecting treatment efficacy. Future studies should establish a treatment regimen that produces a profound tumor change. The protocol will require a higher doxorubicin dose to ensure tumor cell death. If possible, the sensors should be implanted in smaller tumors, which have less necrotic tissue, to reduce the effect of necrosis on the pH change. A doxorubicin resistant cell line derived from the same melanoma model will provide the control experiment.

THIS PAGE INTENTIONALLY LEFT BLANK

# Chapter 6

# Detecting protein biomarkers

Soluble proteins, measured in blood, can serve as markers of biological activity. Blood tests can indicate the onset of a myocardial infarction (heart attack), predict some types of cancer, and report on the function of several organs. Detecting these biomarkers with an implanted device could serve as an early warning system or provide feedback on the progress of treatment.

Magnetic nanoparticles with a polysaccaride coating are used as contrast agents in NMR [82]. Antibodies conjugated to the particles form a protein-dependent contrast agent. The functionalized particles aggregate around the protein of interest and change the transverse relaxation rate of the solution. The resulting $T_2$ can be correlated to the amount of bound protein [83].

One example protein is human chorionic gonadotropin (hCG) that is produced by choriocarcinoma. Particles functionalized with anti-hCG antibodies were encapsulated in a device using a semipermeable membrane. The device is shown in Figure 6-1. The membrane has pores that are smaller than the particles but larger than

the protein; it traps the particles while allowing the protein to diffuse freely into the chamber. The relaxation time was measured using magnetic resonance imaging (MRI). Devices implanted in a mouse cancer model demonstrated detection of the cancer marker [84].

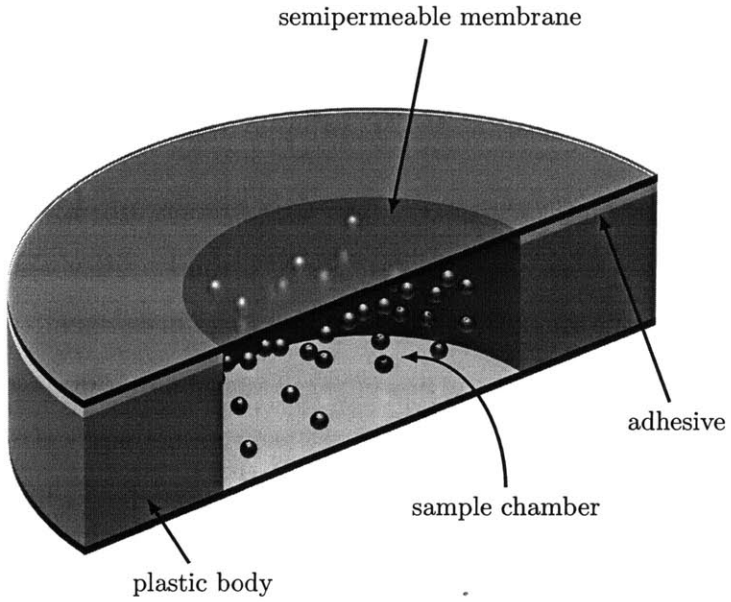


Figure 6-1: Prototype device used to test protein detection. Sensitive nanoparticles are encapsulated in a plastic body using a semipermeable membrane that keeps the nanoparticles in but allows the target to pass.

Ling et al. developed a multiplexing technique that uses a single class of particles functionalized with secondary antibodies against mouse antibodies. Any mouse-derived primary antibody can be added to these particles to form a vast array of protein-sensitive contrast agents [85]. Multiple reservoirs can be built on a single device to detect a panel of protein biomarkers [86].

Cancer biomarkers are an area of active research, but their utility has proven controversial. Elevated levels of prostate specific antigen (PSA) were thought to be pre-

dictive of prostate cancer, but recent work has cast doubt on that conclusion. The original analysis was confounded by the very high prevalence of enlarged prostate, and PSA levels are far less predictive of prostate cancer. The absolute blood PSA concentration that triggers further tests has increased the number of unnecessary biopsy and surgical procedures [87, 88]. Should cancer biomarkers be discovered that are diagnostic or predictive, then nanoparticle-based agents can quickly be created to detect them. The sensing technology is instead tested in a different model for which the diagnostic concentrations are known.

## 6.1 Cardiac biomarkers

Cardiac markers follow a very well known profile following cardiac tissue damage. A panel of proteins can determine whether heart tissue damage has occurred within the past 72 hours. The myocardial infarction model was chosen as a better proxy for testing protein sensors.

Disc sensors (Figure 6-1) were filled with nanoparticles functionalized with antibodies against a standard cardiac panel: myoglobin, troponin I, and creatine kinase MB (CKMB). The sensors were tested in saline solution spiked with varying concentrations of the three proteins and in a mouse model of myocardial infarction.

Research presented in this section was performed in collaboration with Yibo Ling and Terrence Pong [89, 90].

### 6.1.1 Exposure

The antibody-protein interaction is generally irreversible, and so the sensors will continuously collect the protein. The measurements contain the history of the concentration profile. Integrating the concentration, $C(t)$, as a function of time yields an exposure. The exposure measurement reflects the total amount the device has been exposed to up until that point in time. This is formally defined as

$$E(\tau) \equiv \int_0^\tau C(t) d\tau. \tag{6.1}$$

Ten identical myoglobin sensors were exposed to different concentration-time profiles. They were measured continuously over a period of several days. The sensor response to constant concentrations is shown in Figure 6-3. The sensors show a continuously increasing $T_2$ over time. The rate of increase of $T_2$ depends on concentration, but the final value is the same for all conditions, suggesting that the antibodies are fully saturated. Plotting $T_2$ versus exposure collapses the curves onto a single, characteristic $T_2$-exposure profile. Furthermore, the sensors exposed to transient concentration profiles also lie along the $T_2$-exposure curve (Figure 6-4).

### 6.1.2 Mouse myocardial infarction model

The dosimeter property was exploited in a mouse myocardial infarction (MI) model. The left anterior descending artery was ligated with a suture to cause downstream tissue damaged. A sham procedure involved all of the steps except the ligation, and a control group received no procedures. Sensors were implanted subcutaneously in all

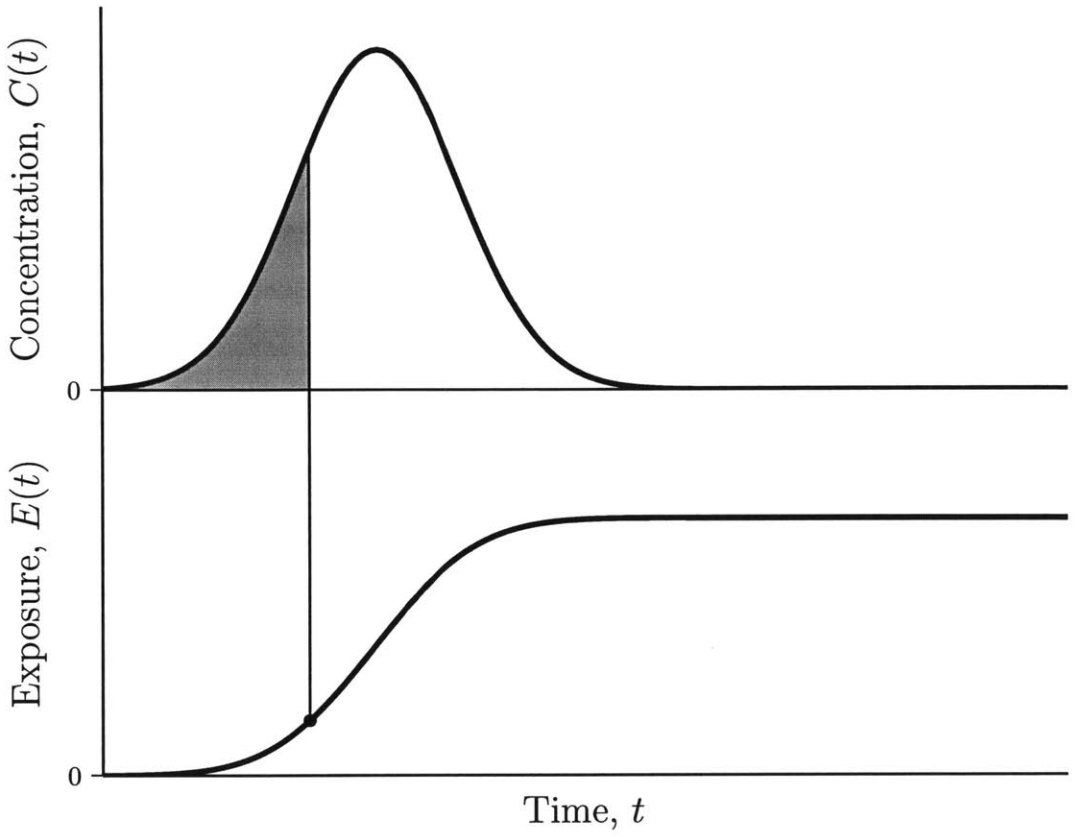


Figure 6-2: Antibody based sensors measure exposure, defined as the time integral of concentration. Transient events can be detected because exposure remains high even after the concentration has subsided.

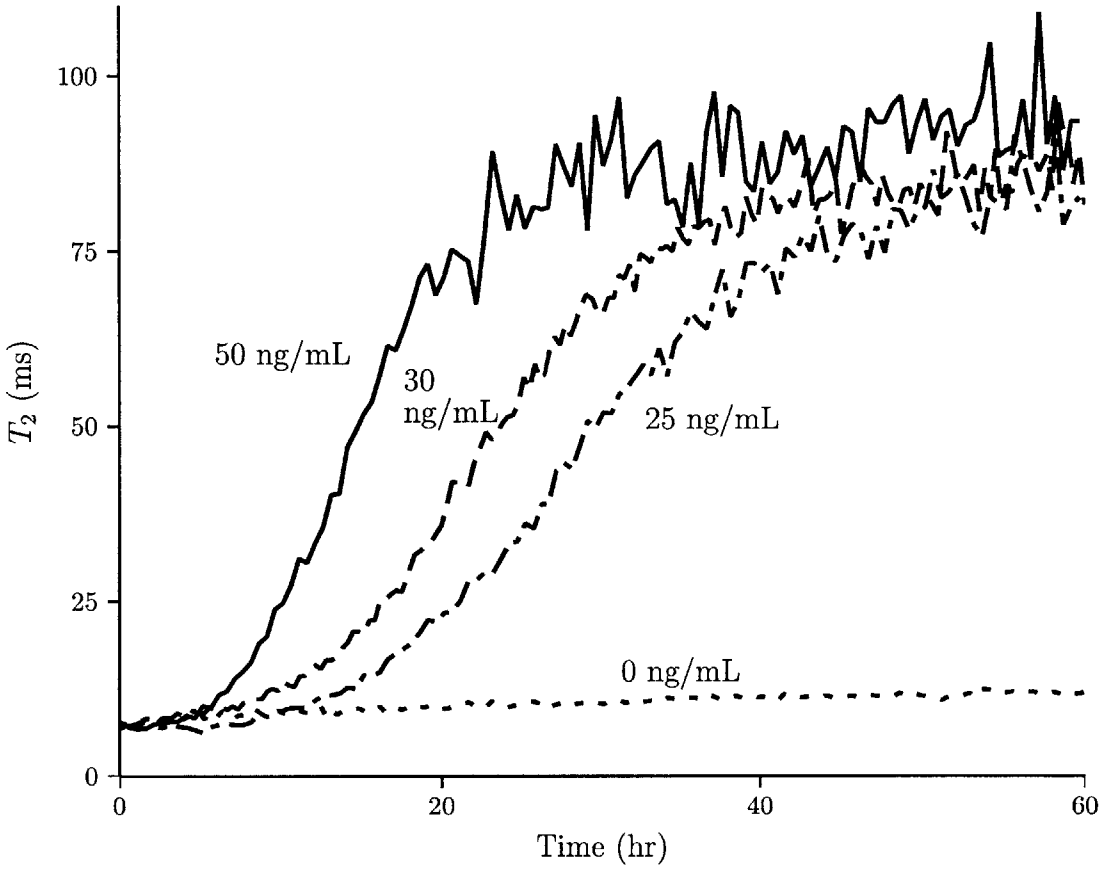


Figure 6-3: Measured $T_2$ versus time. Sensors exposed to steady concentrations of myoglobin respond at different rates but saturate to the same value. Adapted from Ling, Pong, Vassiliou et al. [89].

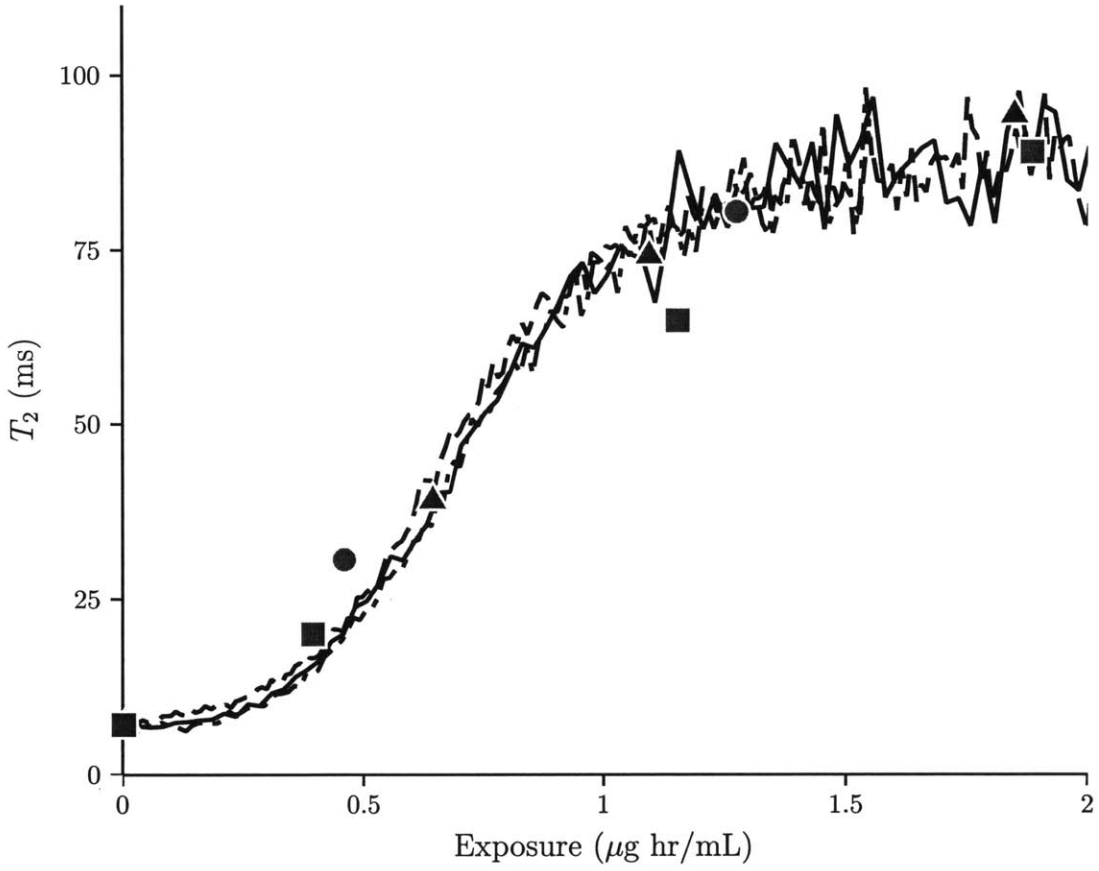


Figure 6-4: Measured $T_2$ versus myoglobin exposure. The measurements from Figure 6-3 all lie along a characteristic $T_2$ vs exposure curve. Transient profiles (markers) simulate one-off events and also lie along the curve. Adapted from Ling, Pong, Vassiliou et al. [89].

of the animals and were explanted the following day for measurement. The sensors distinguished the MI group from the other two groups. Furthermore, the change in relaxation time correlated with the amount of tissue damage as determined by histology of the heart tissue [89]. A single concentration measurement in blood does not give any information on how much tissue was damaged. This study demonstrated that protein biomarkers can be detected with subcutaneously implanted sensors; the sensors do not need to be implanted near the heart. It suggests that other soluble proteins detected with a blood test are also possible targets for a subcutaneous sensor.

### 6.1.3 Future cardiac sensor applications

The study points to a clear application for monitoring patients at risk for a heart attack. A small sensor implanted under the skin could be tested daily, at home, or during routine visits to the doctor's office. Detecting silent MIs, those that are not felt by the patient, would ensure that the patient received prompt care and followup treatment in advance of a more serious cardiac event.

A patient undergoing chemotherapy is at risk for cardiotoxicity; the heart muscle is damaged by the cancer drug. A subcutaneously implanted sensor could monitor the patient's heart over the course of treatment. Just as an X-ray dosimeter signals that a maximum allowable exposure has been reached, the sensor would indicate when the patient is in danger of severe cardiac toxicity.

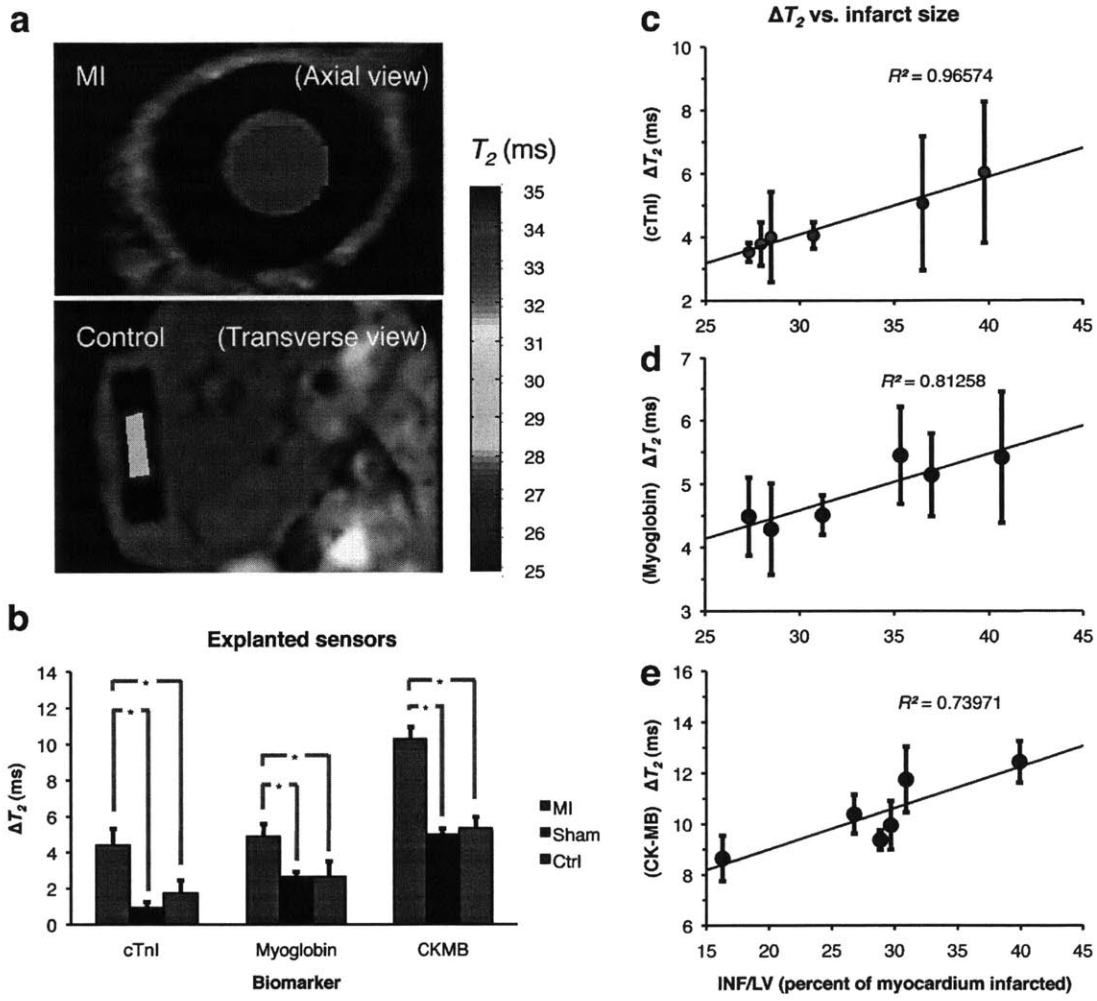


Figure 6-5: Sensors implanted in a myocardial infarction (MI) model. MRI measurements of the sensor (a) show one possible use. Sham and control experiments show that the sensors indeed detect the MI (b). The measured $T_2$ increase with the amount of damaged tissue (c-e) as would be expected from Figure 6-4. Reproduced from Ling, Pong, Vassiliou et al. [89].

## 6.2 Nanoparticle aggregation

Magnetic particles have long been known to increase the relaxation rate in fluids, and established models exist for the mechanism behind this contrast [39, 91, 92, 93, 94]. The theory developed to calculate relaxation due to single spherical particles was applied to clusters of particles [95, 96, 97]. The particles are assumed to bind under diffusion-limited aggregation to form fractal structures. The single-particle theory is applied by modeling a new sphere with reduced magnetization per unit volume. The simultaneous assumption of a fractal aggregate and a solid sphere appears to be contradictory. The model, however, predicts the correct qualitative change in $T_2$ as the particles aggregate. The scaling of $T_2$ with aggregation was simulated in collaboration with Keith Brown and published in the *Journal of Magnetism and Magnetic Materials* [98]. Numerical simulations of the random-walk diffusion of water molecules around magnetic particles confirmed the results of the simplified solid sphere model.

A second simulation considered the following thought experiment: form a chain of magnetic particles and rotate the chain relative to the field while measuring $T_2$. The single-particle model would predict a constant $T_2$ regardless of the chain's orientation with respect to the field because it has no orientation-dependent parameters. The simulation, however, revealed that $T_2$ has an angular dependence. The relaxation time is at a minimum when the chain is perpendicular to the magnetic field.

The experimental verification of this model was performed in collaboration with Melanie Adams as part of the MIT Undergraduate Research Opportunities Program (UROP). Magnetic particles of diameter 1 µm (Dynabeads MyOne, Invitrogen Dynal AS, Oslo, Norway) were chosen for their very narrow size distribution, which is

revealed in the scanning electron micrograph in Figure 6-6. These particles consist of iron oxide nanoparticles in a polystyrene matrix [99].

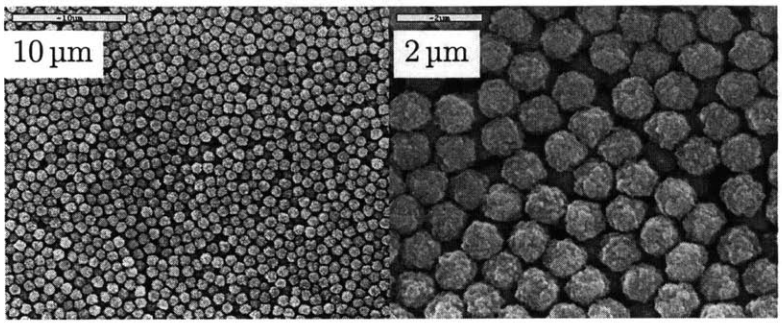


Figure 6-6: Scanning electron micrograph of 1 µm beads.

The particles were suspended in molten solution of agarose (Sigma-Aldrich) and transferred to a 5 mm NMR tube. Multiple tubes were filled with the particle suspension. The tubes were placed inside an electromagnet with a field of strength of 4 mT. A water-cooled heatsink gelled the agar solution, while the sample was inside the magnetic field, to trap the particles. Incubation times varied from 0 min to 30 min to form chains of different lengths. The aggregation is shown schematically in Figure 6-7. Micrographs of the chained and dispersed particles are shown in Figure 6-8. Analysis of multiple photographs of the chained particles yielded a power-law relationship between chain length and incubation time, as shown in Figure 6-9.

The relaxation time, $T_2$, was measured using a benchtop relaxometer (Minispec mq-20, Bruker Optics) using a standard CPMG pulse sequence. The angle between the chain axis, $\hat{B}_c$, and the NMR field, $\vec{B}_0$, is defined as $\theta_c$ and is shown in Figure 6-10. A geared sample holder rotated the tube at a rate of 3.75 turns per hour using an off-the-shelf quartz clock movement. The $T_2$ was measured continuously over several

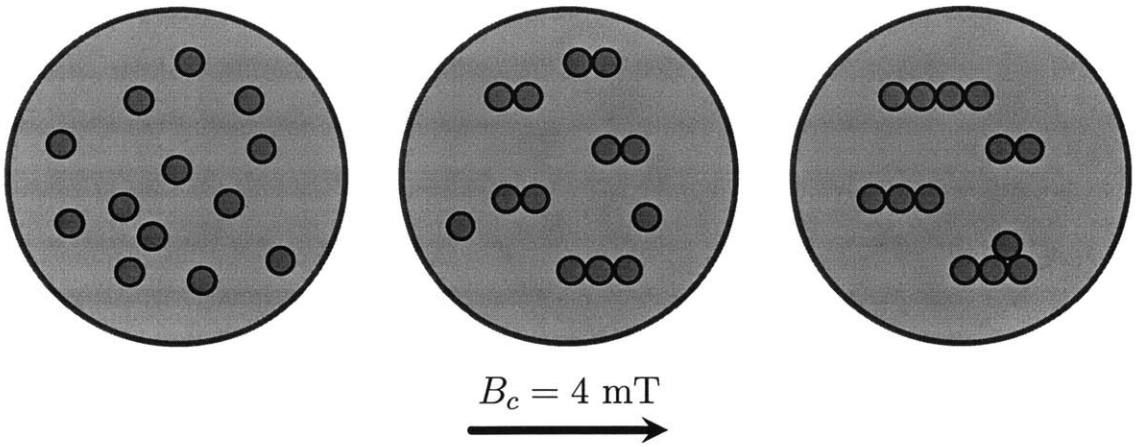


Figure 6-7: A tube containing particles suspended in molten agarose is inserted into a weak magnetic field. The particles begin to form chains. A water-cooled jacket gels the agar solution after a predetermined time, and the particle formation is captured.

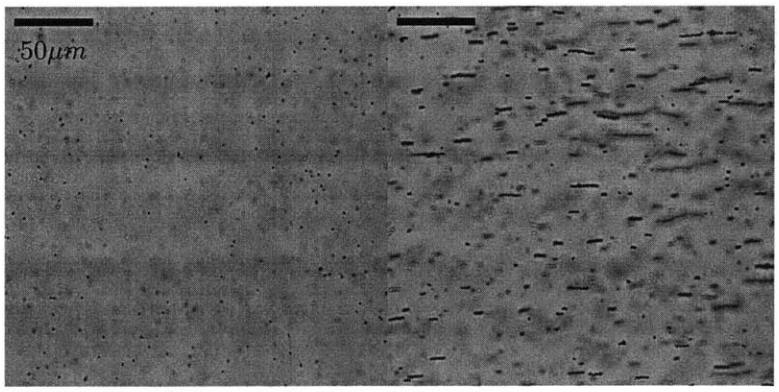


Figure 6-8: Bright field transmission micrograph of 1 µm beads suspended in agar. The chains were created by magnetizing the sample using an electromagnet ($B$=4 mT).

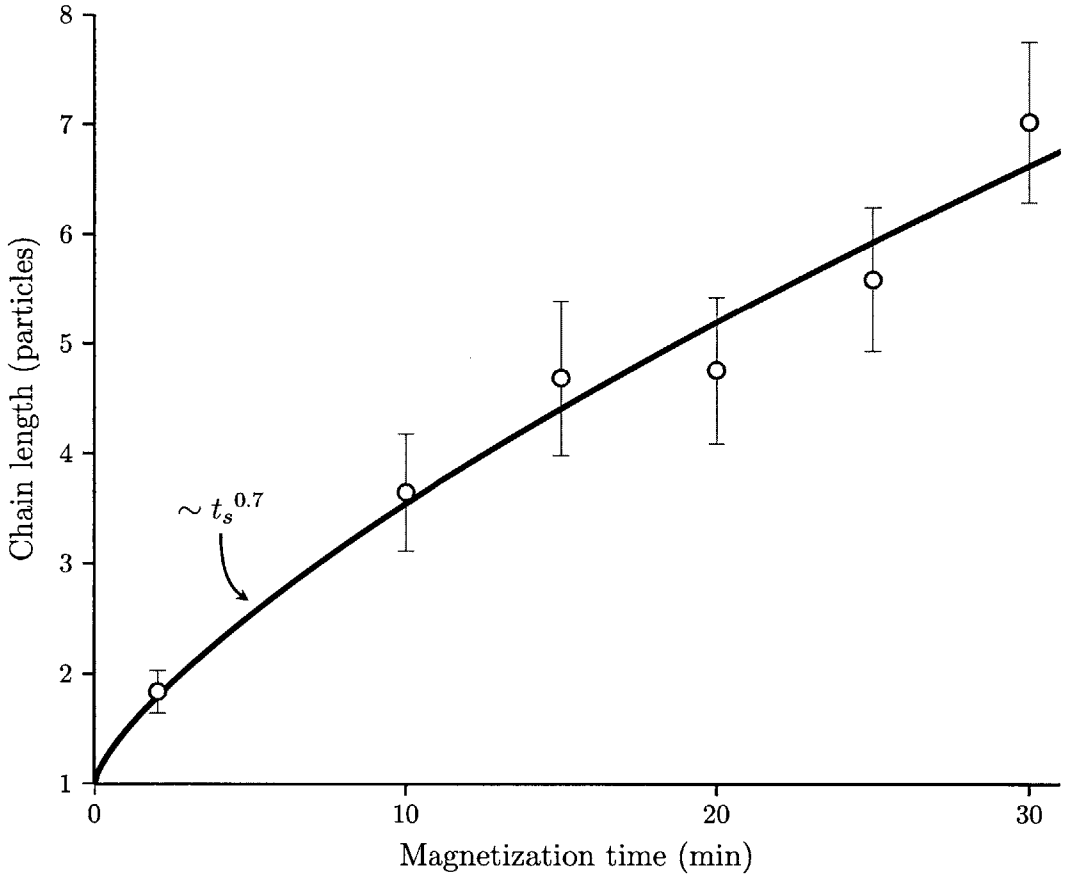


Figure 6-9: The average chain length determined by optical imaging shows a power-law increase with time inside the 4 mT magnetic field.

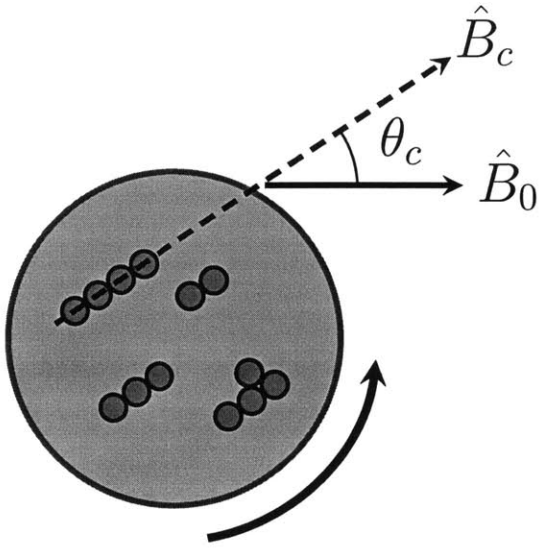


Figure 6-10: The tube is rotated along an axis perpendicular to instrument field, $B_0$, with $\theta_c$ being the angle between particle chains and $B_0$.

complete revolutions of the sample. A representative data set reveals the sinusoidal variation of relaxation time as a function of angle (Figure 6-11), as predicted by the Monte Carlo simulations. The data are fit to a cosine function to give a mean relaxation time, $T_2$, and a swing in relaxation time $\Delta T_2$.

The mean $T_2$ shows an increase as expected for large particles [94, 101, 97]. The difference between the maximum and minimum $T_2$ also increases with chain length and appears to follow a power law. The $\Delta T_2$ versus time has the same exponent as the mean chain length suggesting that it may be a better measure of chain length than the mean $T_2$.

The experiments and simulations demonstrate clearly that chains of particles cannot be modeled under the assumption that they are simply large spherical particles. This picture is neither valid nor intuitive satisfying. Finite element analysis of the field pertubation caused by a chain of three particles is shown for three different orien-

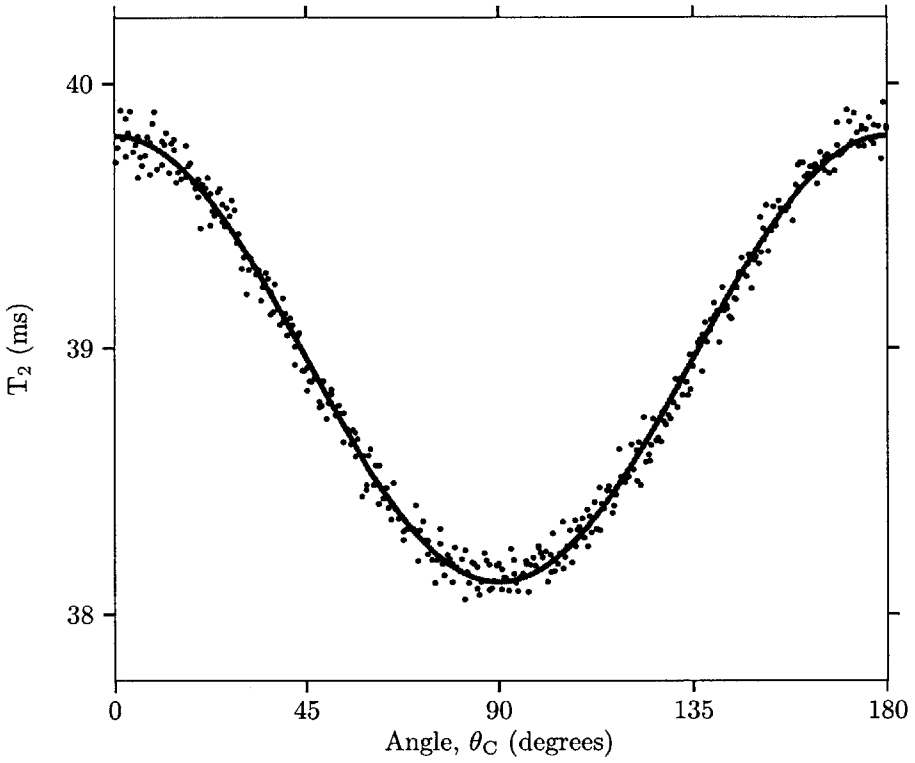


Figure 6-11: Relaxation time measurements as a function of angle between the magnetized direction, $\hat{B}_c$ and the measurement field direction, $\hat{B}_0$.

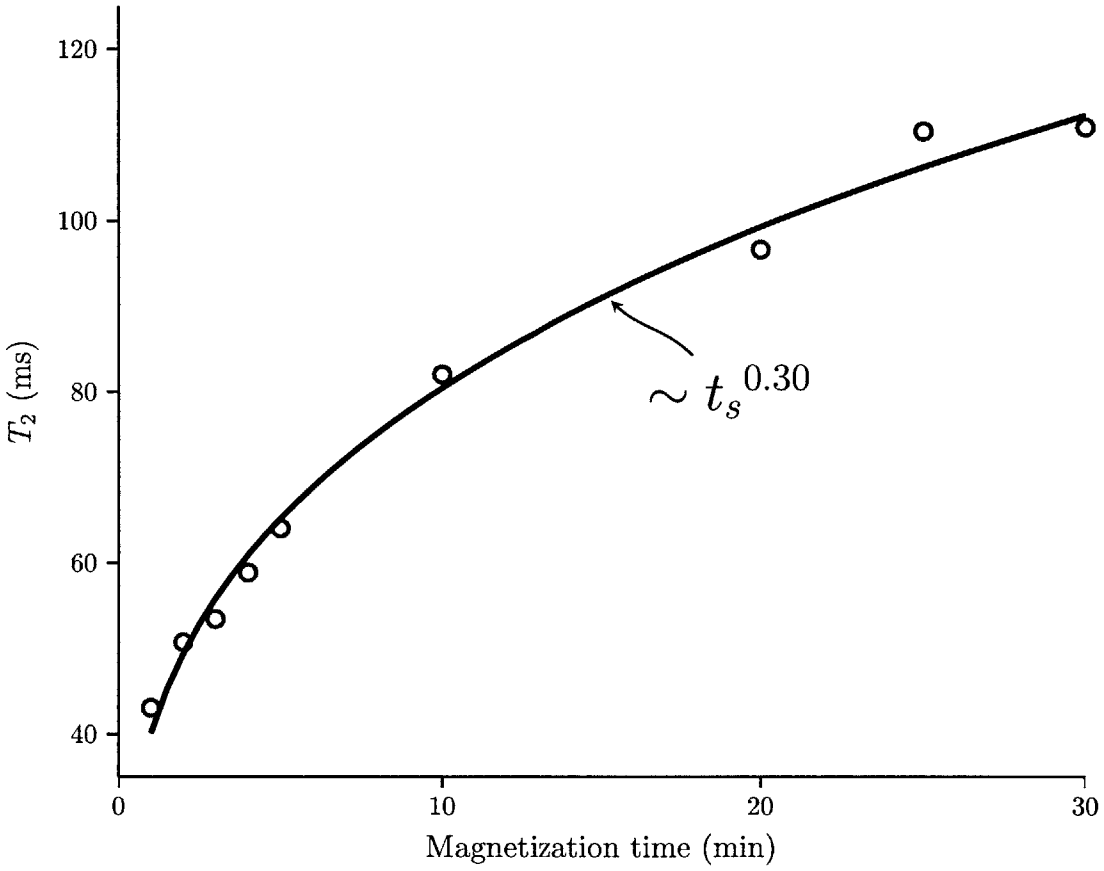


Figure 6-12: Measured relaxation time as a function of magnetization time shows a power law increase of $T_2$ with time.

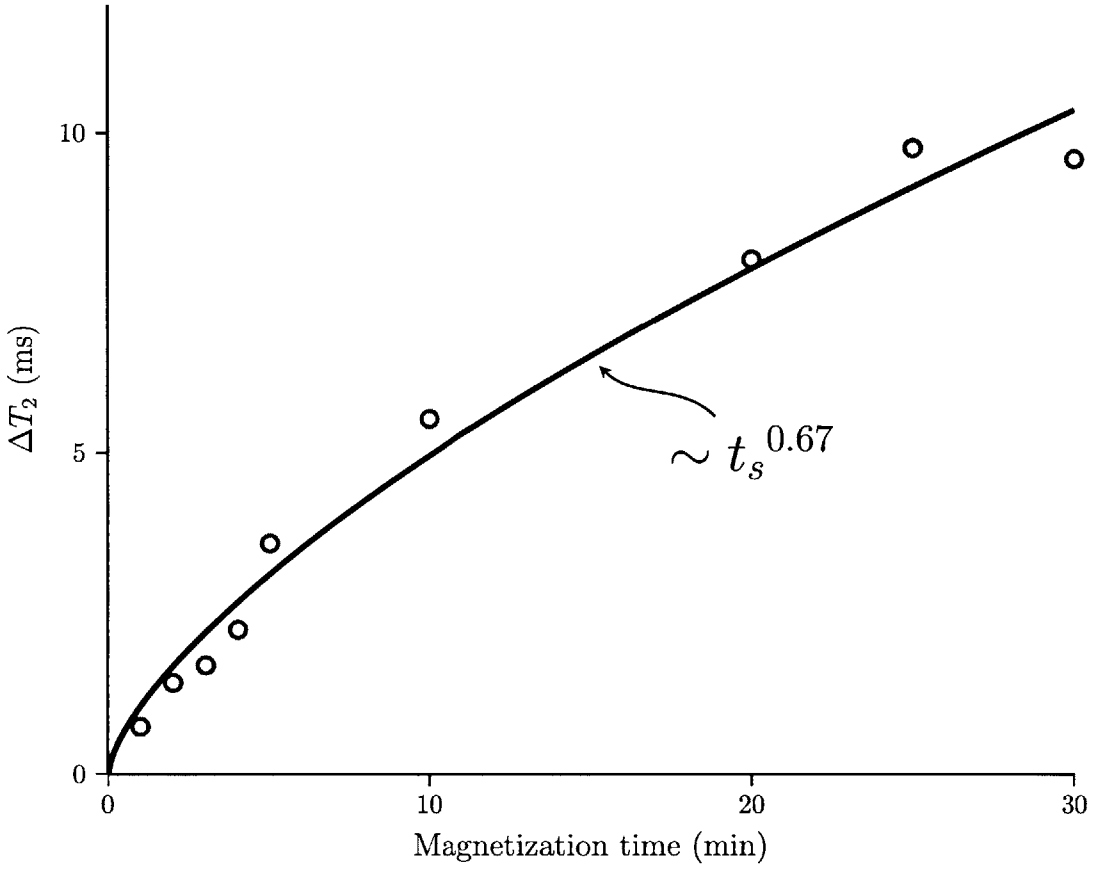


Figure 6-13: The difference between high and low $T_2$ values as the sample is rotated relative to the magnetic field also increases as a function of magnetization time and chain length.

tations in Figure 6-14. Similar analysis on single beads and two- and three-bead

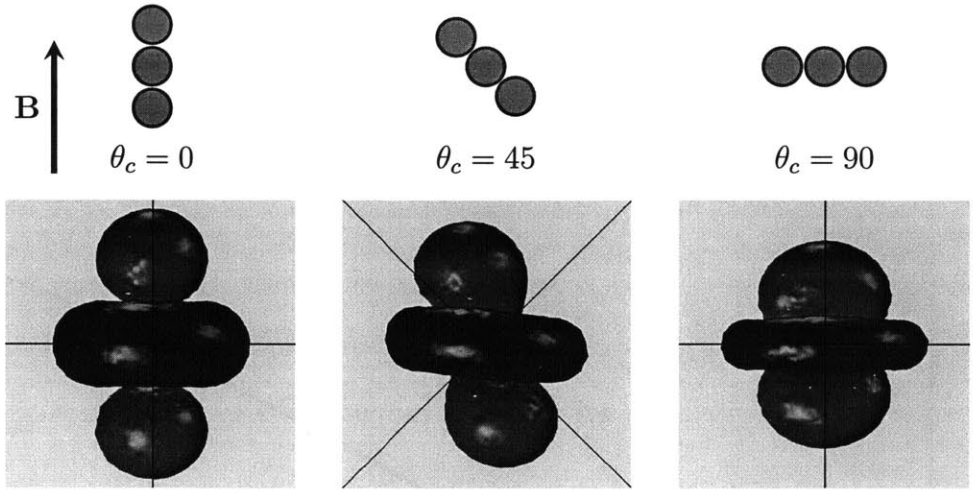


Figure 6-14: Isosurfaces of field perturbations caused by a three-particle chain at different angles to the field. The top and bottom surfaces (red) bound the 1% positive field deviation, and the center, torroidal surface (blue) bounds the negative 1% field deviation. The shape and volume of the 1% boundaries change with angle and are responsible for the angular dependence of $T_2$.

chains revealed an angular dependence on the volume of the magnetic field pertubation. Figure 6-15 shows how the perturbed volume fraction varies as a function of angle. A single particle shows no angular dependence as is expected, but is included to ensure the finite element model is sufficiently well meshed. Aligned chains ($\theta_c = 0$) generate a larger volume, indicating an overall gentler field gradient. The CPMG sequence can compensate for lower gradients more efficiently and measures a longer $T_2$. Chains rotated away from the field axis create a stronger field perturbation, and the 1% boundary encloses a smaller volume. The volume is not a predictor of relaxation time but hints at the root cause of how relaxation changes with particle orientation. It is the time-changing field that the water molecules experience that determines the relaxation time [102]. Spherical particles offer a simplification because the field per-

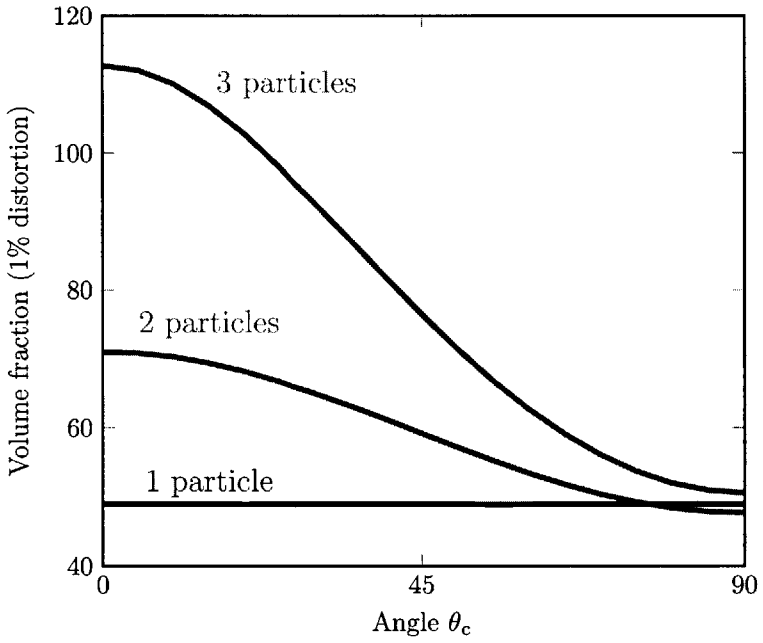


Figure 6-15: The volume of solution for which the field is perturbed at least 1% is shown versus chain angle and normalized to the particle volume. The three-particle chains show a gentler field gradient consistent with an increasing $T_2$. Rotating the chain 90° increases the field gradient, and a shorter $T_2$ is expected.

turbation and the characteristic length are both defined by the radius. The effective radius for a chain is some combination of the chain length for water diffusing along the chain and the particle radius for orbital motion. Random-walk simulations of diffusing water molecules can estimate $T_2$ directly, but it is instructive to look at the field perturbations caused by the particular particle orientation.

## 6.3 Prospects

Implanted sensors can detect soluble biomarkers. Proteins were the main focus of this chapter, but other targets can be detected by choosing the appropriate ligand for the particle surface. Magnetic particles have been developed for detecting peptides [103, 104] and short strands of nucleic acids [105].

The sensors continuously capture the target, and a single measurement reports the total exposure. This historical information can be more clinically relevant than single-point concentration measurements as shown for cardiac muscle injury.

Cardiotoxicity is a serious concern for patients undergoing chemotherapy. An implanted sensor could monitor the patient to warn when dangerous levels have been administered. The implantation would be for a relatively short period and only a very small amount of contrast agent is needed. The quantity of contrast agent inside a sensor is approximately $10^{-6}$ the amount that would need to be injected systemically. The encapsulation of this tiny amount virtually eliminates any potential for toxicity or an immune response. A cardiotoxicity sensor for monitoring cancer patients should face an easier path towards regulatory approval owing to its short residence time, low risk of toxicitiy, and dire medical need.

# Chapter 7

# Conclusion

This thesis presents a new device for direct sensing in living tissue. Emphasis was placed on monitoring cancer from within the tumor and providing the oncologist with information that is not available by other means. The sensor was designed to be deployed during a biopsy procedure and to report back on the state of the tumor environment. Because tumors are both hypoxic and acidic, and yet no easy method exists to measure those quantities, the sensor was designed to provide those data. Miniaturization and wireless detection were achieved through a new approach to nuclear magnetic resonance (NMR) that builds a small portion of the instrumentation on the implant. Sensors for oxygen, pH, and soluble proteins were developed by incorporating appropriate NMR contrast agents.

A new approach to spatial localization in NMR was explored in Chapter 3. It eliminates the need for magnetic resonance imaging (MRI) to measure the sensor. MRI produces a full picture inside the body. If a contrast agent is embedded in the tissue, it can be located and measured using MRI. The data are processed to extract the

required information, which is one number that represents a chemical concentration; the rest of the image is discarded. The sensor's on-board circuit acquires the necessary information by only measuring the contrast agent; this approach is simpler, more direct, and does not waste costly MRI time for a non-imaging purpose. The sensor and a reader probe, which sits outside the body, are two resonators coupled through their mutual inductance. The reader's weak oscillating excites the sensor, and there is a 40-fold field gain inside the sensor chamber. This enhancement ensures that only the sensor's contents are involved in the NMR experiment and the rest of the tissue is ignored. While the MRI acquires data on the entire region and then extracts the parameter of interest, the sensor directly reads that one parameter.

The instrument's specific sensing capabilities are provided by contrast agents inside the sensor chamber. Oxygen was detected in a silicone material. A pH sensitive polymer measured tumor acidity. Antibodies attached to nanoparticles created a protein sensor.

The oxygen sensor, presented in Chapter 4, is intended for the study of tissue hypoxia. Hypoxia is implicated as a driving force for metastasis, it inhibits the action of chemotherapy and radiotherapy, and it is being investigated as a possible target for treating cancer [9, 69, 70]. An implanted sensor can study all of these effects in a research setting and monitor patients undergoing treatment or enrolled in clinical trials. The sensor contains a silicone matrix embedded with a liquid siloxane. The material has a very high oxygen solubility, and it is the paramagnetism of molecular oxygen that provides the constrast. The ability to track oxygen inside a tumor allows researchers to ask new questions: "How important is tumor hypoxia on radiation and chemotherapy dose?", "Does inspiring pure oxygen help treatment?", "Do antiangiogenic factors reduce the oxygen supply to a tumor?" Answering these

questions could provide new guidance on how an oncologist should treat a patient and reveal new targets for therapies. For example, an oxygen sensor in a clinical trial could preselect patients for hypoxia. The hypoxia-activated drug, tirapazamine, may prove successful if tested in patients with confirmed hypoxia. One can envision oxygen sensors being used routinely during clinical trials to reveal whether preselecting for hypoxia is necessary. Clinical drug trials are risky and expensive; the small incremental cost of adding a tumor oxygen sensor would more than pay off if it identifies a subpopulation that benefits from the drug.

Tumors are acidic, and prior work has suggested that when a potent chemotherapeutic is administered they become more acidic [11, 44]. The benchtop testing of a pH sensor in Chapter 5 showed it to be fast, accurate, and stable. The melanoma study did not achieve the therapeutic effect, and histology showed no difference between treated and untreated tumors. There was no drug effect for the sensors to measure, but there was evidence of a gradual decrease in pH over the course of the experiment. This was consistent with the increasing necrosis shown by tissue histology. Future experiments should establish a new dosing regimen that produces a response to chemotherapy and should histologically verify that response. The experiment can be repeated with an implanted sensor to explore pH change as an indicator of treatment. The most important consideration when monitoring tumor pH is the wildly heterogeneous makeup of the tumor: the pH will vary from point to point throughout the tumor. Because an implanted sensor measures the same location repeatedly, it tracks the temporal change in pH rather than the spatial variation. It should therefore prove an excellent indicator of treatment efficacy in response to a chemotherapeutic.

Soluble proteins released from damaged heart muscle cells enter circulation and can

be detected anywhere in the body. This may suggest that a blood test is sufficient to detect cardiac damage and that an implanted sensor is not necessary at all. Chapter 6, however, showed that a protein sensor is useful becuase it measures the sensor's total exposure to the protein rather than an instantaneous concentration. Exposure represents the entire history of a protein's concentration in the body and is a more clinically relevant metric in some instances. Sensors measuring a cardiac panel in a myocardial infarction model demonstrated that protein exposure correlated with the amount of damaged heart tissue. Where a blood test simply identifies that damage has occurred, the sensor can quantify the amount of tissue damage.

The protein sensor's ability to measure total cardiac damage has a direct application in monitoring cardiac toxicity induced by chemotherapy. An oncologist could quantitatively monitor the extent of cardiac toxicity and take action before a critical level is reached.

The implanted sensor presented in this thesis was designed to fit through a biopsy needle because almost all cancer patients will undergo a tumor biopsy. The sensor can be implanted without any additional discomfort to the patient and is effectively non-invasive. It has the potential to predict therapeutic outcome and guide treatment options. Most importantly, through its direct access to the tumor, the sensor will give the oncologist rapid feedback and save valuable time in the early stages of treatment. The patient will be started on the right drug sooner and spared the unnecessary side effects of ineffective treatment.

# Future work

The implantable sensor is a powerful preclinical research tool. It offers direct, repeat, and non-invasive measurements on tissue. Researchers can incorporate the sensor into their own preclinical models and track the same animal over time. The sensor's report of tissue oxygen or pH offers a general, non-specific indicator of tissue health. Oftentimes a marker that is specific to a tissue or a condition must be tracked, and the sensor can exploit any of a variety of NMR contrast mechanisms to measure those markers.

A natural extension of this work is to create a system that does not require advanced knowledge on the part of the end user. The work in Chapter 3 offers the critical elements: a set of identical sensors, a reader coil that is insensitive to the position of the sensor, and a method to pre-tune the system. The missing component is a uniform field magnet that would allow a mouse to be inserted into the reader and the measurement to proceed automatically. The mice could be trained to enter the magnet willingly, eliminating the need for anesthesia and allowing more frequent measurements.

The pH and oxygen sensors were demonstrated separately but could be combined into a single sensor. Figure 7-1 shows the concept of a double sensor. The siloxane would first be cured as a ring leaving space in which the pH-sensitive gel can be polymerized. The two materials have significantly different relaxation time constants, and so they can both be measured simultaneously. The result is a combined sensor for measuring tumor hypoxia and pH.

NMR spectroscopy distinguishes specific chemical groups and identifies many molecules by their NMR spectrum. Adding spectroscopic ability to the sensor's enhanced

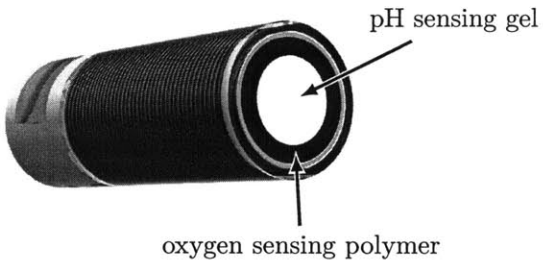


Figure 7-1: Concept implantable sensor for simultaneous pH and oxygen measurements.

signal-to-noise ratio could open up a wide array of chemicals that can be detected in vivo. A uniform magnetic field is absolutely necessary, and shim coils must be added to eliminate small field imperfections. The sensor would not need to change physically, but the materials would need to be chosen to avoid any permeability mismatch that would distort the magnetic field. The sensor chamber is a very clean environment in which to perform spectroscopy, especially compared to tissue. The sensor chamber could be filled with a polymer matrix that excludes cells and large molecules. The sensor could then search for small molecules based on their NMR spectrum or based on their interaction with specific side groups on the polymer matrix. The system will never achieve the level of sensitivity of a high-field NMR spectrometer, but the basic spectroscopic techniques would open up a vast array of possibilities for in vivo sensing, such as small molecules, markers of metabolism, and neurotransmitters.

A hand-held or even wearable system is possible considering the low power require-

ments of the measurement. Because the reader creates a weak field, only a lower power pulse amplifier is needed. The sensor measurements required 5 µs duration pulses that were only 5 W. That is less than 1 W averaged over the entire measurement. This power requirement is well within the capabilities of a portable battery-operated device. If the sensor is implanted very close to the skin's surface, the magnets can also be miniaturized and it would be possible to build a wearable reader that the patient could use at home. Patients can be released sooner from the hospital because the system will monitor the patient at home. It can detect early warning signs and inform the patient to visit the doctor before it is too late.

# Commercialization

Commercializing the sensor will involve carefully selecting an unmet clinical need with a short path to regulatory approval. The ideal application is one that would benefit from an implanted sensor, will require only a very short implantation period, and will have a clearly defined end point. One example is a subcutaneous cardiac toxicity sensor for chemotherapy patients. Cardiac toxicity is of great concern when choosing chemotherapeutic dose and is often a cause to reduce the dose or to suspend treatment altogether. The sensor would be implanted only for the duration of therapy and could easily be removed if any complications were to arise. The goal would be for the sensor to predict cardiotoxicity earlier on so that the dose can be adjusted sooner. The first trial would involve acquiring the sensor data while the patients receive the standard of care. The sensors would be explanted at the end of the study. The sensor's predictive value can be assessed by how well the sensor readings correlated to outcomes or actions later on. For example, an elevated reading on day

two may correlate with the reduction of dose on day ten. A follow-up trial would then compare the standard of care to a sensor-assisted treatment plan in which the sensor's predictions are used to adjust the dose.

A second short-term application would be a sensor to monitor tumors that will be treated with radiotherapy before being surgically resected. Some tumors cannot be removed surgically because of their size and location. Patients must first receive radiation therapy for several weeks to reduce the tumor size before surgery [106]. An oxygen sensor, implanted before the radiation therapy, will measure the tumor oxygenation over the course of treatment. The sensor will be removed when the tumor is resected. No change to the standard of care would be made except for the sensor implantion, which would involve little to no additional risk to the patient. The data collected from the sensor will be compared to the patient's progress to determine whether the sensor could predict the therapeutic outcome. The ability to predict early on whether the radiation therapy is working or whether a higher dose is needed would be particularly beneficial to the patient.

# Appendix A

# Least-squares echo estimation

This chapter presents an improvement to the standard acquisition method in single-sided NMR systems to increase the signal-to-noise ratio. It uses a least squares estimate of the entire echo rather than just the peak.

Single-sided NMR systems are compact and portable and allow for measurement on samples that will not fit inside the bore of a superconducting magnet in an NMR spectrometer or an MRI [107]. These systems use an array of permanent magnets to create a uniform field in a remote region [108] or a fixed gradient that allows slice-selective measurements and profiling [109, 44]. Non-destructive testing is essential for historical artifacts [110, 111] but is also useful for quality control on a production line [112]. These advantages come at the cost of lowered signal-to-noise ratio. The sensitive region is far from the magnet, and the magnetic fields tend to be very weak. The oscillating field is also weak, and proper shielding becomes difficult.

Relaxation time measurements almost exclusively rely on spin-echo sequences. The echoes are typically short lived owing to the spread in Larmor frequency across

the sample, and the width of the echo is ultimately determined by the bandwidth of the excitation pulse. Setting up for measurement requires identifying the echo and adjusting the receiver phase such that the 'real' and 'imaginary' channels of the quadrature-detected signal correspond to the even and odd decomposition of the echo envelope. The peak resides on the real channel, while the imaginary channel is zero. The acquisition window is centered and narrowed to capture the peak amplitude from real channel. Relaxation times are measured by tracking the decay of the echo amplitude across many echoes.

Acquiring only the peak avoids collecting noise when no signal is expected. An optimum acquisition time window exists that maximizes the signal-to-noise ratio. The window is widened until the accumulated signal drops below a noise threshold [113]. The optimum window is determined by the echo shape and the noise level. It must be found empirically.

## A.1 Theory

The proposed method uses a standard CPMG pulse sequence with an expanded acquisition window to capture and record every echo envelope. The detection scheme requires a known ideal echo, $F(t)$, such that the acquired data for each echo would be given by

$$D(t) = \alpha F(t) + e(t) \tag{A.1}$$

where $\alpha$ is the echo amplitude and $e$ is the noise in the measurement. The NMR receiver will record $N_s$ complex samples from each of $N_e$ echoes and store the data in a matrix, $\mathbf{D}$, of size $N_s \times N_e$. The echo function should also be in sampled form,

$\mathbf{F}$, of size $N_s \times 1$.

It is assumed that the echo duration is much shorter than the relaxation time so that relaxation during the echo is negligible. If $\mathbf{D}$ were real then it can be represented as:

$$\mathbf{D} = \mathbf{F} \cdot \mathbf{A} + \mathbf{E} \tag{A.2}$$

where $\mathbf{A}$ is a vector of echo amplitudes and $\mathbf{E}$ is the noise. Calculating the echo amplitudes is achieved by finding the value of $\mathbf{A}$ that minimizes the error, $|\mathbf{D} - = \mathbf{F} \cdot \mathbf{A}|^2$. This formulation is precisely the least squares problem with a single parameter [114]. The solution is

$$\mathbf{A} = \frac{\mathbf{F}^{\mathrm{T}}\mathbf{D}}{\mathbf{F}^{\mathrm{T}}\mathbf{F}} \tag{A.3}$$

The equation is simplified by normalizing the echo function, such that $\sqrt{\mathbf{F}^{\mathrm{T}}\mathbf{F}} = 1$. The acquired echo data are not real but, rather, are complex numbers with two orthogonal components. The echo amplitude, $\alpha$, scales both the real and imaginary signals, and, therefore, Equation (A.2) can be written in complex form:

$$\mathbf{D}_R + i\mathbf{D}_I = (\mathbf{F}_R + i\mathbf{F}_I) \cdot \mathbf{A} + (\mathbf{E}_R + i\mathbf{E}_I) \tag{A.4}$$

where $i = \sqrt{-1}$. The real and imaginary components represent two sets of equations and can be stacked vertically.

$$\begin{bmatrix} \mathbf{D}_R \\ \mathbf{D}_I \end{bmatrix} = \begin{bmatrix} \mathbf{F}_R \\ \mathbf{F}_I \end{bmatrix} \cdot \mathbf{A} + \begin{bmatrix} \mathbf{E}_R \\ \mathbf{E}_I \end{bmatrix} \tag{A.5}$$

This has the same form as Equation (A.2), and the solution of Equation (A.3) uses all of the data from both channels.

The only outstanding issue is how the ideal echo function is found. The shape will differ depending on the system parameters, the acquisition settings, and the pulse sequence. A spin-echo sequence can yield thousands of echoes all with the same echo shape. The function, $\mathbf{F}$, can be generated by summing the echoes in the data. Implicit in this approach is the assumption that the ideal echo function represents a positive echo, $\alpha > 0$. If the pulse sequence generates a negative amplitude, such as inversion recovery, then $\mathbf{F}$ should be multiplied by minus one. Unlike magnitude detection, the least-squares method can measure negative data, and it also automatically corrects for the echo position and the receiver phase angle.

## A.2 Experiment

The least squares echo approximation was demonstrated by measuring the transverse relaxation time ($T_2$) of a dilute solution of copper sulfate on a single-sided NMR system (NMR-MOUSE/KEA, Magritek, Wellington, New Zealand). A standard CPMG pulse sequence was used to measure the transverse relaxation time (1000 echoes, TE 80 µs, 32 scans). The acquisition window was expanded to store the entire echo. Each echo consisted of 32 complex points stored as a single vector of 64 real values. The receiver phase and acquisition window were adjusted to maximize the real channel and to center the echo for comparison with the integral method. The sample was measured 1,145 times.

Figure A-1 shows the full data acquisition and highlights the peak point that is typically acquired and stored. The black line shows the outline of the echo estimate fit to the data by least-squares. The effect of changing the acquisition window is achieved by taking a subset of the data from the full data set. Echo amplitudes

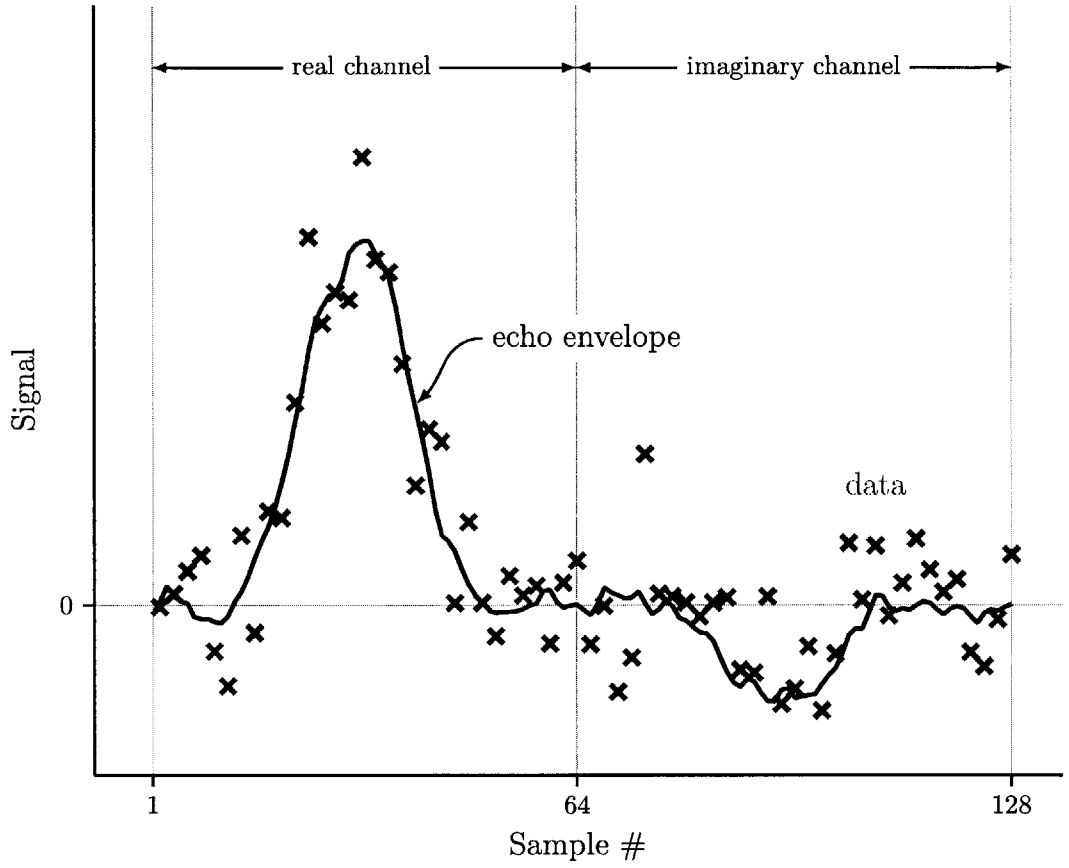


Figure A-1: Typical signal acquired from one echo. The echo envelope is formed by summing multiple echoes at the start of a multi-echo sequence.

were calculated either by the least-squares method or by integrating the data in the subset. The echo peaks were fit to a function:

$$A(t) = \alpha_0 e^{-t/T_2} \tag{A.6}$$

The error is calculated by the root mean square error between the fit and the data and is used to calculate the signal-to-noise ratio. Figure A-2 shows the effect of the acquisition window on the signal-to-noise ratio. The integral method follows the trend described in the literature [113]: a wider acquisition window increases the signal-to-noise ratio only if the signal is above a noise threshold otherwise the noise begins to dominate. The least-squares approach gives more weight to those data points where the signal is expected. The echo function has zero entries where no signal is expected, and therefore no noise from signal-free acquisition enteres the data. Acquiring more data is always preferable, and the data from the imaginary channel increase the signal-to-noise ratio by an additional 5%.

The receiver phase angle was changed in a second experiment to explore how the receiver angle affects the measured $T_2$. The same sample was measured at phase angles from $-120°$ to $120°$ in 30°steps.

The measured echo envelopes are shown in Figure A-3 as a function of the receiver angle. The dashed lines trace the peak of the real and imaginary components. All of the data were used in the least squares estimate, and the acquisition window was optimized for the integral method. The data were fit to Equation (A.6) as usual, allowing for negative amplitudes.

The least squares method relies on the assumption that the echo envelope retains its shape throughout the relaxation process and that only the amplitude changes.

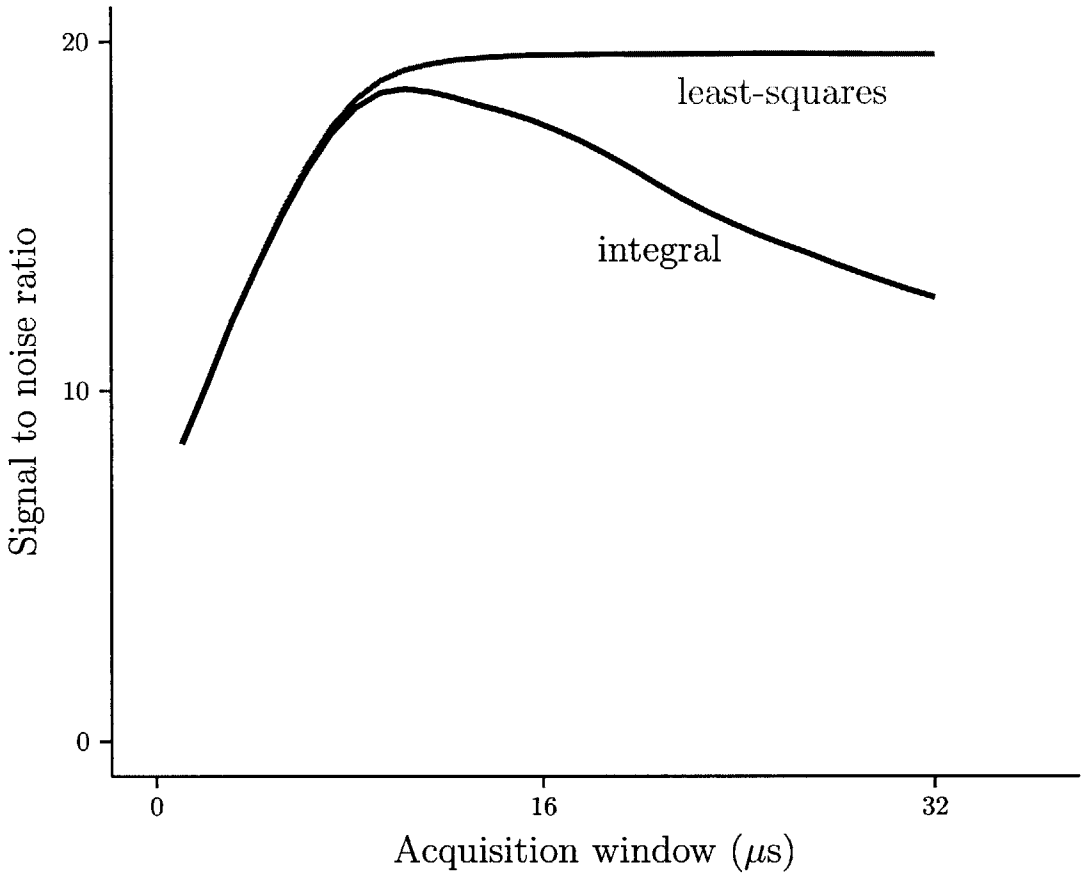


Figure A-2: The signal-to-noise ratio of the least squares estimate increases as more data is acquired. Increasing the integration time eventually adds noise but no data and leads to a reduction in SNR.

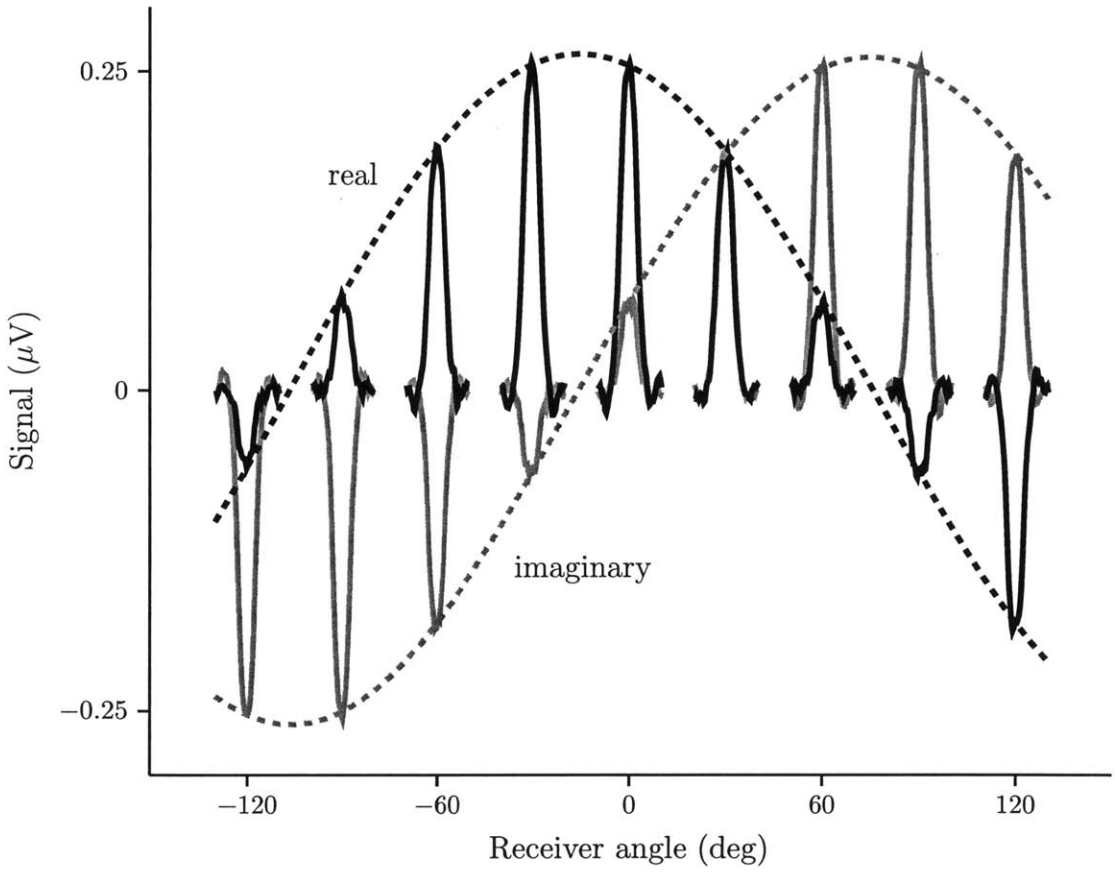


Figure A-3: Echo envelopes as detected with a different receiver angle. The dotted lines represent the peak of the real and imaginary phases.

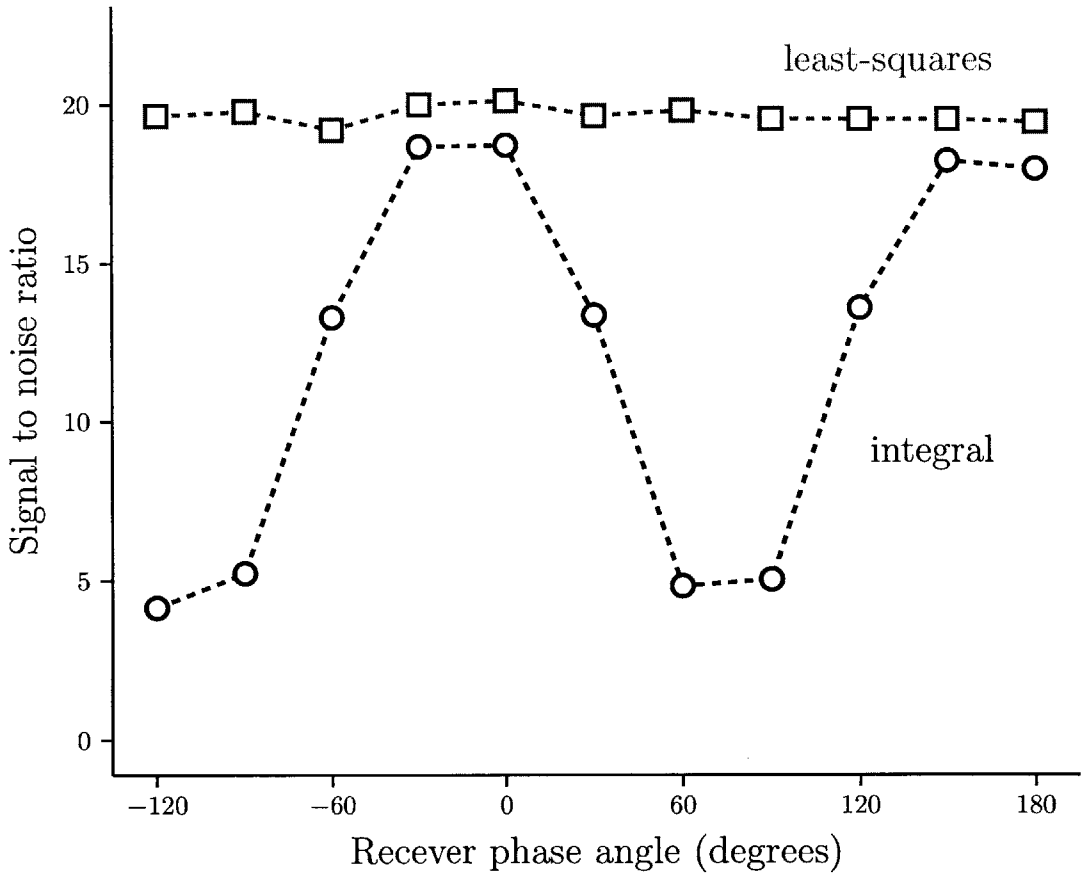


Figure A-4: Plot of the maximum achievable signal-to-noise ratio versus the receiver phase angle. The integral method requires phase alignment, but the least squares method gives an optimal SNR regardless of phase angle.

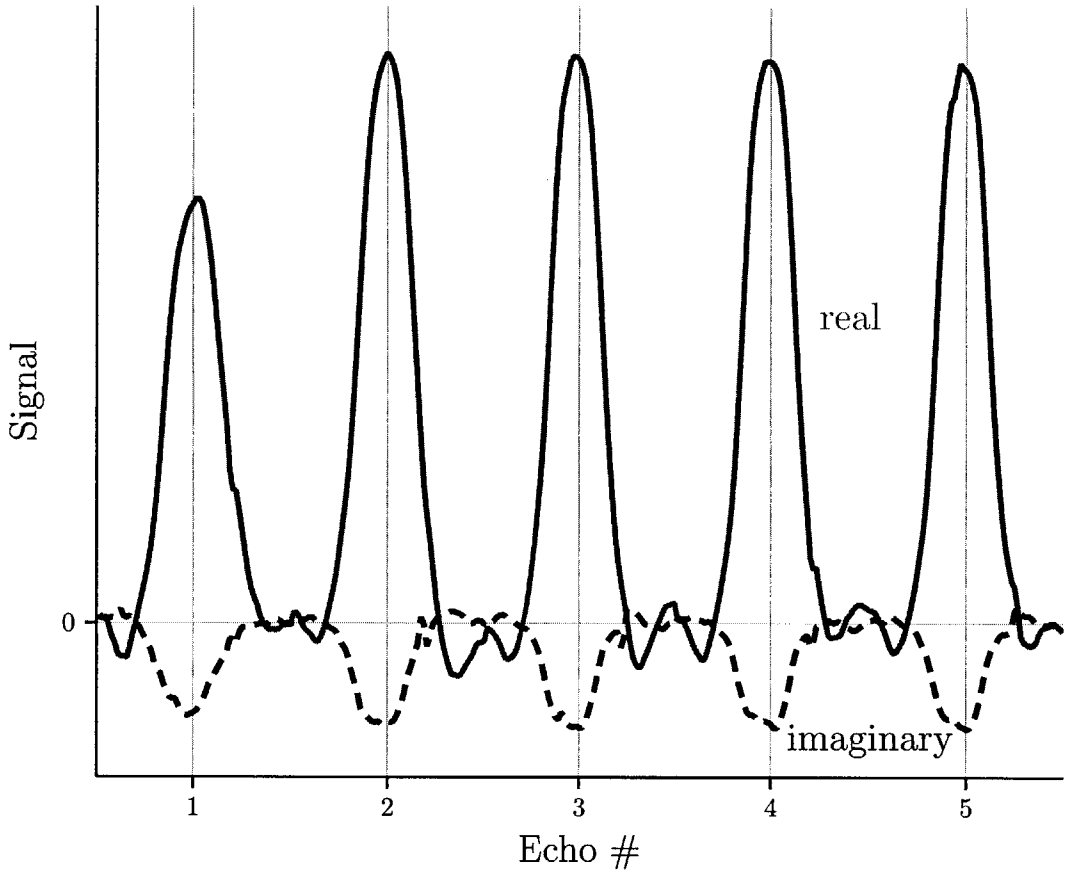


Figure A-5: The echo envelope changes over the first few echoes.

The first five echoes are shown in Figure A-5. The first echo is typically of a lower amplitude than the second and is often ignored in data analysis. The side lobes of the main echo appear to have a shape change, but the amplitude is dominated by the larger peak. Echoes 5 through 100 are normalized in area and overlaid in Figure A-6. The echoes have a similar enough shape that any deviations are well within the noise of each measurement.

The least squares estimate offers an optimal echo acquisition method with very little computational effort and with no prior knowledge of the shape of the echo. The

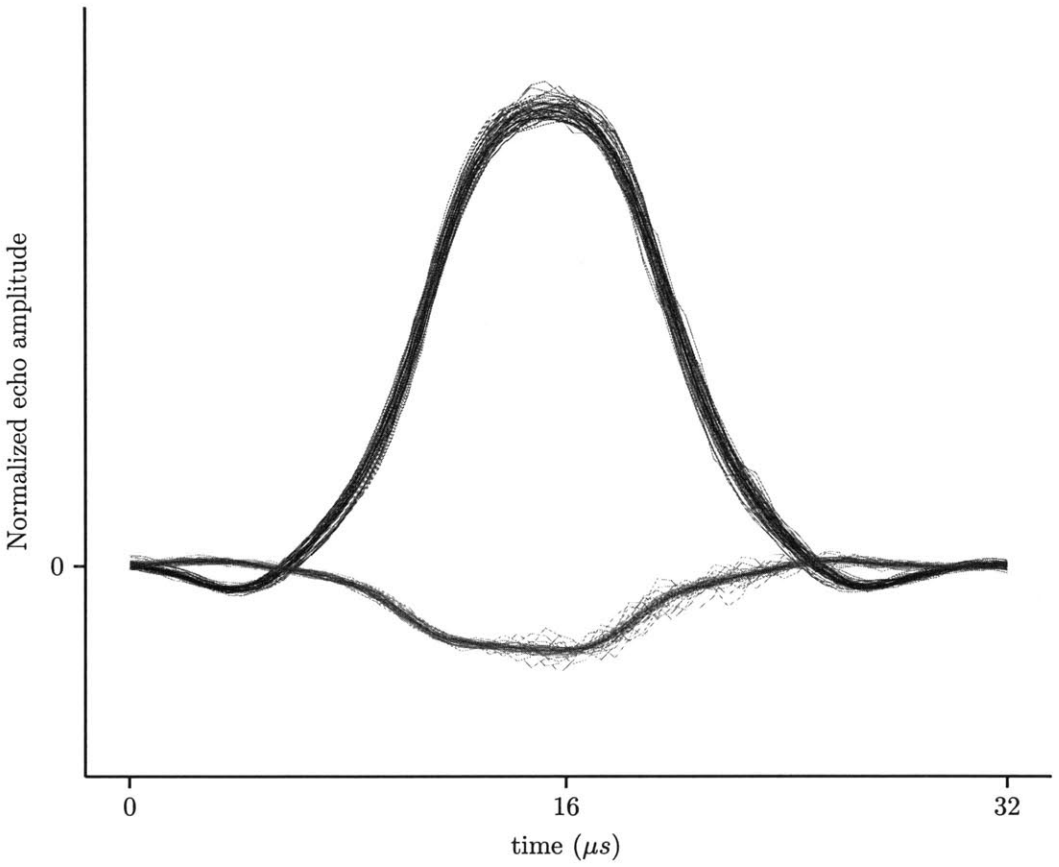


Figure A-6: Normalized signal amplitude for echoes 5 to 100. The echo shape is constant within the noise of any one measurement.

key advantage over the integration of the central portion of the peak is that a wider window *never* decreases the SNR. This is especially important for inhomogeneous field NMR because the width of the echo depends on the excitation pulse. The optimum integration width must be found for each set of parameters. Least-squared error method does not require any optimization since the echo estimate eliminates any data where no signal is expected. Any pulse sequence can be modified by increasing the acquisition window to the maximum allowed and storing all the data at the maximum sampling rate.

# Appendix B

# Numerical computation of mutual inductance

Two coils or loops of wire have a mutual inductance between them given by

$$M = \frac{\mu_0}{4\pi} \int_{C_2} \int_{C_1} \frac{d\vec{l}_1 \cdot d\vec{l}_2}{|\vec{r_1} - \vec{r_2}|}. \tag{B.1}$$

A general case analytical solution does not exist for arbitrary shapes and quickly becomes intractable for all but the simplest of cases. A numerical method that can handle any shape in any orientation is much preferred.

Equation (B.1) must be converted into a summation rather than an integral. Each coil is defined as a sequence of $n$ segments bounded by $n + 1$ points in Cartesian

space:

$$\vec{C} = \begin{bmatrix} x_1 & y_1 & z_1 \\ x_2 & y_2 & z_2 \\ x_3 & y_3 & z_3 \\ & \vdots & \\ x_{n+1} & y_{n+1} & z_{n+1} \end{bmatrix}, \tag{B.2}$$

where each row is considered a bounding point of a line segment. Equivalently, each segment can be defined by a midpoint and a vector direction. This description simplifies the subsequent calculations since the vector potential will be in the same direction as each segment. The midpoints of each segment will be used to calculate the distances between vectors and are defined as

$$\vec{R} = \frac{1}{2} \begin{bmatrix} x_1 + x_2 & y_1 + y_2 & z_1 + z_2 \\ x_2 + x_3 & y_2 + y_3 & z_2 + z_3 \\ x_3 + x_4 & y_3 + y_4 & z_3 + z_4 \\ & \vdots & \\ x_n + x_{n+1} & y_n + y_{n+1} & z_n + z_{n+1} \end{bmatrix}. \tag{B.3}$$

The segment directions are equivalent to current vectors if $I = 1\,\mathrm{A}$ and are calculated by

$$\vec{L} = \hat{I} = \begin{bmatrix} x_2 - x_1 & y_2 - y_1 & z_2 - z_1 \\ x_3 - x_2 & y_3 - y_2 & z_2 - z_2 \\ x_4 - x_3 & y_4 - y_3 & z_3 - z_3 \\ & \vdots & \\ x_{n+1} - x_n & y_{n+1} - y_n & z_{n+1} - z_n \end{bmatrix} \tag{B.4}$$

.

The line vectors would need to be scaled by $I$ in order to calculate a true vector potential, but for calculating mutual inductance unit current is preferred. Coil $C_1$ has $n$ segments and coil $C_2$ has $m$ segments. The vector potential is calculated at each point of $\vec{R}_2$ and has $m \times 3$ elements:

$$\vec{A}(\vec{r}_{2,j}) = \frac{\mu_0 I}{4\pi} \sum_{i=1}^{n} \frac{\hat{I}_{1,i}}{|\vec{r}_{1,i} - \vec{r}_{2,j}|} \tag{B.5}$$

Summing the dot product of each element of $A$ with its corresponding line segment in $L_2$ gives the mutual inductance:

$$M = \sum_{j=1}^{m} \vec{A}_1(\vec{r}_{2,j}) \cdot \vec{l}_{2,j}. \tag{B.6}$$

This formulation is extremely powerful when considering coils at arbitrary orientations to each other. The coils are defined centered at the origin with an axis along $\hat{x}$. One coil is then rotated and translated to the desired position. The rotation matrix is

$$\Omega = \begin{bmatrix} 1 & 0 & 0 \\ 0 & \cos(\psi) & \sin(\psi) \\ 0 & -\sin(\psi) & \cos(\psi) \end{bmatrix} \begin{bmatrix} \cos(\theta) & 0 & -\sin(\theta) \\ 0 & 1 & 0 \\ \sin(\theta) & 0 & \cos(\theta) \end{bmatrix} \begin{bmatrix} \cos(\phi) & \sin(\phi) & 0 \\ -\sin(\phi) & \cos(\phi) & 0 \\ 0 & 0 & 1 \end{bmatrix}. \tag{B.7}$$

The rotated direction vectors are $\vec{L}_{rot} = \vec{L}\Omega$. The midpoints must also be translated to the coil's new center coordinates $(X, Y, Z)$ since they are referenced to the origin. The new midpoints are $\vec{R}_{rot,trans} = \vec{R}\Omega + (X, Y, Z)$. The computation is extremely fast even on a modest PC with calculation of M taking a few milliseconds for thousand-segment coils.

THIS PAGE INTENTIONALLY LEFT BLANK

# Bibliography


[1] A. J. Moss, W. J. Hall, D. S. Cannom, J. P. Daubert, S. L. Higgins, H. Klein, J. H. Levine, S. Saksena, A. L. Waldo, D. Wilber, M. W. Brown, and M. Heo, "Improved survival with an implanted defibrillator in patients with coronary disease at high risk for ventricular arrhythmia," *New England Journal of Medicine*, vol. 335, pp. 1933–1940, 26 Dec. 1996.

[2] Quallion, LLC, "Ql0003i rechargeable lithium ion battery specification sheet," Accessed online 27 August 2012.

[3] S. Standring and H. Gray, *Gray's anatomy : the anatomical basis of clinical practice*. Edinburgh: Churchill Livingstone/Elsevier, 40, anniversary ed., 2008.

[4] R. Eliakim, K. Yassin, I. Shlomi, A. Suissa, and G. M. Eisen, "A novel diagnostic tool for detecting oesophageal pathology: the pillcam oesophageal video capsule," *Alimentary Pharmacology and Therapeutics*, vol. 20, no. 10, pp. 1083–1089, 2004.

[5] J. Ferlay, H. R. Shin, F. Bray, D. Forman, C. Mathers, and D. M. Parkin, "GLOBOCAN 2008 v2.0, cancer incidence and mortality worldwide: IARC cancerbase no. 10," 2010.

[6] American Cancer Society, *Cancer Facts and Figures 2013*. Atlanta, GA: American Cancer Society, 2013.

[7] American Cancer Society, *Cancer Prevention and Early Detection Facts and Figures 2013*. Atlanta, GA: American Cancer Society, 2013.

[8] American Cancer Society, *Cancer Treatment and Survivorship Facts and Figures 2012-2013*. Atlanta, GA: American Cancer Society, 2012.

[9] W. K. Hong, W. N. Hait, D. W. Kufe, R. E. Pollock, R. C. Bast, R. R. Weichselbaum, J. F. Holland, and E. F. III, *Holland Frei Cancer Medicine Eight*. Shelton, CT: People's Medical Publishing House, 2010.

[10] R. E. LaFond, *Cancer: the outlaw cell*. Oxford ; New York: American Chemical Society/Oxford University Press, 3 ed., 2012.

[11] D. Hanahan and R. A. Weinberg, *Hallmarks of Cancer: The Next Generation*, vol. 144. Cell Press, 03/04 2011.

[12] R. A. Weinberg, *One renegade cell: how cancer begins*. New York: Basic Books, 1 ed., 1998.

[13] D. Slamon, G. Clark, S. Wong, W. Levin, A. Ullrich, and W. McGuire, "Human breast cancer: correlation of relapse and survival with amplification of the her-2/neu oncogene," *Science*, vol. 235, pp. 177–182, January 09 1987.

[14] S. Verma, D. Miles, L. Gianni, I. E. Krop, M. Welslau, J. Baselga, M. Pegram, D.-Y. Oh, V. Diéras, E. Guardino, L. Fang, M. W. Lu, S. Olsen, and K. Blackwell, "Trastuzumab emtansine for HER2-Positive advanced breast cancer," *New England Journal of Medicine*, vol. 367, pp. 1783–1791, 08 Nov. 2012.

[15] L. Amiri-Kordestani, G. Blumenthal, and P. Cortazar, "Clinical review KADCYLA (ado-trastuzumab emtansine, t-dm1)," Tech. Rep. BLA 125,427, FDA Center for Drug Evaluation and Research, 2013.

[16] "Kadcyla (ado-trastuzumab emtansine) prescribing information," tech. rep., Genentec, Inc., 2013.

[17] "Stivarga (regorafenib) prescribing information," tech. rep., Bayer HealthCare Pharmaceuticals, Inc., 2012.

[18] P. Keegan, "Summary review for regulatory action, stivarga (regorafenib)," Tech. Rep. NDA 203085, FDA Center for Drug Evaluation and Research, 2013.

[19] M. J. Bissell and D. Radisky, "Putting tumours in context," *Nature Reviews Cancer*, vol. 1, pp. 46–54, Oct. 2001.

[20] R. S. M.D., *Hyaluronan in cancer biology*. San Diego, CA: Academic Press/Elsevier, 1 ed., 2009.

[21] M. Hu and K. Polyak, "Microenvironmental regulation of cancer development," *Current opinion in genetics and development*, vol. 18, pp. 27–34, 2 2008.

[22] S. Huang and D. E. Ingber, "The structural and mechanical complexity of cell-growth control," *Nature cell biology*, vol. 1, pp. E131–E138, Sep. 1999.

[23] C. S. Chen, M. Mrksich, S. Huang, G. M. Whitesides, and D. E. Ingber, "Geometric control of cell life and death," *Science*, vol. 276, pp. 1425–1428, 30 May 1997.

[24] D. E. Ingber, "Can cancer be reversed by engineering the tumor microenvironment?," *Seminars in cancer biology*, vol. 18, pp. 356–364, Oct. 2008.

[25] F. Bloch, "Nuclear induction," *Physical Review*, vol. 70, p. 460, 01 Oct. 1946.

[26] B. P. Cowan, *Nuclear magnetic resonance and relaxation.* Cambridge ; New York: Cambridge University Press, 1997.

[27] E. Fukushima and S. B. W. Roeder, *Experimental Pulse NMR: A nuts and bolts approach.* Reading, Mass.: Addison-Wesley Pub. Co., Advanced Book Program, 1981.

[28] C. P. Slichter, *Principles of magnetic resonance, with examples from solid state physics.* New York: Harper and Row, 1963.

[29] A. Abragam, *The principles of nuclear magnetism.* Oxford: Clarendon Press, 1961.

[30] D. I. Hoult and R. E. Richards, "Signal-to-noise ratio of nuclear magnetic-resonance experiment," *Journal of Magnetic Resonance*, vol. 24, no. 1, pp. 71–85, 1976.

[31] D. I. Hoult, "The principle of reciprocity in signal strength calculations - a mathematical guide," *Concepts in Magnetic Resonance*, vol. 12, no. 4, pp. 173–187, 2000.

[32] D. I. Hoult, "NMR receiver - description and analysis of design," *Progress in Nuclear Magnetic Resonance Spectroscopy*, vol. 12, pp. 41–77, 1978.

[33] *Concepts in magnetic resonance.Part B, Magnetic resonance engineering [electronic resource]*, 2003-.

[34] *Concepts in magnetic resonance.Part A, Bridging education and research [electronic resource]*, 2003-.

[35] *Journal of magnetic resonance*, 1997-.

[36] *Magnetic Resonance in Medicine*, 1984-.

[37] Tim the Beaver. (personal communication).

[38] M. Zahn, *Electromagnetic field theory : a problem solving approach.* Malabar, Fla.: Krieger Pub. Co., reprint w/corrections ed., 2003; 1979.

[39] A. G. Redfield, "On the theory of relaxation processes," *IBM Journal*, vol. 1, p. 19, Jan. 1957.

[40] C. P. Poole and H. A. Farach, *Relaxation in magnetic resonance; dielectric and Mössbauer applications.* New York: Academic Press, 1971.

[41] E. L. Hahn, "Spin echoes," *Physical Review*, vol. 80, p. 580, 15 Nov. 1950.

[42] H. Y. Carr and E. M. Purcell, "Effects of diffusion on free precession in nuclear magnetic resonance experiments," *Physical Review*, vol. 94, p. 630, 01 May 1954.

[43] S. Meiboom and D. Gill, "Modified spin-echo method for measuring nuclear relaxation times," *Review of Scientific Instruments*, vol. 29, pp. 688–691, Aug. 1958.

[44] G. Eidmann, R. Savelsberg, P. Blumler, and B. Blumich, "The NMR MOUSE, a mobile universal surface explorer," *Journal of Magnetic Resonance Series A*, vol. 122, pp. 104–109, Sep. 1996.

[45] P. J. Prado, B. Blümich, and U. Schmitz, "One-dimensional imaging with a palm-size probe," *Journal of Magnetic Resonance*, vol. 144, pp. 200–206, 6 2000.

[46] A. Sezginer, R. L. Kleinberg, M. Fukuhara, and L. L. Latour, "Very rapid simultaneous measurement of nuclear-magnetic-resonance spin-lattice relaxation-time and spin spin relaxation-time," *Journal of Magnetic Resonance*, vol. 92, pp. 504–527, May 1991.

[47] D. I. Hoult, "The origins and present status of the radio wave controversy in NMR," *Concepts in Magnetic Resonance Part A*, vol. 34A, no. 4, pp. 193–216, 2009.

[48] D. I. Hoult and N. S. Ginsberg, "The quantum origins of the free induction decay signal and spin noise," *Journal of Magnetic Resonance*, vol. 148, pp. 182–199, Jan. 2001.

[49] J. A. Kong, *Electromagnetic wave theory.* Cambridge, Mass.: EMW Publishing, 2000.

[50] M. Faraday, *Experimental researches in electricity.* New York: Dover Publications, 1965.

[51] H. P. Greenspan and D. J. Benney, *Calculus : an introduction to applied mathematics.* Brookline, MA: Breukelen Press, 1997.

[52] F. W. Grover, "The calculation of the mutual inductance of circular filaments in any desired positions," *Proceedings of the IRE*, vol. 32, no. 10, pp. 620–629, 1944.

[53] H. Nyquist, "Thermal agitation of electric charge in conductors," *Physical Review*, vol. 32, p. 110, 01 July 1928.

[54] A. van der Ziel, *Noise; sources, characterization, measurement.* Englewood Cliffs, N.J.: Prentice-Hall, 1970.

[55] J. B. Johnson, "Thermal agitation of electricity in conductors," *Physical Review*, vol. 32, pp. 97–109, July 1928.

[56] M. D. Schnall, C. Barlow, V. H. Subramanian, and J. S. Leigh, "Wireless implanted magnetic resonance probes for in vivo nmr," *Journal of Magnetic Resonance (1969)*, vol. 68, pp. 161–167, 6/1 1986.

[57] J.-F. Jacquinot and D. Sakellariou, "Nmr signal detection using inductive coupling: Applications to rotating microcoils," *Concepts in Magnetic Resonance Part A*, vol. 38A, pp. 33–51, Mar. 2011.

[58] D. Sakellariou, G. L. Goff, and J. F. Jacquinot, "High-resolution, high-sensitivity NMR of nanolitre anisotropic samples by coil spinning," *Nature*, vol. 447, p. 694, 07 June 2007.

[59] A. B. Grebene, *Bipolar and MOS analog integrated circuit design.* New York: J. Wiley, 1984.

[60] N. Sun, T.-J. Yoon, H. Lee, W. Andress, R. Weissleder, and D. Ham, "Palm NMR and 1-chip NMR," *IEEE Journal of Solid-State Circuits*, vol. 46, pp. 342–352, Jan. 2011.

[61] H. Kato, M. Kuroda, K. Yoshimura, A. Yoshida, K. Hanamoto, S. Kawasaki, K. Shibuya, and S. Kanazawa, "Composition of MRI phantom equivalent to human tissues," *Medical physics*, vol. 32, pp. 3199–3208, Oct. 2005.

[62] J. M. Toth, M. Wang, B. T. Estes, J. L. Scifert, H. B. S. III, and A. S. Turner, "Polyetheretherketone as a biomaterial for spinal applications," *Biomaterials*, vol. 27, pp. 324–334, Jan. 2006.

[63] S. M. Kurtz, *PEEK biomaterials handbook*. PDL handbook series., Norwich, N.Y.; Oxford: William Andrew; Elsevier Science distributor, 2011.

[64] ASM International, *Materials and Coatings for Medical Devices– Cardiovascular*. ASM International, 2009.

[65] "LOCTITE M-31CL technical data sheet," Aug. 2005.

[66] "Certificate of compliance ISO 10993 biological tests, loctite M-31CL medical device adhesive," Tech. Rep. 05-1574, Toxicon Corporation, 13 June 2005.

[67] J. Allen, "Photoplethysmography and its application in clinical physiological measurement," *Physiological Measurement*, vol. 28, no. 3, p. R1, 2007.

[68] S. Ogawa, T. M. Lee, A. R. Kay, and D. W. Tank, "Brain magnetic-resonance-imaging with contrast dependent on blood oxygenation," *Proceedings of the National Academy of Sciences of the United States of America*, vol. 87, pp. 9868–9872, Dec. 1990.

[69] J. A. Bertout, S. A. Patel, and M. C. Simon, "The impact of $o_2$ availability on human cancer," *Nature Reviews Cancer*, vol. 8, pp. 967–975, Dec. 2008.

[70] D. Lindner and D. Raghavan, "Intra-tumoural extra-cellular pH: a useful parameter of response to chemotherapy in syngeneic tumour lines," *British journal of cancer*, vol. 100, pp. 1287–1291, Mar. 2009.

[71] S. K. Williamson, J. J. Crowley, P. N. Lara, J. McCoy, D. H. M. Lau, R. W. Tucker, G. M. Mills, and D. R. Gandara, "Phase III trial of paclitaxel plus carboplatin with or without tirapazamine in advanced non–small-cell lung cancer: Southwest oncology group trial s0003," *Journal of Clinical Oncology*, vol. 23, pp. 9097–9104, 20 Dec. 2005.

[72] D. Rischin, L. J. Peters, B. O'Sullivan, J. Giralt, R. Fisher, K. Yuen, A. Trotti, J. Bernier, J. Bourhis, J. Ringash, M. Henke, and L. Kenny, "Tirapazamine, cisplatin, and radiation versus cisplatin and radiation for advanced squamous cell carcinoma of the head and neck (TROG 02.02, HeadSTART): A phase III trial of the trans-tasman radiation oncology group," *Journal of Clinical Oncology*, vol. 28, pp. 2989–2995, 20 June 2010.

[73] H. S. Sandhu, "Effect of paramagnetic impurities on proton spin—lattice relaxation time in methane," *The Journal of chemical physics*, vol. 44, pp. 2320–2321, 15 Mar. 1966.

[74] V. H. Liu, C. C. Vassiliou, Y. Ling, and M. J. Cima, "Implantable dissolved oxygen sensor and methods of use," Filed 04 May 2010. Patent application 61/331,236.

[75] S. M. Imaad, "Injectable polymer for in vivo oxygen sensing." Dissertation, February 2013 2013.

[76] D. W. McCall, E. W. Anderson, and C. M. Huggins, "Self-diffusion in linear dimethylsiloxanes," *The Journal of chemical physics*, vol. 34, pp. 804–808, March 1961 1961.

[77] V. H. Liu, *unpublished dissertation.* phdthesis, Expected Oct. 2013.

[78] N. T. S. Evans and P. F. D. Naylor, "The dynamics of changes in dermal oxygen tension," *Respiration physiology*, vol. 2, no. 1, pp. 61–72, 1966.

[79] O. Warburg, "On the origin of cancer cells," *Science*, vol. 123, pp. 309–314, February 24 1956.

[80] J. GARRPETERS and C. HO, "Oxygen-transfer in the corneal-contact lens system," *Critical Reviews in Biomedical Engineering*, vol. 14, no. 4, pp. 289–372, 1987.

[81] D. Gochberg, R. Kennan, M. Maryanski, and J. Gore, "The role of specific side groups and ph in magnetization transfer in polymers," *Journal of Magnetic Resonance*, vol. 131, pp. 191–198, Apr. 1998.

[82] L. Josephson and S. Palmacci, "Synthesis of polysaccharide covered superparamagnetic oxide colloids." US Patent, 1993. 5,262,176.

[83] G. Y. Kim, L. Josephson, R. Langer, and M. J. Cima, "Magnetic relaxation switch detection of human chorionic gonadotrophin," *Bioconjugate chemistry*, vol. 18, pp. 2024–2028, NOV-DEC 2007.

[84] K. D. Daniel, G. Y. Kim, C. C. Vassiliou, M. Galindo, A. R. Guimaraes, R. Weissleder, A. Charest, R. Langer, and M. J. Cima, "Implantable diagnostic device for cancer monitoring," *Biosensors and Bioelectronics*, vol. 24, pp. 3252–3257, 15 July 2009.

[85] Y. Ling, C. C. Vassiliou, and M. J. Cima, "Magnetic relaxation-based platform for multiplexed assays," *Analyst*, vol. 135, no. 9, pp. 2360–2364, 2010.

[86] K. D. Daniel, G. Y. Kim, C. C. Vassiliou, F. Jalali-Yazdi, R. Langer, and M. J. Cima, "Multi-reservoir device for detecting a soluble cancer biomarker," *Lab on a Chip*, vol. 7, no. 10, pp. 1288–1293, 2007.

[87] M. J. Schwartz, D. H. Hwang, A. J. Hung, J. Han, J. W. McClain, M. M. Shemtov, A. E. Te, R. E. Sosa, E. D. Vaughan, and D. S. Scherr, "Negative influence of changing biopsy practice patterns on the predictive value of prostate-specific antigen for cancer detection on prostate biopsy," *Cancer*, vol. 112, no. 8, pp. 1718–1725, 2008.

[88] P. J. Littrup, R. A. Kane, C. J. Mettlin, G. P. Murphy, F. Lee, A. Toi, R. Badalament, and R. Babaian, "Cost-effective prostate cancer detection. reduction of low-yield biopsies," *Cancer*, vol. 74, no. 12, pp. 3146–3158, 1994.

[89] Y. Ling, T. Pong, C. C. Vassiliou, P. L. Huang, and M. J. Cima, "Implantable magnetic relaxation sensors measure cumulative exposure to cardiac biomarkers," *Nature Biotechnology*, vol. 29, pp. 273–277, 0 2011.

[90] M. J. Cima, P. Huang, Y. Ling, T. Pong, and C. C. Vassiliou, "Implantable magnetic relaxation sensors for the detection of cardiac biomarkers," Filed 25 June 2010. Patent application 61/358,449.

[91] R. J. S. Brown, "Distribution of fields from randomly placed dipoles: Free-precession signal decay as result of magnetic grains," *Physical Review*, vol. 121, p. 1379, 01 Mar. 1961.

[92] S. H. Koenig, "Solvent relaxation by uniformly magnetized solute spheres - the classical-quantal connection," *Investigative radiology*, vol. 33, pp. 822–827, Nov. 1998.

[93] S. H. Koenig and K. E. Kellar, "Theory of proton relaxation in solutions of magnetic nanoparticles, including the superparamagnetic size range," *Academic Radiology*, vol. 3, pp. S273–S276, Aug. 1996.

[94] P. Gillis and S. H. Koenig, "Transverse relaxation of solvent protons induced by magnetized spheres - application to ferritin, erythrocytes, and magnetite," *Magnetic Resonance in Medicine*, vol. 5, pp. 323–345, Oct. 1987.

[95] A. Roch, Y. Gossuin, R. N. Muller, and P. Gillis, "Superparamagnetic colloid suspensions: Water magnetic relaxation and clustering," *Journal of Magnetism and Magnetic Materials*, vol. 293, pp. 532–539, 01 May 2005.

[96] M. G. Shapiro, T. Atanasijevic, H. Faas, G. G. Westmeyer, and A. Jasanoff, "Dynamic imaging with MRI contrast agents: quantitative considerations," *Magnetic Resonance Imaging*, vol. 24, pp. 449–462, May 2006.

[97] R. A. Brooks, F. Moiny, and P. Gillis, "On $t_2$-shortening by weakly magnetized particles: The chemical exchange model," *Magnetic Resonance in Medicine*, vol. 45, pp. 1014–1020, June 2001.

[98] K. A. Brown, C. C. Vassiliou, D. Issadore, J. Berezovsky, M. J. Cima, and R. M. Westervelt, "Scaling of transverse nuclear magnetic relaxation due to magnetic nanoparticle aggregation," *Journal of Magnetism and Magnetic Materials*, vol. 322, pp. 3122–3126, Oct. 2010.

[99] R. J. S. Derks, A. Dietzel, R. Wimberger-Friedl, and M. W. J. Prins, "Magnetic bead manipulation in a sub-microliter fluid volume applicable for biosensing," *Microfluidics and Nanofluidics*, vol. 3, pp. 141–149, Apr. 2007.

[100] G. Y. Kim, C. C. Vassiliou, K. D. Daniel, and M. J. Cima, "Matrix stabilization of aggregation-based assays," Filed 13 Nov. 2008. US Patent Application 20100136517 A1.

[101] P. Gillis, F. Moiny, and R. A. Brooks, "On $t_2$-shortening by strongly magnetized spheres: A partial refocusing model," *Magnetic Resonance in Medicine*, vol. 47, pp. 257–263, Feb. 2002.

[102] P. T. Callaghan, *Translational dynamics and magnetic resonance : principles of pulsed gradient spin echo NMR.* Oxford ; New York: Oxford University Press, 2011.

[103] M. Lewin, N. Carlesso, C. H. Tung, X. W. Tang, D. Cory, D. T. Scadden, and R. Weissleder, "Tat peptide-derivatized magnetic nanoparticles allow in vivo tracking and recovery of progenitor cells," *Nature biotechnology*, vol. 18, pp. 410–414, Apr. 2000.

[104] L. Josephson, C. H. Tung, A. Moore, and R. Weissleder, "High-efficiency intracellular magnetic labeling with novel superparamagnetic-tat peptide conjugates," *Bioconjugate chemistry*, vol. 10, pp. 186–191, Mar. 1999.

[105] L. Josephson, J. M. Perez, and R. Weissleder, "Magnetic nanosensors for the detection of oligonucleotide sequences," *Angewandte Chemie-International Edition*, vol. 40, no. 17, p. 3204, 2001.

[106] J. G. Sinkovics, *Medical oncology*. New York: Dekker, 2 ed., 1986.

[107] B. Blumich, F. Casanova, J. Perlo, S. Anferova, V. Anferov, K. Kremer, N. Goga, K. Kupferschlager, and M. Adams, "Advances of unilateral mobile NMR in nondestructive materials testing," *Magnetic resonance imaging*, vol. 23, pp. 197–201, Feb. 2005.

[108] B. Manz, A. Coy, R. Dykstra, C. D. Eccles, M. W. Hunter, B. J. Parkinson, and P. T. Callaghan, "A mobile one-sided NMR sensor with a homogeneous magnetic field: The NMR-MOLE," *Journal of Magnetic Resonance*, vol. 183, pp. 25–31, Nov. 2006.

[109] S. Anferova, V. Anferov, M. Adams, P. Blumler, N. Routley, K. Hailu, K. Kupferschlager, M. J. D. Mallett, G. Schroeder, S. Sharma, and B. Blumich, "Construction of a NMR-MOUSE with short dead time," *Concepts in Magnetic Resonance*, vol. 15, pp. 15–25, Mar. 2002.

[110] N. Proietti, D. Capitani, R. Lamanna, F. Presciutti, E. Rossi, and A. L. Segre, "Fresco paintings studied by unilateral NMR," *Journal of Magnetic Resonance*, vol. 177, pp. 111–117, Nov. 2005.

[111] E. Federico, S. Centeno, C. Kehlet, P. Currier, D. Stockman, and A. Jerschow, "Unilateral NMR applied to the conservation of works of art," *Analytical and Bioanalytical Chemistry*, vol. 396, pp. 213–220, 01 Jan. 2010.

[112] H. Kühn, M. Klein, A. Wiesmath, D. E. Demco, B. Blümich, J. Kelm, and P. W. Gold, "The NMR-MOUSE: quality control of elastomers," *Magnetic resonance imaging*, vol. 19, no. 3–4, pp. 497–499, 2001.

[113] F. Casanova, J. Perlo, and B. Blümich, *Single-Sided NMR*. Berlin, Heidelberg: Springer-Verlag Berlin Heidelberg, 2011.

[114] G. Strang, *Introduction to linear algebra*. Wellesly, MA: Wellesley-Cambridge, 3 ed., 2003.